MASTERARBEIT / MASTER’S THESIS

Titel der Masterarbeit / Title of the Master‘s Thesis

The impact of X-ray-induced photoevaporative mass loss on the long-term evolution of protoplanetary disks

verfasst von / submitted by

Michael Cecil, BSc

angestrebter akademischer Grad / in partial fulfilment of the requirements for the degree of

Master of Science (MSc)

Wien, 2023

Studienkennzahl lt. Studienblatt / degree programme code as it appears on the student record sheet:	A 066 861
Studienrichtung lt. Studienblatt / degree programme as it appears on the student record sheet:	Masterstudium Astronomie
Betreut von / Supervisor:	Univ.-Prof. Dipl.-Phys. Dr. Manuel Güdel

Abstract

Context. Protoplanetary disks are the birthplaces of planetary systems, which makes them a highly interesting subject for astrophysical investigations. The difference between the short dispersal timescale of such structures and their viscous timescale, resulting from both observations and theoretical considerations, poses a significant problem in this field of research. A promising candidate for solving this issue is the evaporation of disk material by heating through irradiation from the central star. However, corresponding numerical simulations still fail to explain common observations of dispersing disks.
Aims. The aim of this thesis is to show the influence of X-ray photoevaporation on the structure and long-term evolution of protoplanetary disks in the context of different stellar- and disk parameters by utilizing a 1+1D hydrodynamic code with an implicit integration scheme. Both the influence of a magnetic star-disk coupling and the effect of including a dead zone on the photoevaporative disk dissolution are investigated. Furthermore, the impact of recurring, episodic accretion events, caused by thermal instability, on the dispersal process and timescale is studied.
Methods. Pre-calculated photoevaporative mass loss profiles, resulting from heating by different spectra of stellar X-ray radiation, are implemented into the fully implicit, 1+1D TAPIR code, which is then used to solve the full set of axisymmetric hydrodynamic equations and simulate the long-term evolution of low-mass protoplanetary disks. The model includes the star-disk connection via the stellar magnetic field and a layered viscosity description, which leads to a self-consistent development of dead zones and may result in episodic accretion behaviour for certain ranges of disk- and stellar parameters. The implicit integration scheme combined with an adaptive timestep and an adaptive numerical grid allows for a self-consistent treatment of the processes in the inner disk while simultaneously maintaining reasonable timesteps for conducting long-term simulations.
Results. The time and location of the creation of a photoevaporative gap is determined by the net radial mass transport rate, composed of radial mass in- and outflow, and photoevaporative mass loss. The net accretion mass transport rate is dependent on the initial model, effective α-viscosity and pressure gradients, which are also influenced by photoevaporation. Hence, the prediction of a gap location is a complex, dynamic, non-linear problem. Pressure gradients and radial angular momentum transport lead to a mass flux inversion at the outer edge of the dead zone as soon as photoevaporation reduces the inward mass flux to zero at this location. The magnetic torque at the inner boundary is responsible for the extension of the flux inversion over the whole disk. Due to the dead zone and the regulation of accretion by the magnetic torque, photoevaporative gaps can be created and expanded in the outer disk while the accretion rate stays high. Smaller viscosities and higher stellar X-ray luminosities facilitate gap

creation, whereas a large MRI-viscosity and episodic accretion events can prevent it entirely.
Conclusions. Including a dead zone and stellar magnetic torques to photoevaporating disk simulations can be a useful method of recreating disks with large gaps and high accretion rates, which are commonly observed but previously unexplained by the photoevaporation scenario. The results show, that incorporating a photoevaporation model into the TAPIR code can not only reproduce existing results, but can provide valuable additions to this field of research.

Zusammenfassung

Kontext. Protoplanetare Scheiben sind die Geburtsstätten von Planetensystemen, was sie zu interessanten Objekten für astrophysikalische Untersuchungen macht. Die kurzen Zeiträume, in denen sich solche Strukturen auflösen, verglichen zu ihren längeren Entwicklungszeitskalen, stellt ein viel diskutiertes Problem in diesem Feld dar. Die Evaporation von Scheibenmaterial durch die Strahlung des zentralen Sterns kann eine vielversprechende Lösung sein. Aber entsprechende numerische Simulationen können übliche Beobachtungen von sich auflösenden Scheiben noch nicht reproduzieren.
Ziele. Ziel dieser Arbeit ist es, den Einfluss von Röntgen-Photoevaporation auf die Entwicklung von protoplantaren Scheiben mit Berücksichtigung verschiedener Stern- und Scheibenparameter durch vielseitige, implizite 1+1D Simulationen zu zeigen. Außerdem soll auf die Wichtigkeit der innersten Scheibenregionen, die von toten Zonen und magnetischen Momenten beeinflusst werden, für die Zeitskalen und Strukturen von auflösenden Scheiben hingedeutet werden.
Methoden. Existierende, Röntgen-photoevaporative Massenverlustprofile werden in den impliziten, 1+1D TAPIR Code implementiert. Dieser löst das Set an achsensymmetrischen, hydrodynamischen Gleichungen um die Langzeitentwicklung von massearmen Scheiben zu simulieren. Das Modell beinhaltet magnetische Momente durch das stellare Magnetfeld und erlaubt die Entstehung von toten Zonen und episodischen Akkretionsausbrüchen. Das implizite Integrationsschema, kombiniert mit einem adaptiven Zeitschritt, ermöglicht die selbstkonsistente Modellierung der innersten Scheibenregionen.
Ergebnisse. Zeit und Ort der Bildung einer Lücke in der Scheibe durch Photoevaporation wird durch das delikate Zusammenspiel von Massenfluss durch die Scheibe und photoevaporativer Massenverlustrate bestimmt. Eine Inversion des Massenflusses am Außenrand der toten Zone wird produziert sobald die Photoevaporation den Massenfluss von außen an dieser Stelle vernichtet hat. Das magnetische Moment am Scheibeninnenrand führt zu einer Ausbreitung der Flussinversion über die gesamte Scheibe. Durch die tote Zone und die Regulierung der Akkretion durch das magnetische Moment können photoevaporative Lücken in der äußeren Scheibe produziert und aufgeweitet werden während die Akkretionsrate auf den Stern hoch bleibt. Kleinere Viskositäten und höhere Röntgen-Leuchtkräfte erleichtern die Entstehung von Lücken, während eine große MRI-Viskosität und Akkretionsausbrüche sie gänzlich verhindern können.
Schlussfolgerung. Die Berücksichtigung von toten Zonen und stellaren magnetischen Momenten ist eine nützliche Methode um Scheiben mit großen Lücken und hohen Akkretionsraten zu erzeugen. Diese können häufig beobachtet, aber noch nicht durch Photoevaporation erklärt werden. Die Ergebnisse zeigen, dass die Implementierung einer Photoevaporationsbeschreibung in die einzigartige Funktionsweise des TAPIR Codes nicht nur existierende Modelle reproduzieren, sondern auch wertvolle Beiträge zu diesem Forschungsfeld liefern kann.

Contents

1 Introduction

The study of protoplanetary disks represents a highly active field of research in modern astrophysics, since their structure and their evolution provide the foundation for the formation of planets. More specifically, the dispersal and the corresponding lifetimes of disks put constraints on the timescales and the conditions under which planet formation has to occur. According to observations, the lifetimes of protoplanetary disks rarely exceed 10 Myr. This results from studies of stellar clusters and the construction of relations between the age of the cluster and the fraction of stars which retain a disk (Haisch, Jr. et al. 2001; Williams & Cieza 2011; Ribas et al. 2014). In these investigations, they assumed an exponential drop in disk fraction with cluster age. The e-folding time for the exponential decay function depends on the observed wavelength and lies at 2 - 3 Myr for near infrared ($\sim$3 μm) and at 4 - 6 Myr for $\sim$22 μm. Since the longer wavelenghts trace dust further away from the central star, this finding could suggest an inside out clearing of the disk as it evolves in time (e.g. Owen 2016). Disks, which are currently in the process of dissolving - meaning transitioning from optically thick to optically thin, typically showing large gaps or cavities in their dust distribution (e.g. Gorti et al. 2016; Owen 2016)- are known as transition disks. During this phase, no near infrared excess is measured, whereas the disk still appears optically thick at larger wavelengths. Such disks typically make up only around 10% of confirmed disk observations in clusters (Williams & Cieza 2011), suggesting that this phase lasts only for a few 10^5 yr. So the timescale on which a protoplanetary disk evolves (at least as long as it is optically thick) seems to be significantly different from the dispersal timescale. Standard viscous evolution models fail to adequately describe this phenomenon (Owen 2016). One of the most promising approaches to conquer this problem is the consideration of photoevaporative processes in the disk caused by stellar irradiation. Far ultraviolet (FUV, h$\nu \leq$ 13.6 eV), extreme ultraviolet (EUV, hν > 13.6 eV) and X-ray radiation (hν $\gtrsim$ 100 eV) are capable of removing mass from protoplanetary disks by increasing the thermal energy of the disk material to a point where it can escape the gravitational potential (e.g. Ercolano & Pascucci 2017; Pascucci et al. 2022). The photoevaporation of disks was first investigated in the context of EUV heating by Hollenbach et al. (1994), who found that outside the so called gravitational radius ($r_{\rm g} = GM_\star/c_{\rm s}^2$, with G being the gravitational constant, $M_\star$ the stellar mass and $c_{\rm s}$ the isothermal sound speed), a photoevaporative wind develops, which can lead to mass loss rates of the order of 10^{-10} $M_\odot$/yr. However, these first calculations were made without considering the viscous evolution of the disk. Since then, the theory of photoevaporation has progressed to a great extent. Clarke et al. (2001) recognised that mass loss through photoevaporative processes in combination with viscous evolution leads to the opening of a gap in the disk as soon as the photoevaporation rate and the accretion rate onto the central star become comparable. The inner disk is then cut off from resupply of material from the outer part, which leads to a quick draining of the inner disk onto the star on the viscous timescale. Alexander et al. (2006) argued that the consequent exposure of the outer part of the disk to the direct irradiation from the central star leads to a larger photoevaporative mass loss rate than previously assumed, which disperses the disk more quickly. These basic ideas (creation of a gap $\rightarrow$ rapid draining of the inner disk $\rightarrow$ direct irradiation of the outer disk) have basically remained the same due to the promising outlook of this process to explain the 'two-time-scale behaviour' of disk evolution. On the other hand, the calculation of the mass loss rates has undergone a more significant evolution. While Hollenbach et al. (1994) proposed a semi-analytic model for EUV heating and the corresponding mass loss due to the photoevaporative wind, the consideration of X-ray (e.g. Owen et al. 2010, 2011, 2012) and FUV radiation (e.g. Gorti & Hollenbach 2008; Wang & Goodman 2017; Nakatani et al. 2018) resulted in significantly higher mass loss rates due to the ability of these high energy radiation fields to penetrate much larger column densities. Therefore, while EUV radiation mainly influences only the uppermost particles of the disk in a certain small surface area, FUV and X-ray are capable of heating disk material closer to the disk midplane and at much larger radii, also creating significant photoevaporative winds in the outer parts of the disk. The investigation of which energy regimes yield photoevaporation rates capable of explaining observations of disk dispersal has been and is still widely discussed (e.g. Owen et al. 2012; Ercolano & Pascucci 2017; Pascucci et al. 2022). X-ray induced photoevaporation is thought to be most effective at radii smaller than 100 AU (Owen et al. 2012), whereas FUV irradiation can result in efficient heating at larger distances (Gorti & Hollenbach 2008). Furthermore, the modelling of global photoevaporation rates resulting from X-ray heating has progressed greatly (Owen et al. 2010; Picogna et al. 2021; Ercolano et al. 2021) while FUV mass loss rates are still uncertain (e.g. Pascucci et al. 2022). Owen et al. (2012) also argue that in the presence of X-ray heating, FUV- and EUV-driven photoevaporation only play a minor role at distances below 100 AU. Therefore, for simulating low-mass disks with radial extents of around 100 AU, the implementation of X-ray photoevaporation is justified.

The photoevaporation-scenario of disk dispersal can be used to explain observations of transition disks which show low accretion rates ($< 10^{-9}$ $M_\odot$ yr^{-1}) and only small dust cavities, extending to radii of up to 30 AU (Owen 2016; Pascucci et al. 2022). An open problem for this model is to produce transition disks with large gaps and high accretion rates (Owen 2016; Pascucci et al. 2022), which are frequently observed (e.g. Van Der Marel et al. 2016; Francis & van der Marel 2020). The reason for that is that in the 'standard' picture of photoevaporation developed since Clarke et al. (2001), the inner disk accretes onto the star too quickly, such that the accretion rate diminishes before the photoevaporative gap can extend to larger radii (e.g. Owen 2016). Several approaches have been made to conquer this problem, such as the intensification of photoevaporation in disks depleted of carbon (Wölfer et al. 2019) or magnetized winds which keep the accretion rate high (Wang & Goodman 2017). Morishima (2012) was the first to propose that photoevaporative gaps can be opened at large radii when a layered accretion model (e.g. Gammie et al. 1996) is considered. In that case, a dead zone in the inner disk can develop within which the viscosity is significantly decreased by the suppression of ionization and therefore the efficiency of the magnetorotational instability (MRI) is reduced (Balbus & Hawley 1997). Due to the resulting larger viscous timescale in the dead zone, the gap can expand outwards while the accretion rate from the inner disk (within which photoevaporation is not effective) onto the star stays high. Gárate et al. (2021) expanded on this idea by implementing recent X-ray photoevaporation models (Picogna et al. 2019) into hydrodynamic simulations of disks with dead zones and found that large gaps in disks maintaining a high accretion rate may indeed be reproducible with this method. However, in their studies, they used a simplified model for the viscous evolution of the protoplanetary disk, implementing the commonly used diffusion equation (Lynden-Bell & Pringle 1974). This method neglects the influence of pressure gradients and disturbances in the rotational velocity of the disk, which can become important during the creation of a gap (e.g. Zhang et al. 2018). Furthermore, little attention has been paid in the past to the innermost parts (< 1 AU) of the disk, closest to the star. The connection between the star and the inner regions of the disk via the stellar magnetic field can have significant effects on the long-term evolution of the disk (Steiner et al. 2021). Although the magnetic torques resulting from this coupling do not interfere directly with photoevaporation (which becomes effective at larger radii), the interplay between these two processes could have important influences on the late stages of disk evolution. These can result e.g. from the propelling effect on the disk material at the inner boundary, caused by the stellar magnetic field (Illarionov & Sunyaev 1975), which can eject matter radially away from the central star rather than letting it accrete onto the star. The question if this ejected material can reach the photoevaporation regime at larger radii will be explored in this thesis. Moreover, the development of a dead zone can facilitate the occurrence of thermal instability-induced episodic accretion events (e.g. Bell & Lin 1994), which can be observed even in disks with masses of around 0.01 $M_\odot$ (e.g. Kóspál et al. 2016). Steiner et al. (2021) showed that the star-disk connection via the stellar magnetic field can have a significant influence on the appearance of accretion outbursts and the detailed burst structures. Since the inner disk has to be refueled with material from the outer disk after an accretion outburst, the mass loss due to photoevaporation may result in an alteration of the disk's outburst behaviour.

In this thesis, the fully implicit 1+1D TAPIR code (Ragossnig et al. 2020) is used to investigate the long-term evolution of protoplanetary disks undergoing X-ray photoevaporative processes while at the same time self-consistently modeling the innermost parts of the disk. For this, a model including recent X-ray photoevaporative mass loss calculations (Ercolano et al. 2021) is included into the model described by Ragossnig et al. (2020), which then allows to investigate the impact of the star-disk connection on the long-term evolution of a photoevaporative disk. Furthermore, a layered accretion model is used (Gammie et al. 1996) which leads to the development of a dead zone in the inner disk, in order to expand on the ideas of Morishima (2012) and Gárate et al. (2021) and allow thermal instability-induced episodic accretion events to occur. For the consideration of steep pressure gradients and magnetic torques, the solution of the full set of hydrodynamic equations is necessary, which will be done assuming axisymmetry with an implicit integration scheme. For a comprehensive study of how this model influences the long-term behaviour of a protoplanetary disk, several stellar- and disk parameters will be varied and the resulting disk models will be compared to each other and to the same simulations without photoevaporative mass loss. In Sec. 2, the underlying theory of photoevaporation in protoplanetary disks will be explored. Sec. 3 is dedicated to explain in detail the physical and numerical setup of the TAPIR code used for all simulations. In Sec. 4, the results of the simulations will be presented and subsequently discussed and compared to previous work in Sec. 5. Furthermore, Sec. 5 includes an analysis of the limitations of the used model. Finally, the most important conclusions and an outlook on future work will be described in Sec. 6.

2 Theory of photoevaporation

The basic principle of the physical process of photoevaporation is straightforward: Radiation coming from the central star or the stellar environment around the star-disk system induces heating in the material of the protoplanetary disk until its thermal energy exceeds the gravitational potential, which leads to an escape of particles, driven by thermal gradients in the disk. It is important to realize that radiation of different energy regimes has different properties in terms of heating disk material and driving a wind (e.g. efficiency, area of effect, heating mechanism). Therefore, the question of which (combination of) radiation fields can be responsible for significant photoevaporative mass loss to produce disk structures and lifetimes in agreement with observations, is crucial.

2.1 EUV photoevaporation

Hollenbach et al. (1994) were the first to study the effects of photoevaporation around young, massive stars considering strong EUV radiation fields. The characteristic gravitational radius r_g is defined by equating the sound speed with the keplerian angular velocity:

$$c_\mathrm{s} = \sqrt{\frac{GM_\star}{r_\mathrm{g}}} \quad \Rightarrow \quad r_\mathrm{g} = \frac{GM_\star}{c_\mathrm{s}^2} \quad , \tag{2.1.1}$$

where G is the gravitational constant, $M_\star$ the mass of the central star and c_s the speed of sound. If EUV is the only source of heating taken into account, Hollenbach et al. (1994) argue that within r_g disk material is still gravitationally bound and an atmosphere of ionized plasma is created due to the EUV radiative flux from the star. The EUV photons do not reach the disk regions outside of r_g directly as long as the inner disk is present, but are absorbed in the atmosphere and a diffuse radiation field is created by recombination processes. This diffuse radiation heats the outer parts of the disk, leading to an escape of the ionized gas. The amount of mass lost to this photoevaporative wind is determined by the density ρ_base and the sound speed at the base of the flow,

$$\dot{\Sigma}_\mathrm{ph}(r) \propto \rho_\mathrm{base}(r) \cdot c_\mathrm{s}(r) \quad , \tag{2.1.2}$$

where $\dot{\Sigma}_\mathrm{ph}(r)$ is the loss in column density due to photoevaporation at a radius $r > r_\mathrm{g}$. As argued by Hollenbach et al. (1994), in case of purely EUV driven photoevaporation, the radially integrated total mass loss $\dot{M}$ scales with the EUV flux Φ_EUV coming from the central star with,

$$\dot{M} \propto \sqrt{\Phi_\mathrm{EUV}} \quad . \tag{2.1.3}$$

Adams et al. (2004) found that significant mass loss can also occur at radii smaller than the gravitational radius by launching a subsonic flow at $r > 0.2 r_\mathrm{g}$. Combining these findings with viscous evolution of the disk shows the effect of photoevaporation on the disk structure throughout its lifetime. Since the mass loss through accretion onto the central star scales with disk density and viscosity, the accretion rate declines with time as the remaining mass and therefore the density in the disk becomes smaller. On the other hand, the photoevaporation rate stays fairly constant throughout the disk lifetime. This is because the radiation from the central star responsible for heating and the launching of a photoevaporative wind has a certain penetration depth depending on the column density the photons have to pass through. In the case of EUV radiation, this penetration depth is rather small since EUV photons can easily be absorbed within a column density of $\sim 10^{20}$ neutral hydrogen particles per cm^2 (e.g. Ercolano & Pascucci 2017). Therefore, although the overall density of the disk decreases, the density at the base of the flow, which determines the evaporative mass loss (Eq. 2.1.2), does not follow this decrease since the penetration depth of the photons adapts itself according to the column density passed through. As soon as the accretion rate drops to values comparable to the photoevaporation rate, the accretion process throughout the disk is unable to compensate for the mass loss through the wind and a gap opens in the disk in proximity of the gravitational radius, as realized by Clarke et al. (2001) (who used the term 'ultraviolet switch' for this phenomenon). With the inner part of the disk now being cut off from resupply of material, it drains onto the star on the viscous timescale of order 10^5 yr according to the prevalent picture.

Although the study of disk heating by EUV radiation laid the foundation of our under-standing of photoevaporation in protoplanetary disks, EUV radiation alone is unlikely to cause mass loss rates large enough to have a significant impact on the disk evolution due to the small penetration depth of EUV photons (e.g. Ercolano & Pascucci 2017). Therefore it is obvious to look for radiation in other energy regimes which can also induce evaporative processes in the disk while not being absorbed as easily as EUV radiation.

2.2 X-ray photoevaporation

In this thesis, photoevaporation is implemented in the simulations in the context of X-ray heating, while radiation from other energy regimes does not contribute to the photoevaporative mass loss. This section lays the foundation of this approach.

2.2.1 EUV vs. X-ray

Pioneering work on the effects of X-ray radiation on the heating of protoplanetary disks was conducted by Alexander et al. (2006), who were the first to conclude that a thermally driven wind can be developed by X-ray heating, although the corresponding estimated mass loss resulting from their calculations was too small compared to the EUV photoevaporation to have a significant influence. Ercolano et al. (2008) and Ercolano et al. (2009) used the three-dimensional radiative transfer code `MOCASSIN` (Ercolano et al. 2003) to create a photoionization and dust radiative transfer model in combination with the self-consistent calculation of the hydrostatic structure of a disk irradiated by a synthetic X-ray spectrum. They conclude that X-ray radiation may in fact be the dominant factor of driving photoevaporation with estimated mass loss rates of 10^{-8} $M_\odot$/yr. Owen et al. (2010) created the first radiation-hydrodynamic model of X-ray photoevaporation by including a new method of calculating the temperature of gas irradiated by X-ray and EUV radiation into an hydrodynamic code in order to determine accurate mass loss rates and photoevaporative flow structures. They argue that the gas temperature can be calculated as a function of the ionization parameter (Tarter et al. 1969) ,

$$\xi = \frac{L_\mathrm{X}}{nr^2} \quad , \tag{2.2.1}$$

where L_X is the X-ray luminosity of the central star, n is the gas particle density and r is the distance from the star. The numerical relation between the ionization parameter and the gas temperature was constructed based on the model by Ercolano et al. (2009) and thereby it was confirmed that this computationally cheaper method of determining the gas temperature yields results within small margins of error compared to the radiative transfer calculations. Using this temperature description, they performed 2D hydrodynamic simulations to find steady-state solutions for the photoevaporative flow and further determine mass loss profiles and integrated mass loss rates for primordial

disks and disks with inner cavities. These results were then implemented in viscous evolution simulations to show that they can indeed recreate the dispersal mechanism of a protoplanetary disk influenced by photoevaporation. Owen et al. (2010) confirmed the predicted mass loss rates of $\sim 10^{-8}$ $M_\odot$/yr by Ercolano et al. (2009) and used a two-phase model of photoevaporation to differentiate between the mass loss of the primordial disk and the disk once an inner hole has been created and the outer disk is irradiated directly by the star (as described by Alexander et al. 2006). Since the mass loss rate in their model is around two magnitudes larger than that of purely EUV driven evaporation, Owen et al. (2010) argue that in the presence of X-ray radiation, EUV heating plays an insignificant role.
The key differences between EUV and X-ray photoevaporation which lead to the discrepancy in mass loss rates are as follows:

i While EUV heating acts predominantly through a diffuse radiation field and produces an isothermal wind of ionized plasma, the disk material is directly illuminated by X-ray radiation, heating the disk by photoelectric effects and leading to a variety of escape speeds depending on the radius, which makes the treatment of X-ray heating more complex.

ii X-ray radiation affects a much larger portion of the disk surface (ranging from ~1 - 70 AU). EUV on the other hand has its influence limited to at most a few AU around the gravitational radius.

iii The penetration depth of these two radiation energy regimes differs by two orders of magnitude. EUV radiation can only penetrate neutral hydrogen particle column densities of 10^{20} cm^{-2}, while for X-rays the value lies at about 10^{22} cm^{-2} (e.g. Ercolano & Pascucci 2017).

Furthermore, Owen et al. (2012) argue that in the presence of X-ray photoevaporation, EUV radiation can be neglected regardless of the difference in mass loss rate. The reason for that is that a X-ray driven wind produces streamlines from the inner parts of the disk with an ionization fraction already low enough so that EUV radiation can not penetrate through. As a result, the EUV photons never reach the disk surface and can therefore not contribute to the disk mass loss rate.

2.2.2 From X-ray irradiation to disk mass loss

The parametrization of the gas temperature in the disk via the ionization parameter given in Eq. 2.2.1 has important consequences regarding the dependence of the photoevaporative mass loss on stellar and disk parameters. This was explored in depth by Owen et al. (2012) and the most relevant points will be presented here. As shown in

Eq. 2.1.2, the mass loss at a fixed distance from the central star is determined by the density at the base of the flow and the sound speed. Under the assumption of a steady-state flow, the mass flowing along a streamline is conserved. Therefore, the mass loss can also be evaluated at any other point along the streamline. If chosen to do so at the location where the flow transitions from sub-sonic to super-sonic (the 'sonic surface'), the total mass loss rate due to a photoevaporative flow can be written as,

$$\dot{M}_{\mathrm{ph}} = 2\int_0^\infty 2\pi r \rho_{\mathrm{s}}(r) c_{\mathrm{s}}(r) dr = 4\pi\mu \int_0^\infty r n_{\mathrm{s}}(r) c_{\mathrm{s}}(r) dr \quad , \tag{2.2.2}$$

where $\rho_{\mathrm{s}} = \mu\ n_{\mathrm{s}}$ is the density at the sonic surface, with μ being the mean particle weight and n_{s} the particle density at the sonic surface. The factor 2 accounts for the mass loss from both sides of the disk. When considering disk winds, the speed of sound at the sonic surface can be estimated by approximating the flow as a Parker wind (Parker et al. 1958). A careful application of the Parker wind solution to disk winds was done by e.g. Waters & Proga (2012). Under disk wind conditions (see Owen et al. 2012) the sound speed at the sonic surface then takes the form,

$$c_{\mathrm{s}}(r) = \sqrt{\frac{GM_\star}{2r}} \quad , \tag{2.2.3}$$

where G is the gravitational constant and $M_\star$ the mass of the central star. By assuming ideal gas, the above expression can be equated to,

$$c_{\mathrm{s}}(r) = \sqrt{\frac{GM_\star}{2r}} = \sqrt{\frac{\gamma k_{\mathrm{B}} T_{\mathrm{gas}}}{\mu}} \quad , \tag{2.2.4}$$

with γ being the adiabatic index (which equals unity in the isothermal Parker wind), k_{B} the Boltzmann constant and T_{gas} the gas temperature. As described above, in the case of X-ray heating, T_{gas} can be expressed as a function of ξ (Eq. 2.2.1),

$$T_{\mathrm{gas}} = f(\xi) = f\left(\frac{L_{\mathrm{X}}}{nr^2}\right) \quad , \tag{2.2.5}$$

where the form of $f(\xi)$ has to be calculated numerically (which was done by e.g. Owen et al. 2010). Evaluating this at the sonic surface and inserting it in Eq. 2.2.4, we can get an expression for the particle density at the sonic surface after rearrangement,

$$n_{\mathrm{s}}(r) = \frac{L_{\mathrm{X}}}{r^2}\left(f^{-1}\left(\frac{GM_\star\mu}{2k_{\mathrm{B}}r}\right)\right)^{-1} \quad . \tag{2.2.6}$$

This result provides a coupling between the density and the sound speed at the sonic surface. Due to the conservation of mass along a steady-state flow streamline, Eqs. 2.2.2, 2.2.3 and 2.2.6 provide a way to calculate the integrated mass loss over the whole disk without referring to the properties of the disk. Therefore, the mass loss due to X-ray photoevaporation is determined by the X-ray properties of the star alone. These considerations cannot be made in the case of EUV heating, where the flow has to adapt to the disk structure and dynamics. In the case of X-rays, the reverse is true: The disk adapts itself according to the mass loss determined by the stellar properties. By changing the integration variable in Eq. 2.2.2 from the radius to the escape temperature (for details, see Owen et al. 2012), the scaling of the mass loss rate becomes clearer,

$$\dot{M}_{\mathrm{ph}} \propto L_{\mathrm{X}} \quad . \tag{2.2.7}$$

This means that on the one hand, the total mass loss rate should scale approximately linearly with the X-ray luminosity of the star and on the other hand, it indicates that the mass loss is not explicitly dependent on the stellar mass. But since there seems to be a relation between the mass and the X-ray luminosity of T-Tauri stars (e.g. Telleschi et al. 2007; Bustamante et al. 2016), the stellar mass has indirect influence on the photoevaporation rate.

The previous analytic considerations were made with significant simplifications. In order to test their reliability, numerical simulations of the wind streamline structure are necessary. In addition to that, such simulations are crucial to find actual mass loss profiles along protoplanetary disks. The formalism discussed above describes the evaporation rate as determined at the sonic surface, which can provide a good estimate of the total mass loss rate. But since it is unknown how the streamlines connect from the actual base of the flow to the sonic surface, it is not useful for deriving detailed mass loss profiles. Therefore, Owen et al. (2010, 2011, 2012) conducted numerical simulations of photoevaporating disks by using the gas temperature description via the ionization parameter. For that, they considered both primordial disks and disks with a cleared out inner cavity and covered a large range of stellar masses, X-ray luminosities and inner hole sizes. Indeed they could confirm that the mass loss rates are not explicitly dependent on the stellar mass and inner hole sizes and they did not find a relation between the disk wind and the underlying disk structure. With their results, they also provided numerical fits to the mass loss profiles along the disk out to a radius of $\sim$70 AU to be used in viscous disk evolution simulations.

It has to be pointed out that while the disk mass and structure may not have a significant effect on the photoevaporative mass loss, they obviously do influence the evolution of a disk subject to photoevaporation. Ultimately, it is the interplay between total disk mass, mass flux through the disk (determined i.a. by viscosity) and photoevaporation that determines the time and place of gap opening and the remaining mass in the outer disk to be evaporated after inner disk draining. This means that due to the scaling of mass loss with X-ray luminosity only, the resulting lifetime of the disk in evolutionary calculations may be a function of X-ray luminosity but also heavily influenced by the

viscosity model used for the viscous evolution.
Furthermore, the calculated mass loss rates may be an overestimation since certain processes can be responsible for hindering the X-ray photons from reaching the disk surface. Similar to the screening of EUV by X-ray photoevaporative winds, magnetically driven winds or accretion funnels can generate column densities of > 10^{22} cm $^{-2}$ close to the star, absorbing the stellar X-ray radiation before it can reach the disk surface.
The X-ray photoevaporation model of Owen et al. (2010, 2011, 2012) was improved upon by Picogna et al. (2019), who modified the temperature-ionization parameter relation to also account for different column densities towards the star. Therefore, while using the same method, the new models describe the mass loss (especially in the outer regions) of the disk more accurately, leading to improved mass loss profiles. Interestingly, they find that the mass loss rates are in fact not linear with respect to the X-ray luminosity, but saturate at high luminosities where the ionization parameter vs. gas temperature function becomes constant, starting at a gas temperature of approximately 10^4 K. The reason for such a saturation is that strong X-ray radiation fields drive a strong wind from the inner parts of the disk, which itself can already absorb large amounts of stellar radiation, narrowing the area of the X-ray heating effect, as argued by Ercolano et al. (2021). The mass loss rate as a function of X-ray luminosity as calculated by Picogna et al. (2019) compared to that of Owen et al. (2012) is shown in Fig. 2.1.

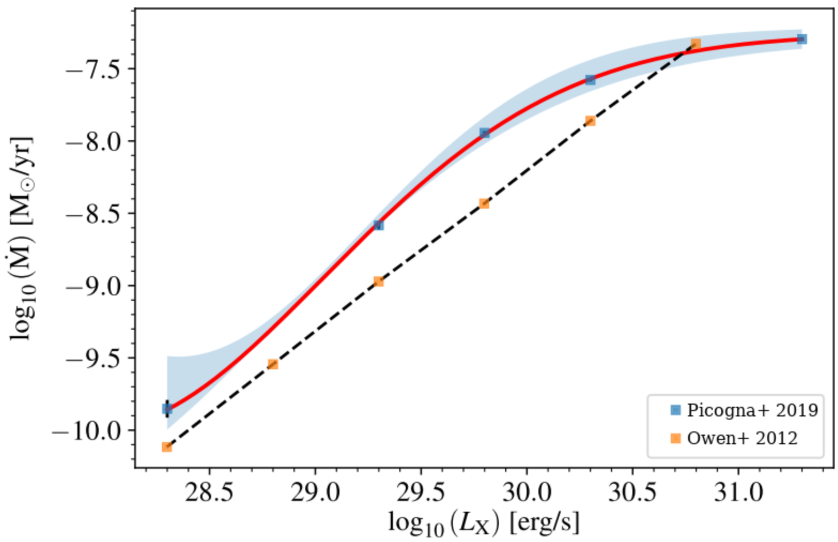

Figure 2.1: Mass loss rate as a function of stellar X-ray luminosity. While the relation is linear in the calculations of Owen et al. (2010, 2012), a more sophisticated treatment of the temperature-ionization parameter relation yields a non-linear function, calculated by Picogna et al. (2019). The blue shaded area around the model of Picogna et al. (2019) represents regions of uncertainty, resulting from multiple simulation runs with different numerical resolutions (This figure originates from Picogna et al. 2019).

As already found by Ercolano et al. (2009), the 'hardness' of the X-ray spectrum of the central star plays an important role when considering photoevaporative mass loss rates. They conclude that 'soft' X-rays (with energies < 1 keV) dominate the heating process, while 'hard' X-rays are incapable of driving a significant wind. Further indications for this was provided by e.g. Wang & Goodman (2017) and Nakatani et al. (2018), who used X-ray spectra dominant in the high energy regime (> 1 keV) and found no significant mass loss due to X-ray heating. For that reason, Ercolano et al. (2021) used three different X-ray spectra, representing X-ray luminosities of 10^{29} erg/s, 10^{30} erg/s and 10^{31} erg/s, which increase in 'hardness' as the luminosity becomes larger. These spectra were synthesized based on observational emission data. The authors used the temperature-ionization parameter relation from Picogna et al. (2019) to derive new evaporative mass loss profiles and found on the one hand, that indeed the mass loss is mostly controlled by the soft part of the X-ray spectrum and on the other hand, that the choice of the irradiating X-ray spectrum has a large influence on the evolution of the disk concerning gap opening and disk dispersal time. They argue that good estimates of the evaporation rates can be achieved by considering the soft part of the stellar X-ray spectrum only (< 1 keV). Picogna et al. (2019) and Ercolano et al. (2021) created these mass loss profiles on the basis of hydrodynamic simulations of disks surrounding a star with a mass of 0.7 $M_{\odot}$. Picogna et al. (2021) used the same methods to investigate the influence of the stellar mass on the photoevaporative mass loss. Contrary to the considerations of Owen et al. (2012), they found that due to the difference in structure of the protoplanetary disk around stars with different masses, the X-ray irradiation causes photoevaporative winds which are not independent of stellar mass. A linear relation between the integrated mass loss rate and stellar mass was found as well as different structures of the mass loss profiles. As a result, the long-term evolution regarding gap opening and disk draining is also influenced by the stellar mass.
When describing X-ray photoevaporation, the mass loss profiles obtained by Owen et al. (2010, 2012) are still widely used (e.g. Kunitomo et al. 2020; Rodenkirch et al. 2020), but due to the arguments described above, the models of Ercolano et al. (2021), which are an extension of the ones constructed by Picogna et al. (2019), will be used in this thesis. The stellar mass dependence of the profiles as argued by Picogna et al. (2021) will not be discussed any further.

2.3 FUV photoevaporation

Unlike in the case of X-rays, heating of the disk by FUV radiation strongly depends on the disk properties. FUV photons get absorbed by small dust grains, including polycyclic aromatic hydrocarbons (PAH), which collisionally heat the surrounding gas by sending out energetic electrons (e.g. Gorti & Hollenbach 2008). Therefore the chemical composition has to be considered when investigating FUV photoevaporation. Due to the dependence on the presence of dust grains, the penetration depth of FUV photons can be considerably larger than that of X-rays, leading to an enhanced mass loss rate in the outer parts of the disk. Gorti & Hollenbach (2008) and Gorti et al. (2009) created models for photoevaporating disks including FUV heating and found mass loss rates of the same order as with X-ray heating, calculated by Owen et al. (2010). They note that FUV evaporation is most effective at larger distances from the star (>100 AU), but, combined with X-ray heating, can contribute significantly to the mass loss in the inner parts as well. Owen et al. (2012) argue that for the inner parts of the disk, FUV evaporation should only play a subordinated role in the presence of X-ray heating. In the regions of the inner disk which are heated by both X-rays and FUV radiation, the effect of X-ray heating dominates. But depending on the disk chemistry, FUV photons can penetrate larger column densities and could therefore launch flows from deeper within the disk, where the density is higher. However, at the radii where there is a purely FUV heated region in the deeper parts of the disk (at column densities of > 10^{22} cm^{-2}), the sonic surface lies above that region in the layers which are predominantly heated by X-rays. As described in the previous section, the mass flux at the sonic surface in an X-ray heated medium is set by the X-ray physics of the central star alone (while being a function of the distance from the star) and is independent of the underlying disk structure. The processes in the layers below the sonic surface have to result in a flow at the sonic surface given by the density in Eq. 2.2.6 and the sound speed in Eq. 2.2.4. Therefore, X-ray photoevaporation dominates the mass loss in the inner parts of the disk (< 100 AU). At larger radii, FUV is still able to provide sufficient heating to drive a wind, while most of the X-ray photons have already been absorbed before reaching such distances. That means that in the outer parts of the disk, the sonic surface lies in the FUV heated region, which makes FUV the dominant driver of a photoevaporative flow. A schematic picture of the X-ray and FUV dominated region respectively is shown in Fig. 2.2.

The true role of FUV heating in driving photoevaporative winds is still disputed. E.g. Nakatani et al. (2018) find that FUV seems to be the dominant factor throughout the whole disk and only aided by ionization by X-ray radiation. They do note, however, that the interplay between these radiation regimes when it comes to the importance in the context of photoevaporation, highly depends on the abundance of PAHs and the amount and size distribution of dust grains in the heated layers. Since these factors are still uncertain and difficult to model in simulations, results of FUV photoevaporation have to be taken with a grain of salt.

Due to these properties (dependence on chemical composition, dust treatment, ineffectiveness at radii < 100 AU), FUV photoevaporation will not be considered in this thesis.

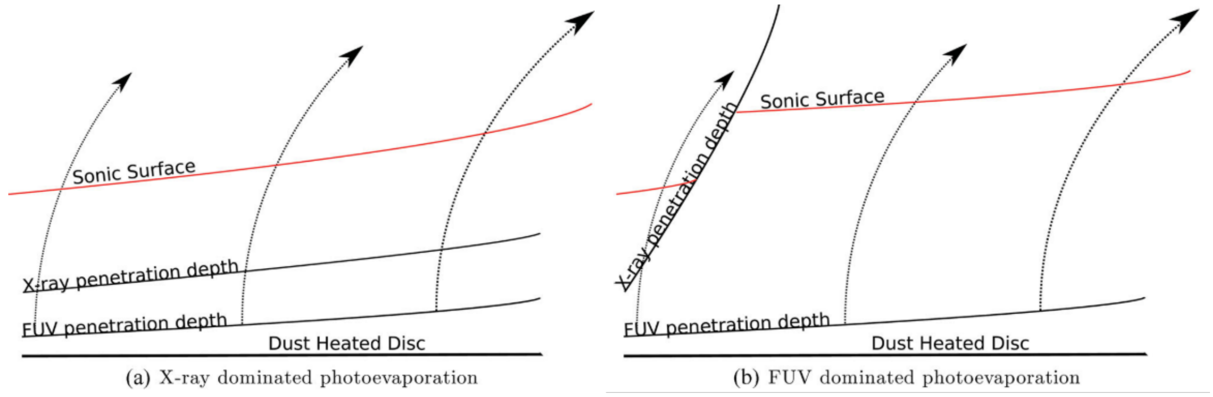

Figure 2.2: Photoevaporative flows from a disk irradiated by X-ray and FUV radiation. (a) In the inner parts of the disk, the flow starts at the penetration depth of FUV photons, but the sonic transition happens in the X-ray heated layer. (b) X-rays get mostly absorbed by the flows before reaching the disk surface in the outer disk, so the sonic surface lies in the FUV heated layer (This figure originates from Owen et al. 2012).

3 Methods

For this thesis, the cylindrical symmetric, fully implicit 1+1D TAPIR (**T**he **A**da**p**tive **I**mplicit **R**HD) code (Ragossnig et al. 2020, and references therein) is used to solve the full set of hydrodynamic equations which describe the viscous evolution of an axisymmetric protoplanetary disk in the thin-disk limit. The equations will be presented briefly and the implementation of the corresponding terms for the description of photoevaporation will be described in this section. Furthermore, the physical and numerical setup used for the simulations will be presented.

3.1 Hydrodynamic equations

For describing the surface density evolution of a photoevaporating viscous disk in time, the one-dimensional diffusion equation (e.g. Lynden-Bell & Pringle 1974) with an additional sink term for the photoevaporative mass loss is widely used (e.g. Gorti et al. 2009; Owen et al. 2010; Kimura et al. 2016; Kunitomo et al. 2021; Ercolano et al. 2021). It takes the form,

$$\frac{\partial \Sigma}{\partial t} = -\frac{1}{r}\frac{\partial}{\partial r}\left[\frac{1}{(\partial j/\partial r)}\frac{\partial}{\partial r}\left(r^3 \nu \Sigma \frac{\mathrm{d}\Omega}{\mathrm{d}r}\right)\right] - \dot{\Sigma}_{\mathrm{ph}} \quad , \tag{3.1.1}$$

where Σ is the surface column density, j the specific angular momentum, ν the kinematic viscosity, Ω the angular velocity and $\dot{\Sigma}_{\mathrm{ph}}$ the aforementioned photoevaporation sink term. As argued by Steiner et al. (2021), the inaccuracy of this simplified approach is non-negligible, especially when it comes to describing the processes in the innermost parts of the disk. Pressure gradients cannot be implemented in such a description and therefore, the angular velocity of the disk at all radii is assumed to be equal to the Keplerian velocity. However, processes such as the braking of the inner disk due to the connection with the stellar magnetic field or the occurrence of FU-Ori bursts can lead to significant changes in the radial and azimuthal velocity profiles, which have to be taken into account. Therefore, for the calculations in this thesis, the full set of hydrodynamic equations is used to simulate the long-term evolution of a protoplanetary disk. This set also includes an energy equation to account for heating and cooling mechanisms as well as radial energy diffusion and vertical radiation transport. The vertically integrated equations take the following form:

Equation of continuity:

$$\frac{\partial}{\partial t}\Sigma + \nabla(\Sigma\mathbf{u}) + \dot{\Sigma}_{\mathrm{ph}} = 0 \tag{3.1.2}$$

Equation of motion:

$$\frac{\partial}{\partial t}(\Sigma\mathbf{u}) + \nabla(\Sigma\mathbf{u}:\mathbf{u}) - \frac{B_{\mathrm{z}}\mathbf{B}}{2\pi} + \nabla P_{\mathrm{gas}} + \nabla\mathbf{Q} + \Sigma\nabla\psi + H_{\mathrm{p}}\nabla\left(\frac{B_{\mathrm{z}}^2}{4\pi}\right) + \dot{\Sigma}_{\mathrm{ph}}\mathbf{u} = 0 \tag{3.1.3}$$

Equation of energy:

$$\frac{\partial}{\partial t}(\Sigma e) + \nabla(\Sigma\mathbf{u}e) + P_{\mathrm{gas}}\nabla\mathbf{u} + \mathbf{Q}:\nabla\mathbf{u} - 4\pi\Sigma\kappa(J-S) + \dot{E}_{\mathrm{rad}} + \dot{\Sigma}_{\mathrm{ph}}e = 0 \tag{3.1.4}$$

The symbols contained in these equations denote the following quantities:

- Σ ... column density
- $\mathbf{u}$ ... velocity vector
- $\mathbf{B} = \begin{pmatrix} B_r \\ B_\varphi \\ B_{\mathrm{z}} \end{pmatrix}$ ... protostellar magnetic field
- P_{gas} ... vertically integrated gas pressure
- $\mathbf{Q}$ ... viscous pressure tensor
- ψ ... gravitational potential (disk + star)
- H_{p} ... pressure scale height
- e ... specific internal energy density
- κ ... opacity
- J ... mean radiation intensity
- S ... radiation source function
- $\dot{E}_{\mathrm{rad}}$ ... net radiation cooling or heating

Additionally, : represents the tensor product. The above equations and the meaning of the individual terms have been described by Ragossnig et al. (2020) and Steiner et al. (2021). One specific aspect which becomes important when a photoevaporative gap is created in the disk is the gas pressure gradient force density $-\nabla P_{\mathrm{gas}}$ in the equation of motion. When a negative gas pressure gradient is present, the corresponding force is directed away from the star, essentially working against the gravitational pull. Consequently, as explored in Steiner et al. (2021), when neglecting magnetic fields, radial viscous forces and momentum advection, the azimuthal velocity u_φ is influenced by the pressure gradient in the following way:

$$\frac{u_\varphi^2}{r} \approx \frac{GM_\star}{r^2} + \frac{1}{\rho}\frac{\mathrm{d}P}{\mathrm{d}r} \quad . \tag{3.1.5}$$

That means, a negative pressure gradient leads to a radially outward acceleration and azimuthal deceleration, whereas a positive pressure gradient has the opposite effect. Over the largest part of the disks radial extent, $\mathrm{d}P/\mathrm{d}r$ is usually negative, but the resulting forces are subdominant compared to the viscous friction forces in the context of the radial motion. But in regions where the absolute values of the gas pressure gradients become large and the surface density small, such as close to the inner boundary (where $\mathrm{d}P/\mathrm{d}r > 0$, which facilitates accretion, see Steiner et al. 2021) or in the vicinity of gaps, the corresponding forces can show a non-negligible influence.

For this thesis, the main focus lies on the last terms on the left hand side of the equations, since these terms describe the influence of photoevaporation via the mass loss rate $\dot{\Sigma}_{\mathrm{ph}}$ acting as a sink term.

3.1.1 Implementation of photoevaporation terms

The set of hydrodynamic equations shown above indicate, that the term describing the photoevaporative mass loss enters every equation. In the equation of continuity, $\dot{\Sigma}_{\mathrm{ph}}$ acts as a sink term, removing mass from the system. The equation of continuity without a sink- or a source term in general constitutes the conservation of mass. In such a case, the equation would take the form of Eq. 3.1.2 without the $\dot{\Sigma}_{\mathrm{ph}}$ term. It states that the temporal *change of the density* of a system can only depend on the flux of density through the borders of the system. Implementing a source or a sink term means that the density can also change through processes inside the system itself. Since $\dot{\Sigma}_{\mathrm{ph}}$ is a sink term, its sign has to be positive in the form of Eq. 3.1.2. The equation of motion 3.1.3 describes the temporal *change of momentum* in the according system. The removal of mass through evaporation therefore also has to be considered in the equation of motion, since that mass carries radial and angular momentum (described by $\dot{\Sigma}_{\mathrm{ph}}\mathbf{u}$) which is removed accordingly. This does not mean that the disk experiences some form of acceleration through photoevaporation, but merely that the total momentum content is reduced according to the decreased mass. If that term was not included in the equation of motion, the evaporated mass would leave a surplus of momentum

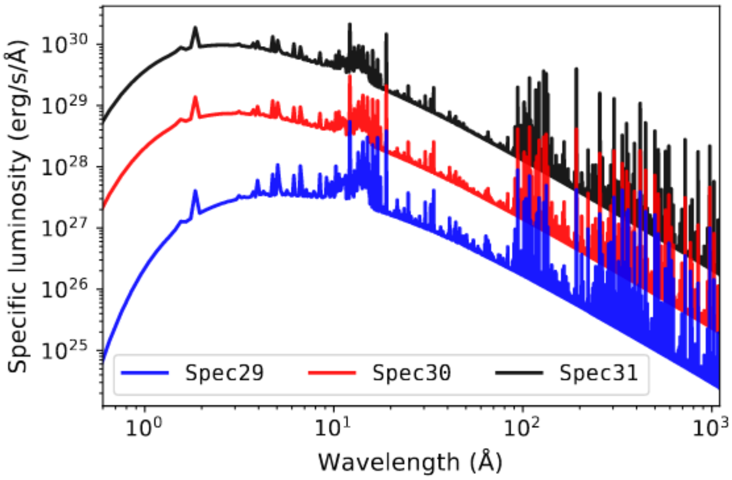

Figure 3.1: The three X-ray luminosity spectra used by Ercolano et al. (2021) for calculating the photoevaporative mass loss profiles. The blue spectrum corresponds to a stellar X-ray luminosity of 10^{29} erg/s while the red and black spectra correspond to 10^{30} erg/s and 10^{31} erg/s, respectively. (This figure originates from Ercolano et al. 2021).

behind which would then get redistributed onto the surrounding material, which would lead to an acceleration. The same argument can also be applied to the inclusion of the photoevaporation term into the equation of energy. Hereby, the amount of internal energy carried by the removed mass is described by $\dot{\Sigma}_{\mathrm{ph}}e$.

As described in Sec. 2.2, the mass loss profiles found by Ercolano et al. (2021) will be used to represent photoevaporation in the calculations in this thesis. The numerical fit to the profiles is described by,

$$\dot{\Sigma}_{\mathrm{ph}}(r) = \chi \ln(10)\left(\frac{6a\ln(r)^5}{\ln(10)^6} + \frac{5b\ln(r)^4}{\ln(10)^5} + \frac{4c\ln(r)^3}{\ln(10)^4} + \frac{3d\ln(r)^2}{\ln(10)^3} + \frac{2e\ln(r)}{\ln(10)^2} + \frac{f}{\ln(10)}\right)\frac{\dot{M}_{\mathrm{ph}}(r)}{2\pi r^2} \quad , \tag{3.1.6}$$

where r is the radial distance from the stellar surface, χ is a unit conversion factor with the value 0.2817 and $\dot{M}_{\mathrm{ph}}(r)$ is the cumulative mass loss rate, described by,

$$\dot{M}_{\mathrm{ph}}(r) = \dot{M}(L_{\mathrm{X,soft}})10^{a\log(r)^6 + b\log(r)^5 + c\log(r)^4 + d\log(r)^3 + e\log(r)^2 + f\log(r) + g} \quad , \tag{3.1.7}$$

where $\log$ is the logarithm in base 10. $\dot{M}(L_\mathrm{X})$ represents the stellar X-ray luminosity dependence of the mass loss rate and is given by,

$$\log(\dot{M}(L_{\mathrm{X,soft}})) = A_\mathrm{L}\exp\left[\frac{(\ln(\log(L_\mathrm{X})) - B_\mathrm{L})^2}{C_\mathrm{L}}\right] + D_\mathrm{L} \quad . \tag{3.1.8}$$

X-ray luminosity [erg/s]	10^{29}	10^{30}	10^{31}
a	-0.9152	0.3034	-1.2845
b	8.5032	-1.5323	9.3601
c	-32.0623	1.5766	-27.7371
d	62.8336	4.0211	42.9367
e	-67.9150	-11.1311	-37.3244
f	39.2652	10.6550	18.8216
g	-10.1113	-4.5769	-5.3780
A_L	$-1.947 \cdot 10^{17}$		
B_L	$-1.572 \cdot 10^{-4}$		
C_L	-0.287		
D_L	-6.694		

Table 3.1: Numerical coefficients used for the description of the photoevaporative mass loss profiles in Eqs. 3.1.6, 3.1.7 and 3.1.8.

The numerical coefficients a to g depend on the X-ray spectrum used. In this thesis, three different spectra, which are described by Ercolano et al. (2021) and are shown in Fig. 3.1, will be considered. They represent stars with three different X-ray luminosities: 10^{29} erg/s, 10^{30} erg/s and 10^{31} erg/s. Additionally, these spectra increase in 'hardness' as the X-ray luminosity increases, meaning that the fraction of the integrated soft (0.1 - 1 keV) X-ray spectrum to the integrated hard (> 1 keV) X-ray spectrum decreases.
As mentioned in Sec. 2.2, the mass loss is dominated by the soft part of the X-ray spectrum, which is why it is sufficient to only consider the soft X-ray luminosity in Eq. 3.1.8. For that, the coefficients A_L to D_L have been calculated and are independent of the spectrum used. According to table 4 in Ercolano et al. (2021), the soft X-ray spectrum makes up for 52% of the total X-ray luminosity in the 10^{29} erg/s spectrum and the percentage decreases to 47% for the 10^{30} erg/s spectrum and to 42% for the

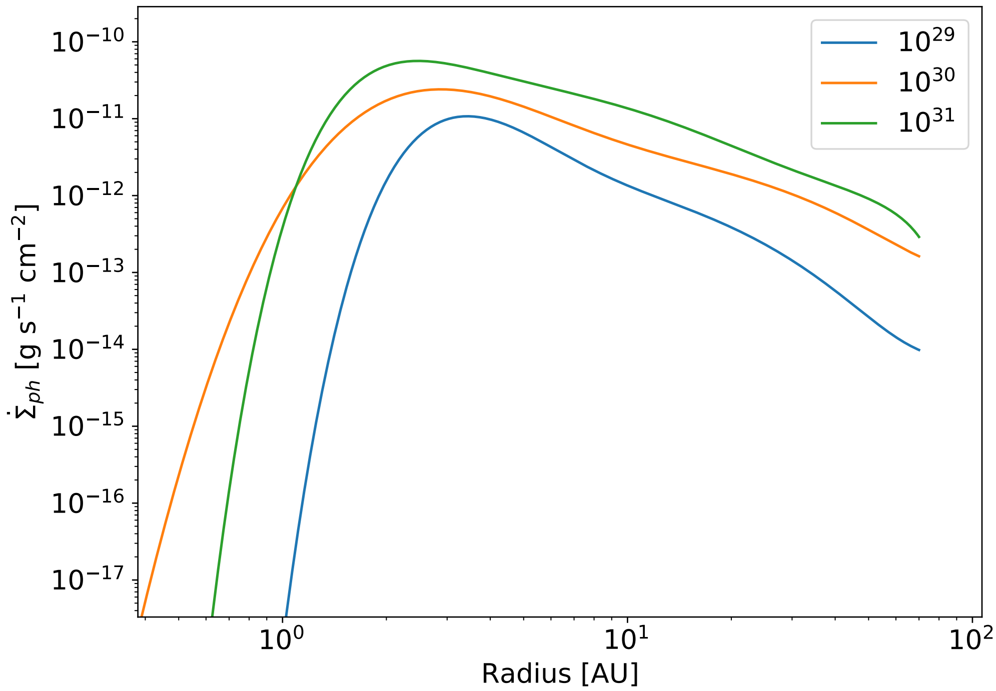

Figure 3.2: Photoevaporative mass loss profiles as calculated with Eq. 3.1.6 using the numerical coefficients from Tab. 3.1 for three different stellar X-ray luminosities (in erg/s) and corresponding X-ray spectra.

10^{31} erg/s spectrum. The numerical values for all coefficients for each of the three spectra have been adopted from Ercolano et al. (2021)[1] and are given in Tab. 3.1. Fig. 3.2 shows the resulting mass loss profiles using stellar X-ray luminosities of 10^{29} erg/s, 10^{30} erg/s and 10^{31} erg/s.

3.2 TAPIR - physical setup

The physical and numerical setup of the TAPIR Code for all simulations conducted for this thesis is described in detail by Steiner et al. (2021)and Ragossnig et al. (2020). Following their descriptions, the most important aspects are summarized in this and the following section.

[1]In Tab. 3 of Ercolano et al. (2021), the values for the coefficients are shown. However, there seem to be two literal errors made while creating this table since the mass loss profiles created with these values do not coincide with the ones shown in Fig. 4 of Ercolano et al. (2021). In Tab. 3.1, these errors have already been eliminated. The coefficient e for the 10^{29} erg/s spectrum has been changed from 67.9150 to -67.9150 and the coefficient f for the 10^{31} erg/s spectrum has been changed from 8.8216 to 18.8216. With these changes applied, the mass loss profiles are now accurately represented, as can be seen when comparing Fig. 3.2 to Fig. 4 of Ercolano et al. (2021).

3.2.1 Initial model

For the simulations, it is desirable to first create a stationary initial model from which the time evolution is then commenced. Additionally, using an implicit integration scheme, the initial model already has to be a solution for the set of hydrodynamic equations. The process of how to reach such a configuration starts with a Keplerian disk in local thermal equilibrium with no radial mass flux through the disk. The column density profile for this model is determined by,

$$\Sigma(r) = \Sigma_{\rm out}\left(\frac{r}{r_{\rm out}}\right)^{\zeta} \quad , \tag{3.2.1}$$

where $\Sigma_{\rm out}$ is the initial density at the outermost radius $r_{\rm out}$ of the simulation domain and ζ determines the column density increase towards the star. $\Sigma_{\rm out}$, $r_{\rm out}$ and ζ are set to 20 g cm^{-2}, 70 AU and -0.5, respectively.
The initial thermal equilibrium gas temperature profile is given by the temperature which the stellar radiation field imposes at a certain radius. Assuming blackbody radiation and an additional ISM ambient radiation field, the gas temperature profile reads,

$$T_{\rm gas}(r) = \left(\frac{L_\star}{\sigma_{SB}4\pi r^2} + T_{amb}^4\right)^{\frac{1}{4}} \quad , \tag{3.2.2}$$

where $L_\star$ is the stellar luminosity, σ_{SB} is the Stefan-Boltzmann-constant and T_{amb} is the temperature of the ambient radiation field and is set to 20 K, which corresponds to the average dust temperature in spiral galaxies (Bendo et al. 2003). With that, the initial specific internal energy profile can also be established by assuming perfect gas,

$$e(r) = \frac{T_{\rm gas}(r)R_{\rm g}}{\mu(\gamma-1)} \quad , \tag{3.2.3}$$

where $R_{\rm g}$ is the ideal gas constant, μ is the mean molecular weight and γ is the adiabatic index. In addition to these profiles, the azimuthal velocity u_φ is also calculated, already taking into account the radial gradient of the vertically integrated gas pressure, which results in a deviation from the keplerian velocity.
Furthermore, the position of the inner boundary of the disk is calculated using the description by Hartmann et al. (2016) which depends on the stellar mass $M_\star$ and radius $R_\star$, the magnetic field at the surface of the star $B_\star$ and the mass accretion rate onto the star $\dot{M}_\star$ (see Sec. 3.2.5). Since the radial mass flux is set to 0 in the starting configuration (as described above), $\dot{M}_\star$ has to be set artificially. For all simulations, a 0.7 $M_\odot$ star with a radius of 1.5 $R_\odot$ is used as a central object in order to match the stellar parameters with which the photoevaporative mass loss profiles were calculated by Ercolano et al. (2021). The stellar magnetic field is described as a dipole field with an

azimuthal component resulting from the drag of the magnetic field lines by the ionized disk material (see Sec. 3.2.3).
This starting configuration is utilized as a 'first guess' of the structure of the protoplanetary disk from where the time integration of the full set of equations starts.
The next step during time integration for finding a physically realistic stationary initial model for the simulations, is the opening of the inner and outer boundaries of the disk and introducing a radial velocity field. For that, a constant flow of mass $\dot{M}_{\rm out}$ from an infinite outer mass reservoir is created, which enters the disk through the outer boundary. Then, the time integration continues until a stationary state is reached, which corresponds to a time independent constant mass flow throughout the whole disk (with the value of $\dot{M}_{\rm out}$) being established. This stationary configuration is then used as an initial model for the long-term evolution simulation in which the mass flux from the outer mass reservoir is stopped ($\dot{M}_{\rm out} = 0$). Consequently, the radial profiles of the physical quantities in the actual initial model for the simulations result from a solution of the full set of hydrodynamic equations and do not follow Eqs. 3.2.1, 3.2.2 and 3.2.3. Photoevaporation is only enabled after the establishment of the initial stationary model. This is achieved by setting the photoevaporation terms in the corresponding equations to 0 prior to the time evolution simulation.
The full structure of the initial model using the described procedure is ultimately determined by the stellar parameters, $\dot{M}_{\rm out}$, the boundary conditions and the viscosity model. In order to make the simulation runs conducted in this thesis comparable, the initial models are created in such a way that the simulations start with disks which all have the same mass. During the parameter study presented in Sec. 4, several stellar- and disk parameters are varied, which would lead to different initial disk masses during the creation of the initial model. In order to achieve the same disk masses, $\dot{M}_{\rm out}$ (and therefore the initial accretion rate $\dot{M}_{\rm init}$) is adapted individually for each simulation run.

3.2.2 Viscosity description

For all calculations, the Shakura-Sunyaev α description of the kinematic viscosity ν is used (Shakura & Sunyaev 1973),

$$\nu(r) = \alpha(r) c_{\rm s}(r) H_{\rm p}(r) \quad , \tag{3.2.4}$$

where $c_{\rm s}$ is the sound speed and the parameter α is compiled of the individual values of the different disk layers, using the layered viscosity model of Gammie et al. (1996),

$$\alpha(r) = \alpha_{\rm base} + v(\Sigma(r))(\alpha_{\rm surf}(r) + \alpha_{\rm deep}(r)) + \alpha_{\rm grav} \quad . \tag{3.2.5}$$

The vertically integrated, total viscosity is then given by,

$$\mu_Q(r) = \nu(r)\Sigma(r) \quad . \tag{3.2.6}$$

In the layered viscosity description, $\alpha_{\rm base}$ is the base value of the viscosity parameter, which represents the viscosity in dead zones (i.e. MRI inactive zones). The presence of this viscosity in a dead zone is motivated by investigations studying the interactions between the MRI inactive zones and the MRI active layers above (e.g. Bai & Stone 2011; Gressel et al. 2012). $\alpha_{\rm surf}$ is the value for the permanently MRI active regions and is controlled by the parameters $\alpha_{\rm MRI}$ and Σ_0, which describe a constant value for MRI active regions and whether or not a deep layer (i.e. a dead zone) develops at a certain radius, respectively. $\alpha_{\rm surf}$ takes the form,

$$\alpha_{\rm surf}(r) = \begin{cases} \alpha_{\rm MRI}\dfrac{\Sigma_0}{\Sigma(r)}, & \text{if } \Sigma(r) > \Sigma_0 \\ \alpha_{\rm MRI}, & \text{otherwise} \end{cases} , \tag{3.2.7}$$

where for Σ_0 the value of 100 g cm^{-2} (Zhu et al. 2010a) is chosen for all calculations. Deep layers describe regions in the disk which cannot be ionized enough by cosmic rays or stellar irradiation in order to sustain a viscosity generated by MRI. But it is still possible for these layers to become MRI active if the local gas temperature $T_{\rm gas}$ exceeds a certain threshold denoted by $T_{\rm active}$. A deep layer is present at a certain radius if $\Sigma(r) > \Sigma_0$ and therefore its viscosity parameter is described by,

$$\alpha_{\rm deep}(r) = \begin{cases} \alpha_{\rm MRI}(1 - \dfrac{\Sigma_0}{\Sigma(r)})s(T_{\rm gas}(r)), & \text{if } \Sigma(r) > \Sigma_0 \\ 0, & \text{otherwise} \end{cases} , \tag{3.2.8}$$

where $s(T_{\rm gas}(r))$ is a factor describing whether the temperature exceeds $T_{\rm active}$ and the deep layer becomes MRI active or not. It creates a smooth transition between MRI active and inactive states of the deep layers by the use of the hyperbolic tangent function and a smoothing temperature range $T_{\rm width}$,

$$s(T_{\rm gas}(r)) = \frac{1}{2}\left[1 + \tanh\left(\frac{T_{\rm gas}(r) - T_{\rm active}}{T_{\rm width}}\right)\right] \quad . \tag{3.2.9}$$

$T_{\rm width}$ is set to 50 K for all calculations.
The dimensionless factor $v(\Sigma(r))$ is included to ensure that if the density drops below a minimum value $\Sigma_{\rm min}$, the viscosity is reduced to its minimum value of $\alpha_{\rm base}$ in order to hinder the density from continuing to drop to even smaller values and eventually to 0 at the same rate. This is necessary due to the numerical peculiarities of the implicit integration method and can be motivated by the fact that at such small densities, the viscosity cannot operate at its full capacity.

Configuration	$\alpha(r)$	Condition
1	$\alpha_{\rm base} + \alpha_{\rm MRI}\frac{\Sigma_0}{\Sigma(r)}$	$(\Sigma(r) > \Sigma_0) \wedge (T_{\rm gas}(r) < T_{\rm active} - 2T_{\rm width})$
2	$\alpha_{\rm base} + \alpha_{\rm MRI}$	$(\Sigma(r) < \Sigma_0) \vee (T_{\rm gas}(r) > T_{\rm active})$
3	$\alpha_{\rm base}$	$\Sigma(r) < \Sigma_{\rm min}$

Table 3.2: Possible configurations of α at radius r.

$\alpha_{\rm grav}$ is the parameter for the viscosity resulting from gravitational instability. The disk becomes gravitationally unstable when its Toomre parameter (Toomre 1964) becomes smaller than a certain critical value, typically set to unity. In the calculations for this thesis, the disk mass to stellar mass ratio has been set to low enough values of $\sim 10^{-2}$ in order to avoid the fulfillment of this criterion (e.g. Kratter & Lodato 2016). Therefore, $\alpha_{\rm grav}$ is 0 for all calculations.

In general, there are three possible configurations of the composition of α at a certain radius in the disk depending on the density and the gas temperature for all simulations conducted in this thesis. The three options are shown in Tab. 3.2. Configuration 1 describes the viscosity if the local density exceeds Σ_0 (and therefore deep layers and a dead zone are created) and the local temperature is well below the MRI activation temperature. If the temperature rises above $T_{\rm active}$, the viscosity is described by configuration 2. A smooth transition between these two configurations in the temperature range from $T_{\rm active} - 2T_{\rm width}$ to $T_{\rm active}$ is reached via the hyperbolic tangent function in the factor $s(T_{\rm gas}(r))$ (Eq. 3.2.9). Configuration 2 is also in place if the local density is smaller than Σ_0 and no deep layers are present. Configuration 3 describes the viscosity if the density drops below $\Sigma_{\rm min}$. A small linear smoothing range is included in $v(\Sigma(r))$ above $\Sigma_{\rm min}$, within which $\alpha_{\rm MRI}$ in configuration 2 is smoothly decreased to 0 as the density drops towards $\Sigma_{\rm min}$. Since $\Sigma_{\rm min}$ is set to 0.05 g cm^{-2} for all simulations, areas in which configuration 3 applies can be considered as completely empty, but the local density cannot be dropped to 0 for numerical reasons (see Sec. 5).

3.2.3 Stellar B-field

The protostellar magnetic field is described as a simple dipole aligned with the stellar rotation axis (e.g. Livio & Pringle 1992). Therefore, the magnetic field lines thread the disk vertically and the field strength in vertical direction at a radius r in the disk is described as,

$$B_{\rm z}(r) = B_\star \left(\frac{r}{R_\star}\right)^{-3} \tag{3.2.10}$$

where $B_\star$ is the magnetic field strength at the stellar surface, with values ranging from a few hundred G to several kG (e.g. Johns-Krull 2007) and $R_\star$ is the stellar radius.

The influence of the stellar magnetic field on the dynamics of the disk is expressed as the magnetic pressure term ($H_\mathrm{p}\nabla\left(\frac{B_\mathrm{z}^2}{4\pi}\right)$) and the term describing the torque exerted onto the ionized disk material ($\frac{B_\mathrm{z}\mathbf{B}}{2\pi}$) in Eq. 3.1.3. This torque can effectively decrease the angular velocity of the disk in the innermost parts of the disk, where the azimuthal velocity of the disk material exceeds the stellar rotation velocity. The radius at which the values of these two velocities match is described as the corotation radius r_cor. When assuming Keplerian angular velocities in the disk, the corotation radius is described as,

$$r_\mathrm{cor} = \left(\frac{P^2 G M_\star}{4\pi^2}\right)^{\frac{1}{3}} \quad , \tag{3.2.11}$$

where P is the stellar rotation period. In the simulations conducted in this thesis, the azimuthal velocities in the disk are not necessarily Keplerian due to i.a. the inclusion of the gas pressure term in the equation of motion (Eq. 3.1.3). This means that the corotation radius may not lie exactly at the location described by Eq. 3.2.11, but since this difference is very small, the definition of r_cor via Eq. 3.2.11 is sufficient for the simulations described in this thesis.

Stellar spinup or spindown as a result of angular momentum transfer onto the star is not considered in this thesis since the interest lies in the influence of photoevaporation on the disk rather than on the evolution of the star. The stellar rotation period is therefore held constant at 5.5 days, leading to a corotation radius (with a 0.7 $M_\odot$ central star) of 0.054 AU. The decrease of the disk's angular velocity within this distance can lead to an amplified accretion flow onto the star. On the other hand, outside this radius, the disk material can be accelerated in azimuthal direction. At the same time, the disk material causes the stellar magnetic field to drag behind, which introduces an azimuthal magnetic field component at the disk surface (e.g. Kluzniak & Rappaport 2007). Neglecting effects such as magnetic reconnection, accretion funnels or buoyant magnetic loops, the simplified description of the azimuthal component reads,

$$B_\varphi(r) = -\alpha_\mathrm{cor} B_\mathrm{z}(r)\left(1 - \left(\frac{\Omega(r)}{\Omega_\star}\right)^{-\alpha_\mathrm{cor}}\right) \quad , \tag{3.2.12}$$

where $\Omega(r)$ and $\Omega_\star$ are the angular velocity of the disk at radius r and the stellar angular velocity respectively. α_cor has the value -1 if $r > r_\mathrm{cor}$ and 1 if $r < r_\mathrm{cor}$. The development of an such an azimuthal magnetic field component is ultimately responsible for the exertion of magnetic torque on the inner disk (torque terms in Eq. 3.1.3 and Eq. 3.3.4).

3.2.4 Stellar X-ray luminosity

Classical T Tauri stars are observed to show X-ray luminosities ranging from 10^{29} erg/s to 10^{31} erg/s (e.g. Güdel et al. 2007). Hence, the stellar X-ray spectra used for the description of X-ray induced photoevaporation used by Ercolano et al. (2021) are constrained to this luminosity range. As a connection to the total bolometric luminosity of the star, the relation found by Telleschi et al. (2007) for classical T Tauri stars in the Taurus molecular cloud is used to find the total stellar luminosity corresponding to the used X-ray luminosity as an input parameter for the simulations. The relation reads,

$$L_\mathrm{X} = 10^{-3.73} L_\star \Rightarrow L_\star = 10^{3.73} L_\mathrm{X} \quad , \tag{3.2.13}$$

where $L_\star$ is the bolometric luminosity of the central star.
Several studies have indicated that accretion onto the star suppresses its X-ray activity (Preibisch et al. 2005; Telleschi et al. 2007; Bustamante et al. 2016), where it was found that strongly accreting stars show a deficiency in X-ray luminosity compared to weak accretors. On the other hand, some observations show that during episodic strong accretion events, the X-ray output of the system increases (Kastner et al. 2002, 2004). But the X-ray excess during strong accretion could possibly never reach the surrounding disk due to screening by dense accretion flows. For constant accretion over time, this screening has been taken into account by Ercolano et al. (2021) when constructing the photoevaporative mass loss profiles. Therefore, in this thesis, the X-ray luminosity is chosen to be a constant function of the stellar luminosity, independent of the additional luminosity generated by accretion L_acc for most simulations. In these cases, the stellar luminosity was chosen according to the X-ray luminosity used to describe the photoevaporative mass loss (Eq. 3.1.6) following Eq. 3.2.13. However, specific simulation runs were also conducted with L_X being dependent on L_acc in the following way,

$$L_\mathrm{X} = 10^{-3.73} (L_\star + L_\mathrm{acc}) \quad , \tag{3.2.14}$$

in order to investigate the influence of increased photoevaporation due to accretion. The accretion luminosity results from the release of energy during the accretion process, where it is assumed that 70% of the gravitational energy is converted into radiation,

$$L_\mathrm{acc} = \frac{7}{10} \frac{G M_\star \dot{M}_\star}{R_\star} \quad . \tag{3.2.15}$$

In these runs, the stellar luminosity $L_\star$ was again chosen to result in the desired X-ray luminosity according to Eq. 3.2.13, but during the simulation, L_X was adapted at every timestep to the accretion rate following Eq. 3.2.14. The largest difference between these two descriptions becomes evident in the presence of episodic accretion events.

3.2.5 Boundary conditions

The definition of inner and outer boundary conditions is crucial in determining the structure of the simulated protoplanetary disk. As argued by Ragossnig et al. (2020), the position and the conditions at the boundaries of the computational domain can have a large impact on the long-term evolution of a disk-like structure, since they ultimately determine the solutions of the set of partial differential equations which are then used to find the new solutions at the next timestep.

Concerning protoplanetary disks, finding the location of the inner and outer boundary is not trivial. As already indicated in Sec. 3.2.1 in the context of the initial model, for the simulations in this thesis, the inner boundary is located at the magnetic truncation radius within which the magnetic pressure of the stellar dipole magnetic field is strong enough to disrupt the disk and force the disk material to be accreted onto the star along trajectories determined by the magnetic field. This truncation radius can be determined in two separate ways depending on the gas pressure $P_{\rm gas}$ in the innermost parts of the disk and the ram pressure of the accreted disk mass $P_{\rm ram}$. When the accretion rate onto the star is small, $P_{\rm gas}$ can become larger than $P_{\rm ram}$. In this case, the inner boundary is set at the radius where the magnetic pressure is equal to $P_{\rm gas}$. Otherwise, in case of strong accretion, $P_{\rm ram}$ exceeds $P_{\rm gas}$ and the truncation radius is set at the distance where the magnetic pressure becomes comparable to $P_{\rm ram}$. For more details, see Steiner et al. (2021). In both cases, the inner boundary is not fixed throughout the simulation. When $P_{\rm gas} > P_{\rm ram}$, the truncation radius depends directly on the local gas pressure. In the other case, the inner boundary can move according to the time dependent accretion rate onto the star, which influences $P_{\rm ram}$. During episodic accretion events, the increased accretion rate results in an inward movement of the inner boundary because the large ram pressure can still withstand the magnetic pressure much closer to the star. With the numerical model used in this thesis, it is even possible to push the inner boundary as far as to reach the stellar surface while still being able to simulate the long-term evolution of the entire disk. On the other hand, if the accretion rate onto the star decreases, the truncation radius and therefore the inner boundary move outwards.

If the radius of the inner rim of the disk becomes larger than the corotation radius, the star-disk connection enters the 'propeller-regime'. The propeller effect (Illarionov & Sunyaev 1975) describes a phenomenon in which accreting disk material is ejected again by the stellar magnetosphere. As mentioned in Sec. 3.2.3, disk material is azimuthally accelerated shortly outside $r_{\rm cor}$ due to the magnetic torque resulting from a higher rotation velocity of the magnetosphere in comparison to the angular velocity of the disk. When the magnetic truncation radius lies in the accelerated area, the centrifugal force exceeds the gravitational pull at the inner boundary. This leads to a radially outward acceleration of disk material at this location and the accretion onto the central star effectively stops as the majority of matter is expelled radially away from the magnetosphere (e.g. Romanova et al. 2003). In the context of protoplanetary disks, the propeller effect can occur at a certain stage during an episodic accretion event (Campana et al. 2018) or at late stages of the disk evolution where the accretion rate drops to levels low enough to push the inner boundary of the disk beyond the corota-

tion radius. The latter is an important phenomenon in the simulations conducted in this thesis, since being able to self-consistently model the star-disk interaction in the inner disk and the long-term evolution of the disk simultaneously can show the impact of the propeller effect and its interplay with the photoevaporative mass loss in the late-stage evolution of the disk.
As explained in Steiner et al. (2021), during the simulations, Neumann conditions are set for the main variables of the hydrodynamic equations at the inner boundary,

$$\left.\frac{\partial \Sigma}{\partial r}\right|_{r=r_{\mathrm{in}}} = \left.\frac{\partial u_{\mathrm{r}}}{\partial r}\right|_{r=r_{\mathrm{in}}} = \left.\frac{\partial u_{\varphi}}{\partial r}\right|_{r=r_{\mathrm{in}}} = \left.\frac{\partial T_{\mathrm{gas}}}{\partial r}\right|_{r=r_{\mathrm{in}}} = 0 \quad . \tag{3.2.16}$$

In addition to that, when the simulation enters the propeller-regime, the radial velocity is set to 0 at the inner boundary in order to prevent an unphysical flow of matter from the star into the disk through the inner boundary. An artificial smoothing of u_{r} towards 0 is not necessary, because as the inner boundary moves towards the corotation radius, the accretion rate and the radial velocity smoothly decrease and reach 0 approximately when $r_{\mathrm{in}} = r_{\mathrm{cor}}$. The position of the outer boundary for protoplanetary disks is also not unambiguous since there is no geometric argument that establishes a clear border between the disk and the surrounding interstellar medium. In order to make the disks and the influence of photoevaporative mass loss comparable for the different parameter setups of the simulations in this thesis, the outer boundary of the computational domain is set at a radius of 70 AU. Since the initial disk mass is chosen to be small ($M_{\mathrm{disk,init}} \simeq 0.01 M_\star = 0.007 M_\odot$ for all simulations), the column density outside of 70 AU is very small and would reach Σ_{min} almost immediately in the simulations.
Similarly to the inner boundary, Neumann conditions are chosen for the column density and the temperature at the position of the outer boundary r_{out},

$$\left.\frac{\partial \Sigma}{\partial r}\right|_{r=r_{\mathrm{out}}} = \left.\frac{\partial T_{\mathrm{gas}}}{\partial r}\right|_{r=r_{\mathrm{out}}} = 0 \quad , \tag{3.2.17}$$

while the value of u_φ is set to the keplerian velocity,

$$u_\varphi(r_{\mathrm{out}}) = \sqrt{\frac{GM_\star}{r_{\mathrm{out}}}} \quad . \tag{3.2.18}$$

The radial velocity at the outer boundary is adapted with respect to the mass flux from the outer infinite mass reservoir $\dot{M}_{\mathrm{out}}$,

$$u_{\mathrm{r}}(r_{\mathrm{out}}) = \frac{\dot{M}_{\mathrm{out}}}{2\pi r_{\mathrm{out}} \Sigma(r_{\mathrm{out}})} \quad . \tag{3.2.19}$$

As noted in Sec. 3.2.1, $\dot{M}_{\mathrm{out}} = 0$ after the establishment of the initial configuration, leading to $u_{\mathrm{r}}(r_{\mathrm{out}}) = 0$ during the simulation. One could argue that at some point during the simulations, $u_\mathrm{r}(r_\mathrm{out})$ can become greater than 0 due to the viscous angular momentum outward transport, which accelerates the outermost annulus of the disk in azimuthal direction. Since the angular momentum cannot be transferred outwards any further, the material in the outermost annulus experiences an acceleration in radial direction outwards as well. But our initial model already includes a mass flux (and therefore a radial velocity) towards the star in the outer cells of the numerical grid. This means that the angular momentum transported to the outermost annulus only decreases the radial velocity inward, but is never able to turn the direction of the mass flux outward. Therefore, $u_\mathrm{r}(r_\mathrm{out})$ does not have to adapt itself to a flow from any direction during the simulation.

3.3 TAPIR - numerical setup

The time evolution of the protoplanetary disk is simulated by adapting Eqs. 3.1.2, 3.1.3 and 3.1.4 to a 1D cylindrical symmetric geometry, discretizing them onto a numerical grid and integrating them using an implicit integration scheme implemented into the TAPIR Code (for details, see Ragossnig et al. 2020).

3.3.1 Adaptive grid

The numerical grid consists of 2000 initially logarithmically spaced grid points at which the values of the physical quantities are defined. The innermost and outermost points are set at the locations of the boundary conditions described in Sec. 3.2.5. A differentiation is made between scalar- and vector-quantities, which are defined on two separate grids that are shifted against each other. This *staggered mesh* is constructed in a way that the points at which vector-quantities are defined (on the vector-grid) are located in the center between two points of the scalar-grid. The spaces between grid points are referred to as grid cells and have volumes denoted as V_S and V_V for the scalar- and vector-grid respectively. A staggered mesh can also be seen as a single grid, where vector quantities are defined at the cell boundaries and scalar quantities at the center of the cell. This facilitates the determination of fluxes from one cell to the next one, since the velocity of the flow (a vector quantity) is already given at the boarder between the two cells.
Since the cells do not have an expansion in vertical direction due to the 1D approach, they can be identified as *integration areas* with the unit cm^2. In these cells, the physical quantities are kept constant. Two additional cells with physical volumes of 0 cm^2 are added each at the outer and at the inner border of the computational domain. This means that the innermost three and the outermost three numerical grid points are located at the same radius in the physical domain. The physical quantities in these four *ghost cells* do not directly result from the solution of the set of equations, but are deter-

mined according to the boundary conditions described in section 3.2.5. The structure of the numerical grid projected into the physical domain including the ghost cells is depicted in figure 3.3.

The location of the grid points in the physical domain is not fixed throughout the simulations, but follows a *grid equation*, which is solved simultaneously with the hydrodynamic equations. All details about the adaption of the grid via the grid equation are presented in Dorfi & Drury (1987). The idea of an adaptive grid is to increase the resolution of the simulation process at locations where steep gradients in the radial functions of relevant physical quantities are present. This is done by rearranging the present grid points according to the self-consistent solution of the grid equation, rather than adding new grid points while keeping the others at the same location. The latter version is part of adaptive mesh refinement methods and can result in disturbances in the numerical system (e.g. Berger & Oliger 1984). These disturbances can be avoided while still increasing the resolution at the respective locations in the grid by calculating new positions for the grid points at every timestep according to the grid equation. For that, a desired grid point distribution has to be defined according to the gradients present in the physical domain. For the simulations in this thesis, it is sufficient to choose the column density and the azimuthal velocity as the relevant variables that define the desired resolution. Consequently, the grid point distribution is calculated at each timestep in a way that it spatially and temporally smoothly transitions towards the desired resolution according to the gradients in the radial column density and angular velocity functions. The timescale on which the grid adapts itself (denoted by τ) is set to be proportional to the dynamic timescale τ_{dyn},

$$\tau(r) = w \cdot \tau_{\mathrm{dyn}}(r) = w \cdot \sqrt{\frac{r^3}{GM_\star}} \quad , \tag{3.3.1}$$

where the proportionality factor w is set to 10^6 for all simulations.

3.3.2 Discretized equations

In order to solve the set of hydrodynamic equations numerically on the grid of the 1D setup of the TAPIR Code, the system of equations to solve has to be discretized. While doing so, the adaptive grid and the resulting velocity of the grid point movement has to be taken into account. Therefore, a generalization of the Reynolds-Transport theorem has to be used which is denoted as the adaptive grid transport theorem (Winkler et al. 1984). The application of this theorem to the system of hydrodynamic equations has been discussed in detail by Dorfi et al. (2006) and Ragossnig et al. (2020). Using the definition of scalar- and vector-volumes as determined by the staggered mesh grid in the previous section, the 1D discretized system of hydrodynamic equations used for the simulations in this thesis will briefly be presented here. In the following equa-

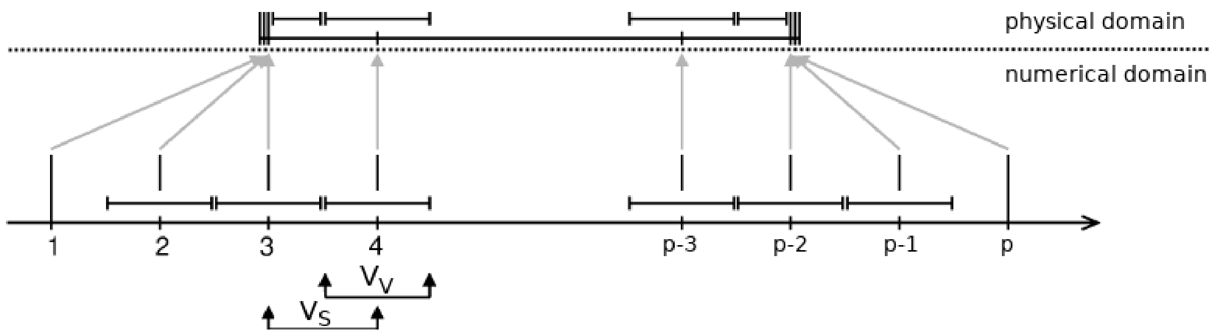

Figure 3.3: General discretization scheme and projection into the physical domain. The four ghost cells do not have a physical volume and serve the purpose of implementing the boundary conditions without disturbing the structure of the implicit numerical solver (see Sec. 3.3.3). The total number of grid points is denoted with p. (This image was adapted from Ragossnig et al. 2020).

tions, symbols denoted as $\tilde{x}$ represent quantities that are to be advected over the cell boundaries. The summation of these quantities over the inner and outer cell boundary is marked with $\sum \tilde{x}\Delta\mathrm{Vol}_{(\mathrm{S,V})}$. The symbols δ and Δ signal the temporal ($t \rightarrow t + \delta t$) and spatial ($r_\mathrm{i} \rightarrow r_{\mathrm{i+1}}$) difference, respectively, of the following term. $\bar{x}$ denotes scalar quantities averaged between two adjacent grid cells in order to be projected onto the corresponding grid point on the vector grid. The terms representing the influence of photoevaporation are written in bold. All variables in the following equations are understood to be functions of only radius r and time t.

Equation of continuity:

$$\delta[\Sigma V_\mathrm{S}] + \sum \widetilde{\Sigma}\Delta\mathrm{Vol}_\mathrm{S} + \dot{\boldsymbol{\Sigma}}_{\mathbf{ph}}\boldsymbol{V}_{\mathbf{S}}\boldsymbol{v}\boldsymbol{\delta t} = 0 \quad , \tag{3.3.2}$$

The terms in the above equation represent (in order) the temporal difference of density in a grid cell between the current time t and the new time $t + \delta t$, the advection over the cell boundaries and the influence of photoevaporation. The process of discretizing the equations involves integration over a finite volume (V_S in this case). In the final discrete form, this is visible as a product of the physical quantity with the finite volume.

The photoevaporation term consists of 4 constituents. $\dot{\boldsymbol{\Sigma}}_{\mathbf{ph}}$ is the photoevaporative mass loss profile shown in Eq. 3.1.6. In the discrete form, the amount of lost mass per second and cm^2 at the grid point r_i can be calculated by evaluating Eq. 3.1.6 with the corresponding coefficients from Tab. 3.1 at r_i. This value has then to be multiplied with the volume of the corresponding grid cell (V_S in cm^2) to receive a number for the total mass lost in this grid cell per second. The total mass loss of the cell during a timestep is then given by multiplication with the timestep δt. Of course, this assumes the photoevaporation rate to be constant over the cell volume, but this is the nature of discretizing a continuous function onto a numerical grid using a finite-volume method (see Sec. 3.3.1). The factor v is the same as described in the context of viscosity in Sec. 3.2.2. Here, it ensures that if the column density drops below $\Sigma_{\min}$, the mass loss through the photoevaporative wind ceases in order to avoid numerical problems when Σ becomes even smaller. As explained in Sec. 3.2.2, v includes a small linear smoothing range above $\Sigma_{\min}$ within which the photoevaporative mass loss is smoothly decreased until it reaches 0 as the density drops to $\Sigma_{\min}$.

Radial equation of motion:

$$\delta[\bar{\Sigma} u_{\mathrm{r}} V_{\mathrm{V}}] + \sum \widetilde{(\bar{\Sigma} u_{\mathrm{r}})} \Delta \mathrm{Vol}_{\mathrm{V}} - \frac{\bar{\Sigma} u_{\varphi}^2}{r} V_{\mathrm{V}} \delta t + 2\pi r \sqrt{2\pi} \Delta \left[H_{\mathrm{p}} \left(P_{\mathrm{gas}} + \frac{B_{\mathrm{z}}^2}{8\pi} \right) \right] \delta t - \partial_r \Psi(r)_{tot} \Sigma \Delta \mathrm{Vol}_{\mathrm{V}} - \frac{\pi}{r} \Delta \left\{ \bar{r}^2 \mu \left[\frac{\Delta u_{\mathrm{r}}}{\Delta \bar{r}} - \frac{\bar{u}_r}{r} \right] \right\} \delta t + \boldsymbol{\dot{\Sigma}_{\mathrm{ph}} u_{\mathrm{r}} v V_{\mathrm{V}} \delta t} = 0 \quad , \quad (3.3.3)$$

The radial part of the equation of motion (Eq. 3.1.3) in discrete form consists of the following terms (in order): temporal difference (analogous to the temporal term in the equation of continuity), advection of radial momentum over the vector cell boundaries, centrifugal force, gas- and magnetic pressure force, gravitational force, viscous friction force, removal of radial momentum by photoevaporation of mass. In the photoevaporation term, the mass loss rate $\boldsymbol{\dot{\Sigma}_{\mathrm{ph}}}$ in the grid cell has to be multiplied with the radial velocity at the same location in order to get the value for the removed radial momentum per second and cm^2 (due to radial momentum being defined in general as $p = mu$, with m being the mass and u the velocity). Multiplication with the cell volume (since u_{r} is a vector quantity, it is defined on the vector grid and the corresponding cell volume is V_{V}) and the timestep results in the total radial radial momentum removed by evaporation from the grid cell during the timestep.

Azimuthal equation of motion:

$$\delta[\bar{r} \Sigma u_{\varphi} V_{\mathrm{S}}] + \sum \bar{r} \widetilde{(\Sigma u_{\varphi})} \Delta \mathrm{Vol}_{\mathrm{S}} - \pi \Delta \left\{ r^2 \mu \left[\frac{\Delta u_{\varphi}}{\Delta \bar{r}} - \frac{\bar{u}_{\varphi}}{r} \right] \right\} \delta t - \bar{r} \frac{B_{\mathrm{z}} B_{\varphi}}{4\pi} V_{\mathrm{S}} \delta t + \boldsymbol{\bar{r} \dot{\Sigma}_{\mathrm{ph}} u_{\varphi} v V_{\mathrm{S}} \delta t} = 0 \quad , \quad (3.3.4)$$

The azimuthal equation of motion is composed of the following terms (in order): temporal difference, advection of angular momentum over the scalar cell boundaries, viscosity, magnetic torque, photoevaporation. u_{φ} has to be discretized on the scalar grid, even though it is a vector quantity. This is because using a 1D approach, u_{φ} is projected onto a purely radial grid. Due to u_{φ} being defined at the cell boundaries of the vector grid (i.e. in the center of the scalar grid cell), it has to be multiplied with the radius at the center of the scalar grid cell $\bar{r}$ in order to evaluate the angular momentum on the scalar grid. The multiplication of $\boldsymbol{\dot{\Sigma}_{\mathrm{ph}}}$ with the scalar volume, the azimuthal velocity, the radius, the timestep and the factor v follows the same argumentation as for the radial equation of motion.

Equation of energy:

$$\delta[\Sigma e V_{\mathrm{S}}] + \sum \widetilde{(\Sigma e)} \Delta \mathrm{Vol}_{\mathrm{S}} + P_{gas,z} 2\pi \Delta(r u_{\mathrm{r}}) \delta t + 8\pi^2 \sqrt{2\pi} H_{\mathrm{p}} \sigma \Delta \left[- \frac{\frac{2}{3} r^2 \Delta(T^4)}{\kappa_{\mathrm{R}} \overline{\Sigma_0} V_{\mathrm{V}}} \right] \delta t + \dot{E}_{\mathrm{rad}} - \frac{\mu}{2} \left\{ \left[\frac{\Delta u_{\mathrm{r}}}{\Delta r} - \frac{\bar{u}_{\mathrm{r}}}{\bar{r}} \right]^2 + \left[\frac{\Delta u_{\varphi}}{\Delta r} - \frac{\bar{u}_{\varphi}}{\bar{r}} \right]^2 \right\} V_{\mathrm{S}} \delta t + \boldsymbol{\dot{\Sigma}_{\mathrm{ph}} e V_{\mathrm{S}} v \delta t} = 0 \quad , \tag{3.3.5}$$

The terms in the above equation denote the following (in order): temporal difference, advection of energy over the scalar cell boundaries, compression via gas pressure, radiation transport, radiative heating and cooling, viscous energy creation, photoevaporation. Multiplying the photoevaporative mass loss with the specific internal energy results in the amount of internal energy lost per second and cm^2. After multiplication with the cell volume and the timestep, the value for the total internal energy loss through photoevaporative mass removal in the whole cell over the timestep is given.

3.3.3 Implicit time integration

An implicit integration scheme with an adaptive timestep allows to simulate the physical processes in the very inner parts of the disk self-consistently while still being able to investigate the long-term evolution of the whole disk. The reason for that is that the choice of the timestep is not restricted by the *Courant-Friedrichs-Lewy* (CFL) condition (Courant et al. 1928), which would be the case if an explicit integration method is used. The CFL condition constitutes an upper limit for the timestep above which instabilities arise when using an explicit method. It states that the timestep has to be smaller than the time the simulated flux needs to flow over two grid points anywhere in the grid,

$$\delta t \leq \min_{\mathrm{i}} \frac{\Delta x_{\mathrm{i}}}{|u_{\mathrm{i}}| + c_{\mathrm{s,i}}} \quad , \tag{3.3.6}$$

where δt is the timestep, Δx_{i} is the width of the i-th grid cell, u_{i} denotes the velocity of the flux and $c_{\mathrm{s,i}}$ is the local sound speed. In the above condition, the smallest Δx_{i} has to be used to determine the maximum timestep. In the context of simulations of protoplanetary disks, the maximum timestep according to the CFL condition will always be set at the inner boundary where the velocities are the highest. This makes long-term evolution simulations with an inner boundary close to the star impossible for explicit methods. Therefore an implicit integration scheme is used for the simulations in this thesis, where the CFL condition does not apply. In the following, the general structure

of the implicit method implemented in the TAPIR-Code is explained.
In general, a discrete set of equations to solve at the time t can be written as (Dorfi et al. 2006),

$$G_{\mathrm{m,i}}(\vec{X}^{(t)}) = 0 \quad , \qquad 1 \leq m \leq M \quad , \qquad 1 \leq i \leq p \quad , \tag{3.3.7}$$

where M is the number of equations (i.e. number of variables), p is the number of grid points and $\vec{X}$ is the vector containing all variables at every grid point,

$$\vec{X} = (\vec{X}_1, \vec{X}_2, ..., \vec{X}_{\mathrm{p}}) \quad . \tag{3.3.8}$$

The system of (in this case) non-linear equations incorporates M equations at p grid points, which means that at every timestep, $M \times p$ unknowns have to be found. In order to do that, we take advantage of the fact that Eq. 3.3.7 also has to be obeyed at the time $t + \delta t$, i.e.

$$G_{\mathrm{m,i}}(\vec{X}^{(t+\delta t)}) = 0 \quad . \tag{3.3.9}$$

A Taylor-expansion of this system around the new time $t + \delta t$ gives,

$$G_{\mathrm{m,i}}(\vec{X}^{(t+\delta t)}) = G_{\mathrm{m,i}}(\vec{X}^{(t)}) + \mathbf{J}(\vec{X}_{\mathrm{i}}^{(t+\delta t)} - \vec{X}_{\mathrm{i}}^{(t)}) = 0 \quad , \tag{3.3.10}$$

where $\mathbf{J}$ is the ($Mp \times Mp$) Jacobi-matrix of this system which contains the derivatives of every equation with respect to every variable at every grid point. A solution for the new time $t + \delta t$ at the grid point i can then be found by inversion of the Jacobi-matrix and rearrangement of Eq. 3.3.10. Due to the non-linear nature of the system of equations, the solution for the new time has to be found iteratively, which is done by a multi-dimensional Newton-Raphson algorithm.
As it is evident in Eq. 3.3.10, the solution of the equations at one grid point depends on the values of the physical variables at every grid point. The inversion of such a Jacobi-matrix at every timestep would be computationally prohibitive. Therefore, a *five-point-stencil* is used, where the solution at one grid point only depends on the variables at the two previous and the two subsequent grid points. At each of the boundaries, two additional grid cells (*ghost cells*, see Sec. 3.3.1) are implemented in which the boundary conditions can be implemented. With that, the five point stencil can be applied to every grid point in the physical domain and the boundary conditions do not have to be imposed on the cells with physical volume. This method results in a penta-diagonal structure of the Jacobi-matrix, which allows for a simpler inversion and does not require a modification of the matrix inversion and equation solving method.
The simulations are governed by an adaptive timestep control scheme. The chosen timestep thereby is determined by the ability of the Newton-Raphson iterator to find solutions after a specific number of iterations. If a solution cannot be found at the new time using the timestep for the previous solution (or too many iterations are necessary),

the timestep will be reduced. This is typically the case if the physical quantities change quickly in time at certain stages of the simulations (e.g. during FU-Ori outbursts). On the other hand, if the previous timestep allows finding a new solution after very few iterations, the new timestep can be chosen to be larger. This control scheme can lead to a large range of timesteps (ranging from $\sim 10^4$ s to $\sim 10^{12}$ s) over the course of a single simulation.

3.3.4 Boundary conditions

As stated above, boundary conditions are essential for finding solutions for the system of equations at hand and can have a large impact on the outcome of the simulations. In conjunction with the five-point-stencil, the boundary conditions for all simulations in this thesis are given in the ghost cells at the inner and outer boundary of the computational domain.
The position of the inner boundary is calculated at every timestep according to the description given in Sec. 3.2.5. The innermost three grid points (two ghost cells) are then set at this position in the physical domain. Taking the column density as an example, the Neumann conditions are implemented in the following way:

$$\Sigma(r_1) = \Sigma(r_2) = \Sigma(r_3) \quad , \tag{3.3.11}$$

$$\Sigma(r_{\mathrm{p}-3}) = \Sigma(r_{\mathrm{p}-2}) = \Sigma(r_{\mathrm{p}-1}) = \Sigma(r_{\mathrm{p}}) \quad , \tag{3.3.12}$$

where r_i denotes the i-th grid point and p is the number of grid points ($\mathrm{p} = 2000$ for all simulations). r_p denotes the outer boundary of the outermost ghost cell. In this context, $\Sigma(r_3)$ and $\Sigma(r_{\mathrm{p}-3})$ represent the column density in the cells adjacent to the ghost cells on the inner and outer boundary, respectively. The physical quantities in these two cells result from the solution of the set of equations. In order to fulfill the Neumann conditions, the ghost cells have to adapt the same values. This ensures that the effects of physical processes inside the disk that affect density, velocity and temperature at the inner rim of the disk are not stopped by rigid boundaries, but can properly propagate further through open boundary conditions. The outer boundary conditions for the radial and azimuthal velocity are are set by,

$$u_\varphi(r_\mathrm{i}) = \sqrt{\frac{GM_\star}{r_\mathrm{i}}} \quad , \qquad u_\mathrm{r}(r_\mathrm{i}) = \frac{\dot{M}_\mathrm{out}}{2\pi r_\mathrm{i}\Sigma(r_\mathrm{i})} \quad , \qquad i = (p-2), (p-1), p \quad . \tag{3.3.13}$$

As soon as the system enters the propeller-regime, where the mass flux at the inner boundary would change its direction (which happens approximately when $r_\mathrm{in} = r_3 = r_\mathrm{cor}$), the radial velocity at the inner boundary has to be set artificially,

$$u_\mathrm{r}^{(t+\delta t)}(r_3) = 0 \qquad \text{if} \quad u_\mathrm{r}^{(t)}(r_3) \geq 0 \ \wedge u_\mathrm{r}^{(t)}(r_4) \geq 0 \quad . \tag{3.3.14}$$

The above condition states, that if the radial velocity at the physically innermost two grid cells rises above 0 (meaning its direction points radially outwards), it is set to 0 at the next timestep at the innermost cell. Due to the (simultaneously applied) Neumann condition for the radial velocity, u_{r} is set to 0 in the inner ghost cells as well. In case the physical process inside the disk lead to yet another turnaround of mass flux at the inner boundary, $u_{\mathrm{r}}^{(t)}(r_4)$ would drop below 0 again and the above condition is lifted, opening the inner boundary for an accretion flow onto the star.

4 Results

The goal of this thesis is to investigate the effect of photoevaporative mass loss on the long-term evolution of protoplanetary disks and to show the influence of various stellar- and disk properties. In particular, the effects of different stellar luminosities, stellar magnetic fields and disk viscosity parameters will be analyzed. For this purpose, a fiducial model has been created, to which every simulation can be compared to. Each simulation run (including the fiducial model) has been conducted with and without (suffix `nPh` in the model name) mass loss due to photoevaporation. In Tab. 4.1, the most important stellar and disk parameters which stay constant for every simulation run are summarized again. In Sec. 4.1 the fiducial model is presented and analyzed with respect to the influence of photoevaporation on the long-term evolution. Sections 4.2, 4.3 and 4.4 show the results of simulations runs where the stellar luminosity, the stellar magnetic field and the disk viscosity parameters are varied, respectively.

$M_\star$ $[M_\odot]$	0.7	$M_{\mathrm{disk,init}}$ $[M_\odot]$	0.007
$R_\star$ $[R_\odot]$	1.5	α_{grav}	0.0
$P_\star$ [d]	5.5	Σ_{min} [g cm^{-2}]	0.05
r_{cor} [AU]	0.054	Σ_0 [g cm^{-2}]	100
r_{out} [AU]	70	T_{active} [K]	1500

Table 4.1: Constant stellar and disk parameters used for every simulation.

4.1 Fiducial model

Tab. 4.2 shows the parameters chosen for the fiducial model. A differentiation is made between the total stellar X-ray luminosity L_X and the luminosity of the soft X-ray spectrum $L_\mathrm{X,soft}$. L_X is set to 10^{30} erg/s so that the corresponding mass loss profile (Sec. 3.1.1, Fig. 3.2) can be utilized. $L_\star$ is then calculated according to Eq. 3.2.13. $L_\mathrm{X,soft}$ is the value used in Eq. 3.1.8 to calculate the evaporative mass loss (see Sec. 3.1.1). $\dot{M}_\mathrm{init}$ is the initial constant mass flux throughout the whole disk (which corresponds to $\dot{M}_\mathrm{out}$ during the establishment of the initial model, see Sec. 3.2.1). The value for $\dot{M}_\mathrm{init}$ is chosen so that the disk mass of the stationary initial model results in $10^{-2}M_\star \approx 7\cdot 10^{-3}M_\odot$ to ensure gravitational stability (see Sec. 3.2.2).

Model	$L_\star$ $[L_\odot]$	L_X $[\mathrm{erg\ s^{-1}}]$	$L_\mathrm{X,soft}$ $[\mathrm{erg\ s^{-1}}]$	$B_\star$ $[\mathrm{kG}]$	α_MRI	α_base	$\dot{M}_\mathrm{init}$ $[M_\odot\ \mathrm{yr^{-1}}]$	Ph
`fid`	1.4	10^{30}	$0.47\cdot 10^{30}$	2.0	$5\cdot 10^{-3}$	$1\cdot 10^{-4}$	$1.90\cdot 10^{-9}$	x
`fid_nPh`	1.4	10^{30}	$0.47\cdot 10^{30}$	2.0	$5\cdot 10^{-3}$	$1\cdot 10^{-4}$	$1.90\cdot 10^{-9}$	

Table 4.2: Run parameters for the fiducial model. The last column (Ph) marks for which simulation runs photoevaporation is included.

Fig. 4.1 shows the overall evolution of the column density and the mass flux through the disk for the fiducial model with (`fid`, panels a and b) and without (`fid_nPh`, panels c and d) photoevaporation. The mass flux is defined so that a positive sign means a flux towards the star, whereas a negative sign signalises the direction of the flux pointing away from the star. The black dashed lines show the initial, stationary configuration (with a constant mass flux $\dot{M}_\mathrm{init}$) of the disk with the fiducial parameters. A dead zone develops for $r < 2$ AU, where mass piles up due to the reduced viscosity (see Sec. 3.2.2. The viscosity in the dead zone is described by configuration 1 in Tab. 3.2.). The density profile drops down towards the inner rim of the disk due to the chosen boundary condition that allows for an unhindered accretion of disk material onto the central star. The fully MRI active zone starts at $r \simeq 2$ AU, where the density profile shows an approximately exponential decay towards the outer boundary at 70 AU.

4.1.1 Evolution without photoevaporation

Starting with the `fid_nPh` model, the surface density evolves according to the viscous angular momentum transport through the disk. Fig. 4.1 shows that the size of the dead zone slowly decreases as the material on the inner rim of the disk accretes onto the star and the matter from the outer disk continuously flows inwards, leading to a decline of the surface density in the outer (fully MRI active) disk. In panel d, the evolution of

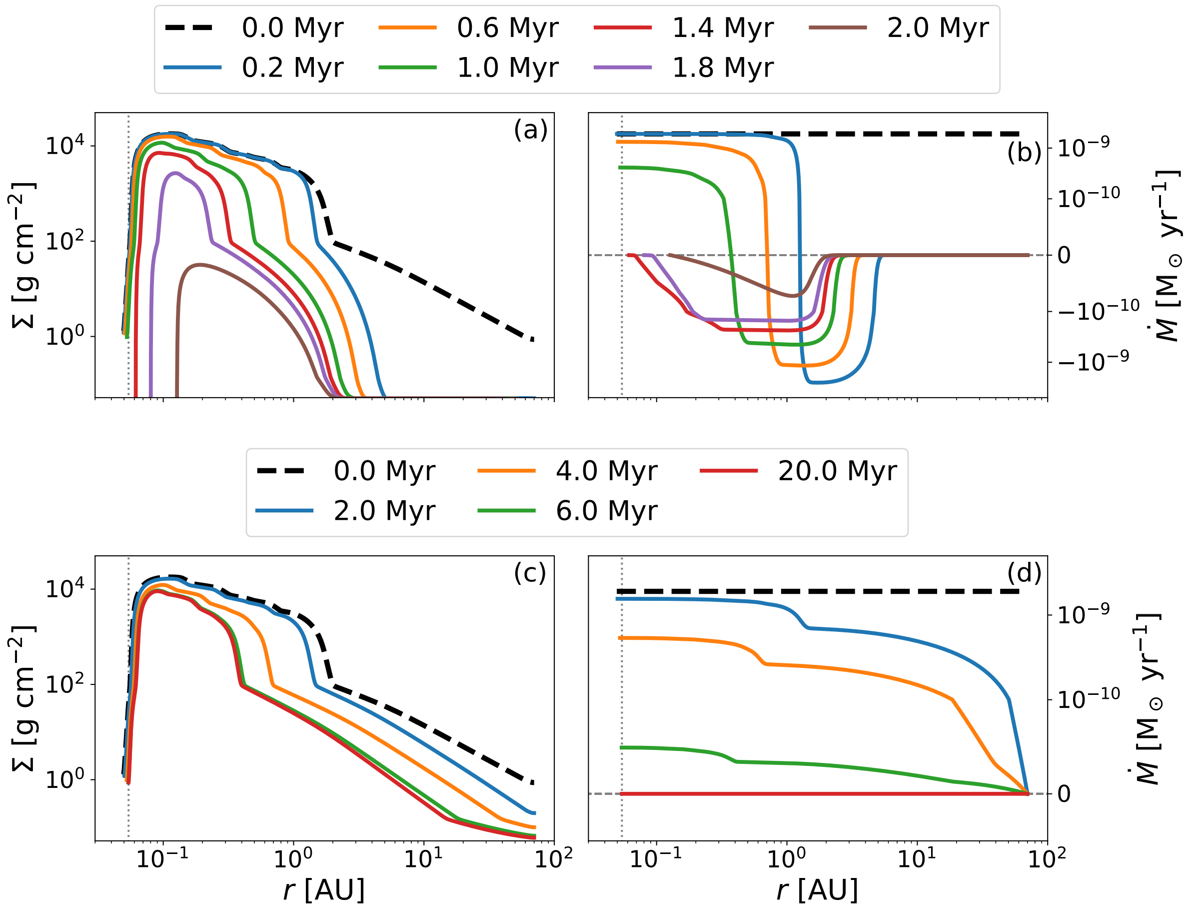

Figure 4.1: Column density and mass flux through the disk for certain times during the fiducial model simulation. *Panels a* and *b* show the time evolution of the column density and the mass flux respectively for the fiducial model `fid`. *Panels c* and *d* depict the evolution of the same quantities for the fiducial model without photoevaporation `fid_nPh` [2]. The vertical dotted grey line indicates the location of the corotation radius $r_{\rm cor}$. The horizontal dashed grey line in *panels b* and *d* marks $\dot{M} = 0$.

the mass flux as a function of disk radius is shown. The mass flux in the dead zone is always higher than in the outer disk. Additionally, as the radius increases, a steep drop in the mass flux develops, as can already be seen after 2 Myr. The two reasons for that are the low density in the outer disk and the large amount of angular momentum transported from the high-density regions in the inner disk which has to be taken over by the low-density outer disk. Combined with the negative gas pressure gradient, this effectively leads to a radially outward acceleration of the outer disk material, braking its initially radially inward flux. The larger the radius becomes, the smaller the density and the stronger the braking of the radial velocity is. As the disk evolves in time, this structure of the mass flux profile stays the same, but the absolute values become smaller

[2]The sharp bend of the mass flux profiles in *panel d* when they cross the value of $10^{-10}\ \mathrm{M_\odot\ yr^{-1}}$ (mostly noticeable in the 4.0 Myr profile) originates from the change of scale of the vertical axis: From 0 to $10^{-10}\ \mathrm{M_\odot\ yr^{-1}}$, the scaling is linear, while it is logarithmic from $10^{-10}\ \mathrm{M_\odot\ yr^{-1}}$ on towards larger values. The same scaling is applied *panel b* as well.

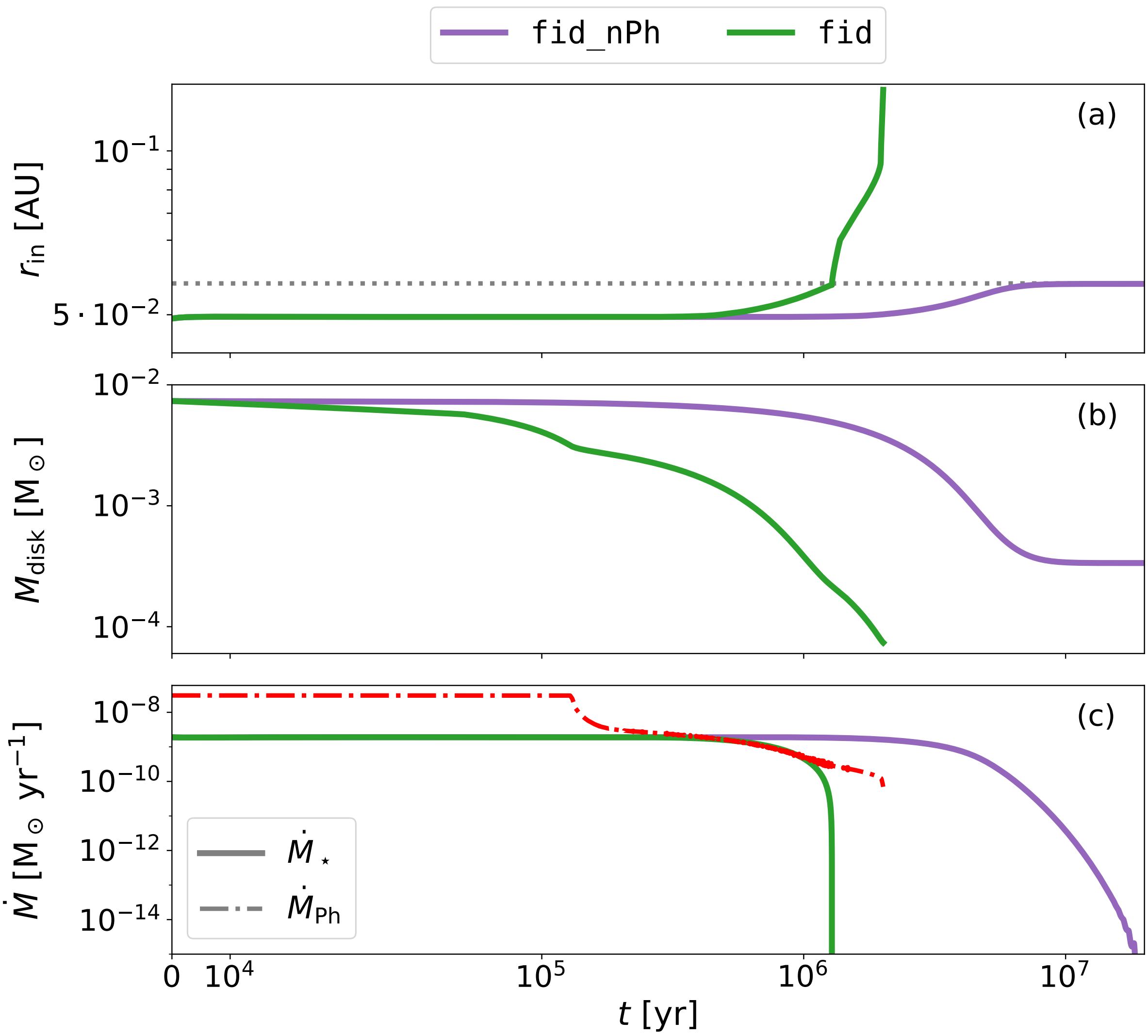

Figure 4.2: Time evolution of the position of *(a)* the inner disk boundary, *(b)* the disk mass and *(c)* the accretion rate for the fiducial model with and without photoevaporation. The horizontal dotted line in *panel a* indicates the location of the corotation radius r_{cor}. In *panel c*, the solid lines represent the accretion rate on the central star and the red dash-dotted line is the mass loss rate due to photoevaporation integrated over the whole disk for the `fid` model.

as the density in the outer disk decreases and the dead zone pulls back towards the star.

The reason for the strong decrease of accretion rate onto the star (see also panel c of Fig. 4.2) and the mass transport rate in the dead zone is the approach of the inner disk rim towards the corotation radius, which is shown in panel a of Fig. 4.2. Initially, the inner disk boundary lies well within the corotation radius, leading to a radially inward acceleration of disk material inside r_{cor} due to the magnetic braking by the stellar magnetic field (see Sec. 3.2.3). Resulting from the decreasing disk mass and overall surface density, the accretion rate slowly becomes smaller and the ram pressure of the accreting material decreases accordingly. This leads to an outward movement of the magnetic truncation radius, which is where the inner disk boundary is defined (See Sec. 3.2.5). At the new (further outward) location of the inner boundary, the accretion rate drops further (relative to the old location) because the braking of the azimuthal velocity by the magnetic field is less efficient due to the difference between stellar rotation velocity and Keplerian velocity being smaller. As the ram pressure at the inner boundary therefore continues to decrease, the inner boundary slowly moves towards the corotation radius before reaching it after approximately 8 Myr. At that time, the connection between the disk and the stellar magnetic field strives to let the disk material at the inner rim move at stellar rotation velocity in angular direction. In principle, at the location of the corotation radius, there is no torque from the stellar magnetic field imposed on the disk. But as soon as the viscous angular momentum transport tries to slow the material down at the inner rim (located at the corotation radius), the magnetic torque starts taking effect again and accelerates the disk again to corotation values, hindering the material from accreting onto the star. With the chosen viscous parameters, the angular momentum transport at the inner rim combined with the gas pressure force is not efficient enough to counter this effect. More precisely, the outer annulus next to the inner rim (which moves at a slower angular velocity) cannot cause enough viscous friction force on the inner annulus to surpass the magnetic torque, leading to a cessation of accretion onto the star. But the friction between the two annuli still causes the outer annulus to be accelerated in azimuthal direction, leading to an outward transport of angular momentum, which is now controlled by the magnetic torque forcing the inner rim to corotate with the stellar magnetic field. Eventually, an equilibrium is reached between the angular momentum coming from the inner rim, the gas pressure gradients and the viscous friction trying to move the material inwards and the mass flux throughout the disk comes to a stop. After this equilibrium is reached between every pair of annuli towards the outer boundary, the evolution of the disk becomes quasi-stationary with a remaining disk mass of $3.4 \cdot 10^{-4}$ $M_{\odot}$ (panel b of Fig. 4.2). With the chosen viscosity model, the torque exerted on the inner disk by the stellar magnetic field is even strong enough to retain a dead zone throughout the whole evolution towards the stationary state. This picture will change when the stellar magnetic field strength or the viscosity parameters are changed (see Sec. 4.3 and Sec. 4.4 respectively).

4.1.2 Evolution with photoevaporation: overall picture

When mass loss due to photoevaporation is included according to the description in Sec. 3.1.1, the evolution of the surface density and the mass flux through the disk changes significantly. Panel a of Fig. 4.1 shows that in the `fid` model, the disk outside of approximately 6 AU disappears completely during the first 0.2 Myr. Similarly to the `fid_nPh` model, the size of the dead zone continuously decreases, but on a much shorter timescale. Simultaneously, the size of the remaining disk shrinks as the outer rim is continuously driven further towards the star by photoevaporation. After the outer edge of the disk reaches $\sim$ 3 AU, its movement towards smaller radii slows down as the inner boundary crosses the corotation radius after about 1.4 Myr. While the inner rim of the disk is continuously pushed outwards, the dead zone disappears shortly before 2 Myr, leaving behind a small (< 2 AU), low-mass disk (with a remaining mass of $\sim 7 \cdot 10^{-5}$ $M_\odot$, see panel b of Fig. 4.2). While in the `fid_nPh` model the disk structure does not change significantly in the first 2 Myr, it almost disappears completely in the same time frame when photoevaporation is included, although the corresponding mass loss is vanishingly small in the innermost parts of the disk (See Fig. 3.2). This evolution can be explained when analyzing the behaviour of the mass flux through the disk. Panel b of Fig. 4.1 shows that after 0.2 Myr, the mass flux has changed from an inwards- to an outwards-directed movement, starting at the outer boundary of the dead zone. In the following, this location will be referred to as the *First Zero Radial Velocity Point* ($ZRVP_1$). The mass flux then becomes 0 again at $\sim$ 16 AU in this case (which will be referred to as $ZRVP_2$), which coincides with the location of the outer rim of the remaining disk in Fig. 4.1.

4.1.3 Evolution with photoevaporation: gap creation

The time up to 0.2 Myr of the fiducial model is resolved in more detail in Fig. 4.3 and Fig. 4.5. Fig. 4.3 shows the evolution of the surface density and the mass flux up to the point in time where a gap is created at $\sim$ 17 AU after 130 kyr, meaning that the surface density reaches $\Sigma_{\rm min}$ at this point in time at this location. In panel b, the development of the mass flux inversion is depicted. The red dash-dotted line shows the amount of mass that is taken out of the grid cell at the respective radius[3]. After 40 kyr, a dip in the mass flux profile can already be seen at the outer edge of the dead zone.

[3]One may notice that this profile looks different compared to the mass loss profile depicted in Fig. 3.2. The reason for that is, that Fig. 3.2 shows the reduction of the surface density (meaning g cm^{-2}) per time at a certain radius point. The photoevaporative mass loss profile in Fig. 4.3 and 4.5 depicts the lost mass per cell volume and per time of the grid cell at a certain radius, since $\dot{\Sigma}_{\rm ph}$ has to be multiplied with $V_{\rm S}$ in the discrete equation of continuity (Eq. 3.3.2). $V_{\rm S}$ is not constant throughout the disk due to the adaptive grid, but (generally) becomes larger at larger radii, which is why the profile of mass taken out of each cell due to photoevaporation takes the form depicted in Fig. 4.3. This depiction has been chosen, so that the mass flux through the disk and the photoevaporative mass loss are shown in terms of the same unit ($M_\odot$ yr^{-1}) and can therefore be better compared.

This can be understood in the following way: The initial constant mass flux through the disk is continuously diminished by the mass loss through photoevaporation. In the dead zone, the flux stays large enough and the photoevaporation is weak enough so that the viscous mass accretion onto the star is the same as for the `fid_nPh` model (at least in the time period depicted in Fig. 4.3). In the outer disk however, the flux becomes much smaller due to the smaller density, so that the influence of the photo-evaporative mass loss takes effect much sooner. Going to smaller radii, the time the flux from the outer disk spends in the region affected by photoevaporation increases, which makes the diminishment of the mass flux increasingly noticeable. This process continues down to the radius of the outer edge of the dead zone, within which a large mass flux is created that compensates the photoevaporative mass loss. As time progresses, the mass flux coming from the outer disk becomes smaller due to the same reasons as in the `fid_nPh` model (with additional decrease by photoevaporation). After around 49 kyr, the integrated mass loss due to photoevaporation from the disk's outer boundary to the outer edge of the dead zone is larger than the total mass flux from the outer disk reaching the dead zone[4]. Therefore, the mass flux coming from the outer disk is fully photoevaporated as it reaches approximately 2 AU, creating a single ZRVP. It splits up into $ZRVP_1$ and $ZRVP_2$ as the mass flux in the outer disk decreases further. The $ZRVP_2$ starts moving outwards because the erasement of the inward mass flux by photoevaporation occurs sooner (i.e. further outside). Meanwhile the $ZRVP_1$ remains at the outer border of the dead zone since inside this radial point, the initial inward flux of mass can still be kept up by viscous angular momentum transport. Obviously, this angular momentum has to be taken up by the material just outside the dead zone, which now does not receive any mass flux from the outer disk (and therefore there is no inward advection of radial momentum). In addition to that, the density gradient and therefore the gas pressure gradient is negative and has a large absolute value at the outer edge of the dead zone, where the $ZRVP_1$ is located. A negative gas pressure gradient causes an outwards directed force on the disk material. This means that the angular momentum received from the inner disk combined with the negative gas pressure gradient leads to an acceleration and outward movement of the matter between the two ZRVPs, creating the mass flux inversion.

The $ZRVP_2$ is a location where the mass loss is very effective because (i) there is no resupply of material by a flux from neither the outer nor the inner disk and (ii) the photoevaporative process still operates. In panel a of Fig. 4.3, the position of the $ZRVP_2$ for the density profile of the same color is indicated by the vertical dashed lines. The time evolution shows that the $ZRVP_2$ moves outwards until it reaches a specific location between 10 AU and 20 AU, which is where the gap is created (i.e. where the density

[4]In other words, every particle that starts flowing inwards outside the dead zone is evaporated before it can reach the outer edge of the dead zone.

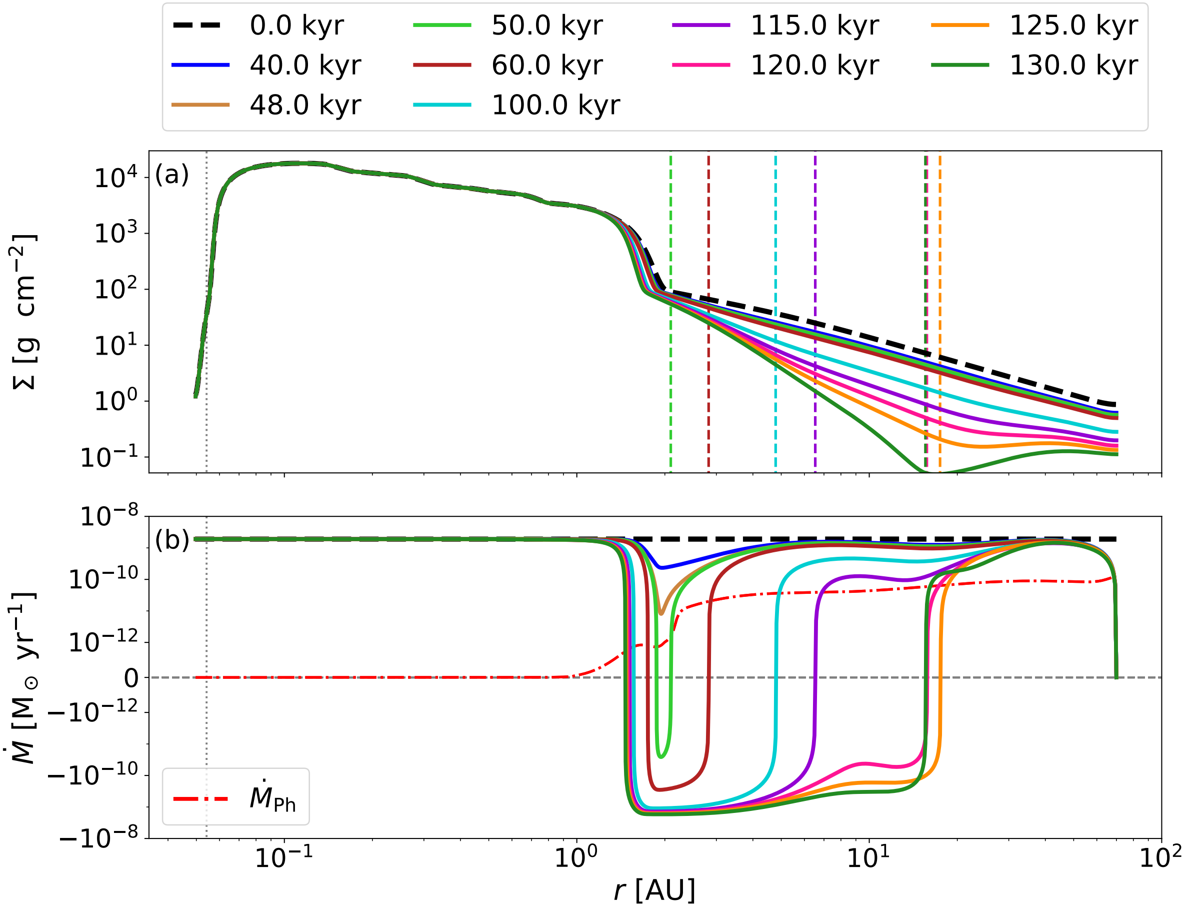

Figure 4.3: *(a)* Column density and *(b)* mass flux through the disk during the gap creation process in the fiducial model simulation `fid`. The vertical dotted grey line indicates the location of the corotation radius $r_{\rm cor}$, while the vertical dashed lines signalise the location of the ZRVP$_2$ at the corresponding time of the density profile of the same color. The horizontal dashed grey line in panel b marks $\dot{M} = 0$. The red dash-dotted line represents the photoevaporative mass loss rate in the respective grid cell. Over the depicted time period, the photoevaporative mass loss rate stays constant.

first reaches $\Sigma_{\rm min}$). This can be understood in the following way: During its outward movement, the ZRVP$_2$ 'scrapes' away material from the disk. As long as the density at the location of the ZRVP$_2$ is high enough, not enough mass can be removed from that location to reach $\Sigma_{\rm min}$ and create a gap before the ZRVP$_2$ moves further outwards. But at some radius, the density is already low enough by a combination of viscous flux and photoevaporation, in order for the photoevaporation around the ZRVP$_2$ to have sufficient time to remove all the remaining mass in that location, creating a gap and separating the disk into an inner and an outer part. As stated above, the mass loss rate at the exact location of the ZRVP$_2$ is purely determined by photoevaporation, as there is no mass flux arriving from neither outside nor inside. The velocity at which the ZRVP$_2$ moves outwards depends on the inward mass flux in the outer disk and the gas pressure gradient on both sides: If the mass flux in the next cells outside of the ZRVP$_2$

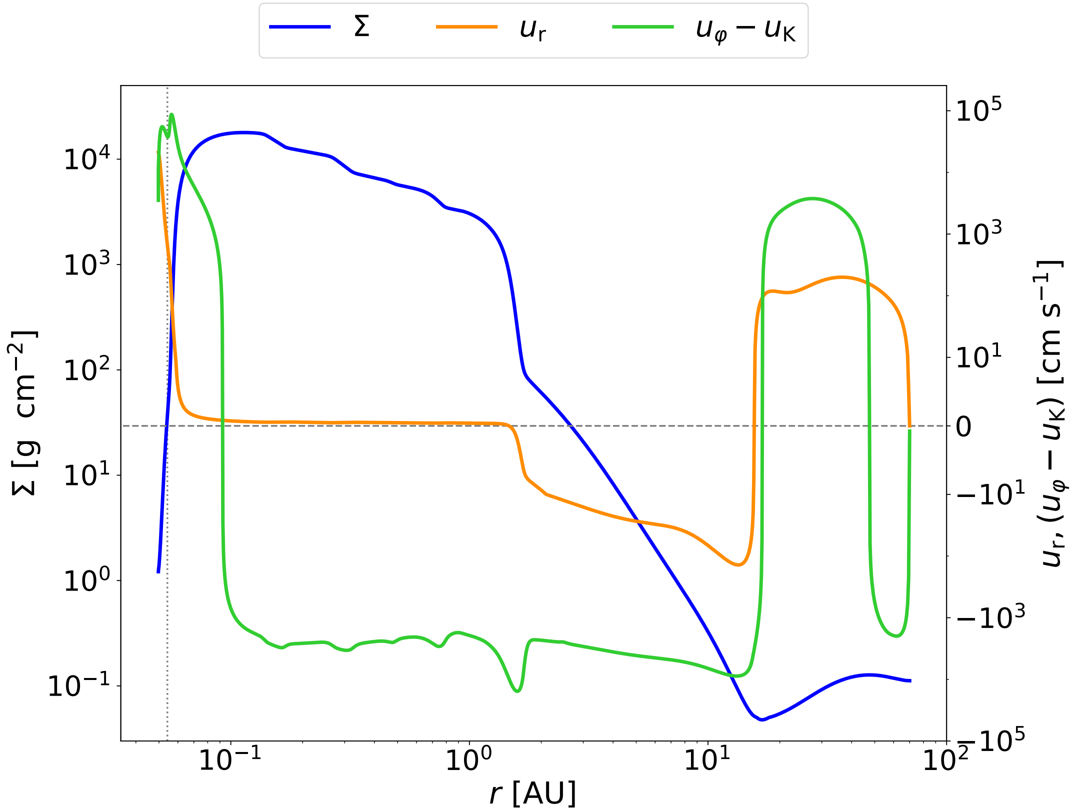

Figure 4.4: Surface density Σ, radial velocity u_{r} and difference between the azimuthal and Keplerian velocity $u_\varphi - u_{\mathrm{K}}$ of the `fid` model at the time of gap creation after 130 kyr. The horizontal, dashed, grey line illustrates where the radial velocity changes its direction and where the rotational velocity transitions between sub- and superkeplerian, respectively. The vertical, grey, dotted line marks the corotation radius.

is large, photoevaporation needs more time to diminish it to 0 so that the ZRVP$_2$ can move further. As a dip in the surface density profile develops, the steepening pressure gradients inwards and outwards of the ZRVP$_2$ try to push material into the developing gap. The effects of this can be seen in Fig. 4.4, which shows the radial profiles of the surface density, the radial velocity and the deviation of the rotational velocity from the Keplerian velocity at the time of gap creation. As was the case for the mass flux, a positive value of u_{r} corresponds to a motion towards the star. In the radial velocity profile, the ZRVP$_1$ and ZRVP$_2$ are visible at the outer edge of the dead zone and at the location of the gap. The gas pressure gradient can essentially be inferred from the surface density gradient, since the gas pressure is proportional to the density, both of which are linked via the equation of state. The sign of $u_\varphi - u_{\mathrm{K}}$ behaves according to Eq. 3.1.5: In regions where a negative gas pressure gradient is present, the rotational velocity is smaller than Keplerian and vice versa[5]. Outside the dead zone, the pressure gradient and consequently the deviation from the Keplerian velocity continuously

[5]Note, that $u_\varphi - u_{\mathrm{K}}$ sharply decreases towards the star inside the corotation radius due to the braking by the stellar magnetic field.

decreases towards the gap until it reaches a minimum after which it becomes positive again on the outside 'wall' of the gap. A similar behaviour can be observed in the radial velocity profile. As the surface density becomes smaller and the gas pressure gradient larger towards the gap coming from smaller radii, the outward radial velocity increases until it spikes just inside of the gap location, following the less pronounced spike in the $u_\varphi - u_\mathrm{K}$ profile. A similar 'spike' (but less distinct due to the smaller absolute value of the pressure gradient compared to the inner 'wall' of the gap) can be observed just outside of the gap, in the opposite direction. This means that the pressure gradients around the gap increasingly dominate the radial velocity and are working to push material back into the gap. For that reason, gap creation is impeded when the influence of pressure gradients are considered in the simulations compared to disk models using e.g. the common diffusion equation.

In summary, the position at which the gap is created depends on the following factors:

- The magnitude of the inward mass flux in the outer disk (determined, in part, by the initial mass flux and the viscosity description) and the outward mass flux outside the dead zone, which control the speed at which the ZRVP_2 moves outwards
- The gas pressure gradients around the ZRVP_2 once a dip in the surface density profile is developed
- The surface density at the location of the ZRVP_2
- The photoevaporative mass loss rate at the ZRVP_2

The point in time when the gap is created is also visible in Fig. 4.2: The photoevaporative mass loss rate suddenly drops when the gap is created after 130 kyr because no more mass can be taken out of the area of the gap. This also leads to a flattening of the disk mass evolution function at this point. The photoevaporative mass loss then causes the gap to broaden, separating the inner and the outer disk from each other. The mass fluxes coming from both sides are not large enough to counter the mass loss and refill the gap. The ZRVP_2 stays at the outer edge of the inner disk which is driven towards smaller radii, which can already be seen in Fig. 4.3 since the ZRVP_2 is closer to the star at 130 kyr than it was at 125 kyr.

Fig. 4.5 shows the further evolution of the surface density and the mass flux after gap creation. The outer rim of the inner disk continues to be driven back towards the star by the continuous photoevaporative mass loss. The same process is operating at the inner edge of the remaining outer disk, driving it further outwards. At the same time, the surface density over the whole outer disk decreases by the combined effects of photoevaporative mass loss and the still existing mass flux towards the gap. Due to numerical reasons, the surface density in the gap can not drop all the way to 0 g cm^{-2}.

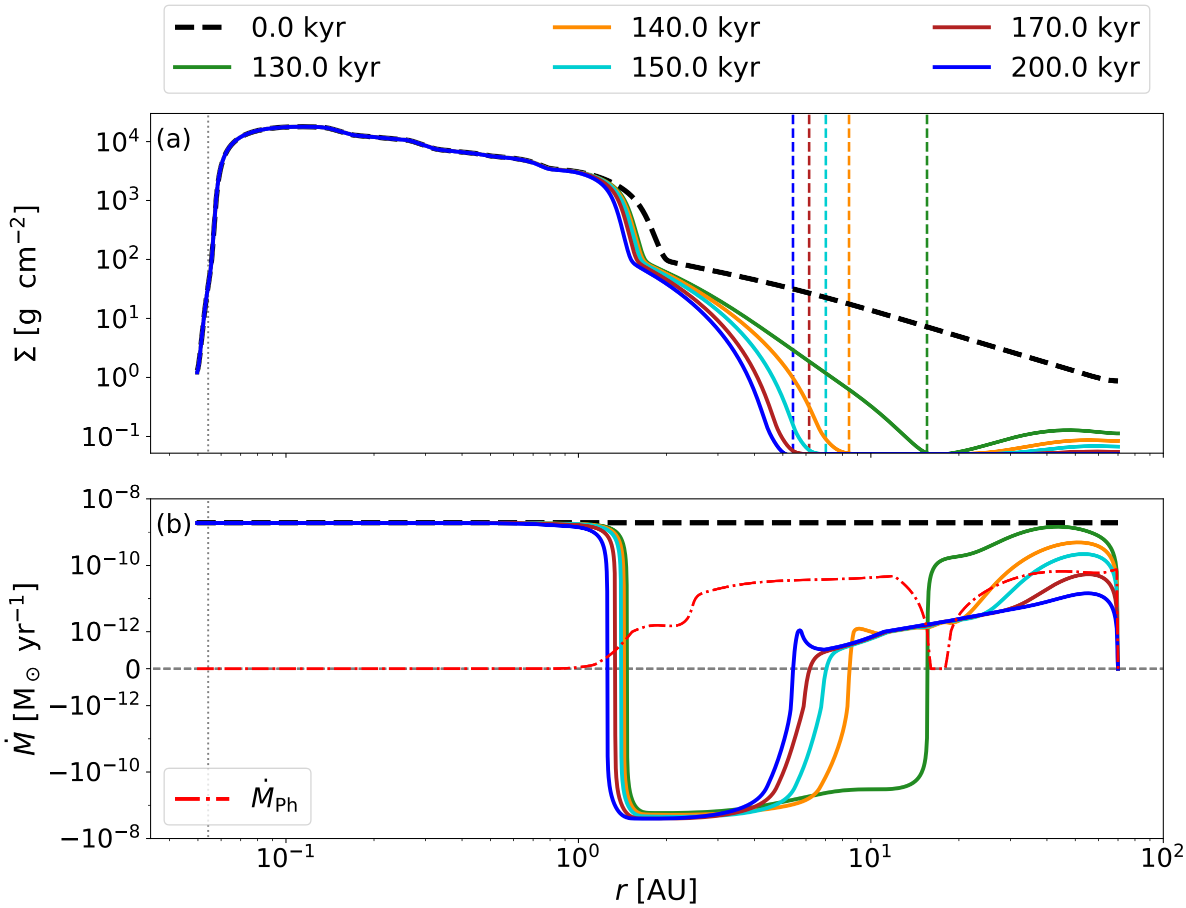

Figure 4.5: Same as Fig. 4.3 for times after gap creation. The depicted photoevaporative mass loss rate (red dash-dotted line) was taken from the model at 130 kyr, where the density in the gap is low enough that the factor $v(\Sigma(r))$ reduces the mass loss to avoid numerical problems (Sec. 3.3.2). The model at 130 kyr is the same as in Fig. 4.3 and the model at 200 kyr is the same as in Fig. 4.1.

This is controlled by the factor $v(\Sigma(r))$, which is included in the photoevaporation terms in the discrete set of equations (Eqs. 3.3.2 - 3.3.5) and in the viscosity description (Eq. 3.2.5). It ensures that the photoevaporative mass loss stops and the viscosity is set to its minimum value $\alpha_{\rm base}$ when the surface density reaches $\Sigma_{\rm min}$. Due to the very small (but non-zero) viscosity, a minuscule mass flux, unaffected by photoevaporation, can develop in the gap, which is visible in panel b of Fig. 4.5. But this flux does not contribute in any significant way to the evolution of the inner or the outer disk.

4.1.4 Evolution with photoevaporation: inner disk dispersal

After 200 kyr, the outer disk has already disappeared entirely (i.e. the surface density reaches $\Sigma_{\rm min}$ everywhere) and the inner disk has a maximum radius of $\sim$ 6 AU. This state of the disk is also depicted in Fig. 4.1 where the long-term evolution over the whole disk lifetime is shown. Up to a time of 1 Myr, the overall structure of the surface density and the mass flux stays about the same. The size of the dead zone decreases, with the ZRVP_1 staying at its outer edge. The outer boundary of the remaining disk (coinciding with the ZRVP_2) continues to move closer towards the star. Meanwhile, similarly to the `fid_nPh` model, the inner boundary of the disk moves outwards due to the continuously decreasing ram pressure of the accreting material. Between 1 Myr and 1.4 Myr, the inner boundary of the disk reaches the corotation radius and the accretion onto the star ceases for the same reasons as for the `fid_nPh` model described above. But in the evolution of the `fid` model, the transport of angular momentum from the inner boundary at $r_{\rm cor}$ outwards encounters a disturbance at the ZRVP_1, where the mass flux and the radial velocity vanish. That means that the disk material in the annulus at this point does not inherit any radial momentum. When it now takes over the angular momentum coming from the inner annulus by viscous friction, it receives an outward radial momentum from the centrifugal force, which causes the material in the annulus to flow outwards. This is further aided by the negative gas pressure gradient, causing an outwards directed force. At the same time, the inner annulus does not receive any mass flux or radial momentum from the outer one, which leads to the cessation of radial flux at this location. This means that during this process, the ZRVP_1 moves from the outer annulus to the inner one. This mechanism then repeats itself for every annulus pair in the inner disk until the ZRVP_1 reaches the inner boundary.

This stage of the disk's evolution (from the dispersal of the outer disk at 0.2 Myr to the crossing of the corotation radius by the inner boundary) is shown in Fig. 4.6. Panels a and b are of the same structure as in Fig. 4.3 and Fig. 4.5, but in this case, the location of the ZRVP_1 at the corresponding times is indicated by the vertical dashed lines in the $r - \Sigma$ plot (panel a). The speed at which the ZRVP_1 moves depends on the magnitude of the mass flux towards the star inside this radius point. The movement starts immediately after the flux inversion is created at the outer edge of the dead zone, but at an initially very small velocity compared to the ZRVP_2 movement (as evident in Fig. 4.3 and Fig. 4.5). This is because the inward mass flux in the dead zone is large, so the angular momentum transported outwards towards its edge needs a long time to reduce the inward radial momenta in the inner annuli next to the location of the ZRVP_1. But as the flux in the dead zone decreases (due to the decreasing density and the approach of the inner boundary towards the corotation radius), the inward movement of the ZRVP_1 is facilitated until it even crosses the dead zone and reaches the inner boundary of the disk. As will be discussed in Sec. 4.3.1, the underlying cause of this is the propelling effect of the magnetic torque at the inner disk boundary. At this point in time, the mass flux throughout the whole remaining disk is directed away from the star. Consequently, there can also be no ram pressure $P_{\rm ram}$ in the star's direction, which means that the magnetic truncation radius (where the inner boundary of the disk is defined) is located at the point where the magnetic pressure from the stellar magnetic

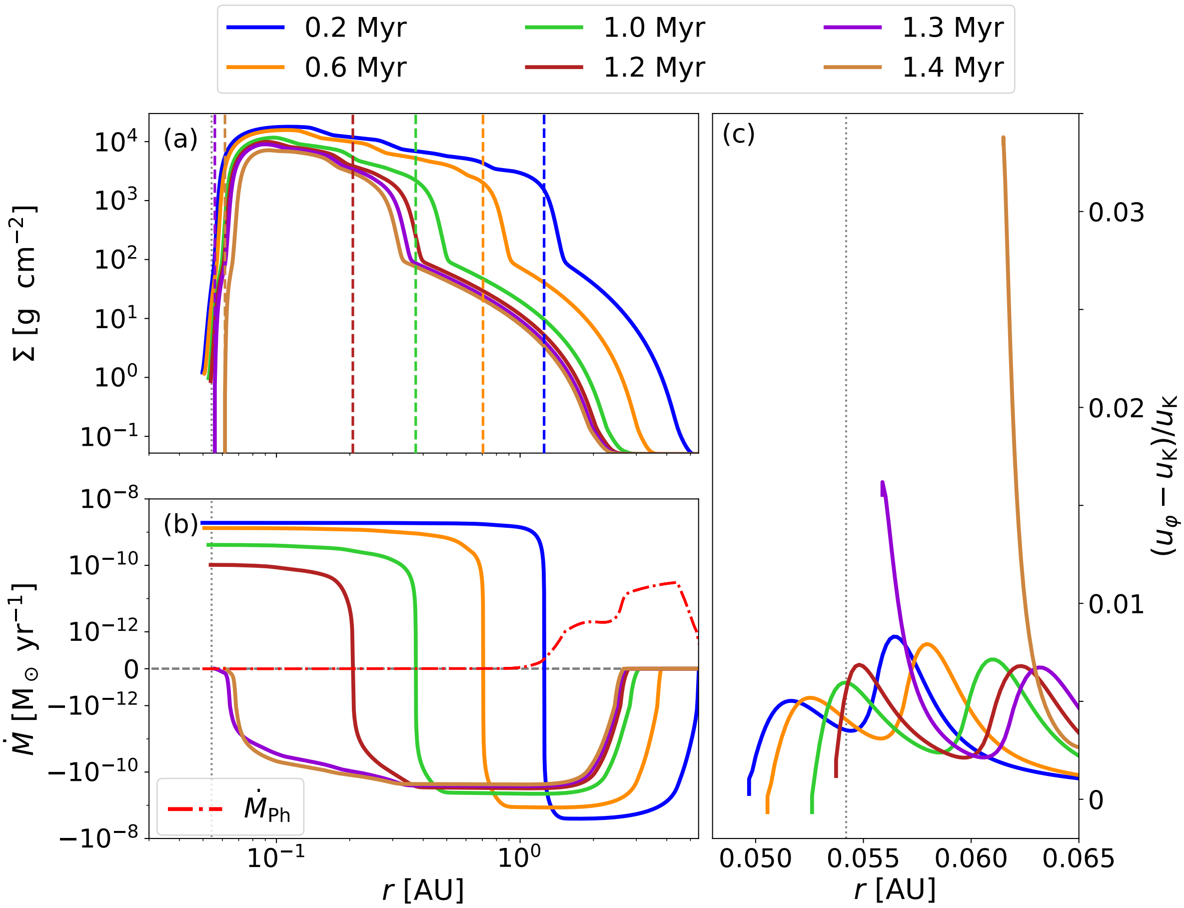

Figure 4.6: Evolution of *(a)* surface density, *(b)* mass flux and *(c)* deviation from Keplerian orbital velocity in the vicinity of the corotation radius for times after the outer disk has disappeared. The vertical dashed lines in *panel a* represent the position of the ZRVP_1 of the density profile of the same color. The horizontal grey dashed line, the vertical grey dotted line and the red dash-dotted line mark the same quantities as in Fig. 4.3 and Fig. 4.5. The depicted photoevaporative mass loss rate is the one corresponding to the model at 0.2 Myr.

field is equal to the gas pressure P_{gas} (See Sec. 3.2.5). Since the mass flux is pointed outwards throughout the whole disk, the density at the very inner edge of the disk decreases as well, which also leads to a decrease of the gas pressure. Therefore, the location of the inner boundary does not stop at the corotation radius as was the case in the `fid_nPh` model, but can move beyond it, as depicted in panel a of Fig. 4.2. This reinforces the outwards flux of material away from the inner edge of the disk through the propeller effect (See Sec. 3.2.5), which is indicated in panel c of Fig. 4.6. This plot shows the deviation from the Keplerian velocity at radial points close to the corotation radius. At such small radii, the azimuthal velocity tends to be super-Keplerian due to the influence of the gas pressure gradient force (see analysis by Steiner et al. (2021)). The oscillations in the $(u_\varphi - u_\mathrm{K})/u_\mathrm{K}$ profile (which will not be analysed here in detail) results from the delicate interplay between the influences of the stellar magnetic field, the gas pressure gradient and viscosity. The focus now lies on the behaviour of u_φ at the inner boundary. As long as the inner boundary resides within the corotation radius, u_φ is slowed down towards the star due to the braking by the magnetic torque. But the braking turns into an acceleration as soon as the inner rim of the disk moves beyond the corotation radius, because at these locations, the magnetosphere moves at a larger angular velocity than the disk material and therefore the magnetic torque is parallel to u_φ (as opposed to anti-parallel inside the corotation radius). This large azimuthal velocity at the inner boundary leads to an increased centrifugal force, overcoming the gravitational pull and pushing the disk material away from the star. As a further result, the gas pressure at the inner boundary decreases rapidly, leading to an accelerated outward movement of the inner boundary after it crosses the corotation radius (panel a in Fig. 4.2).

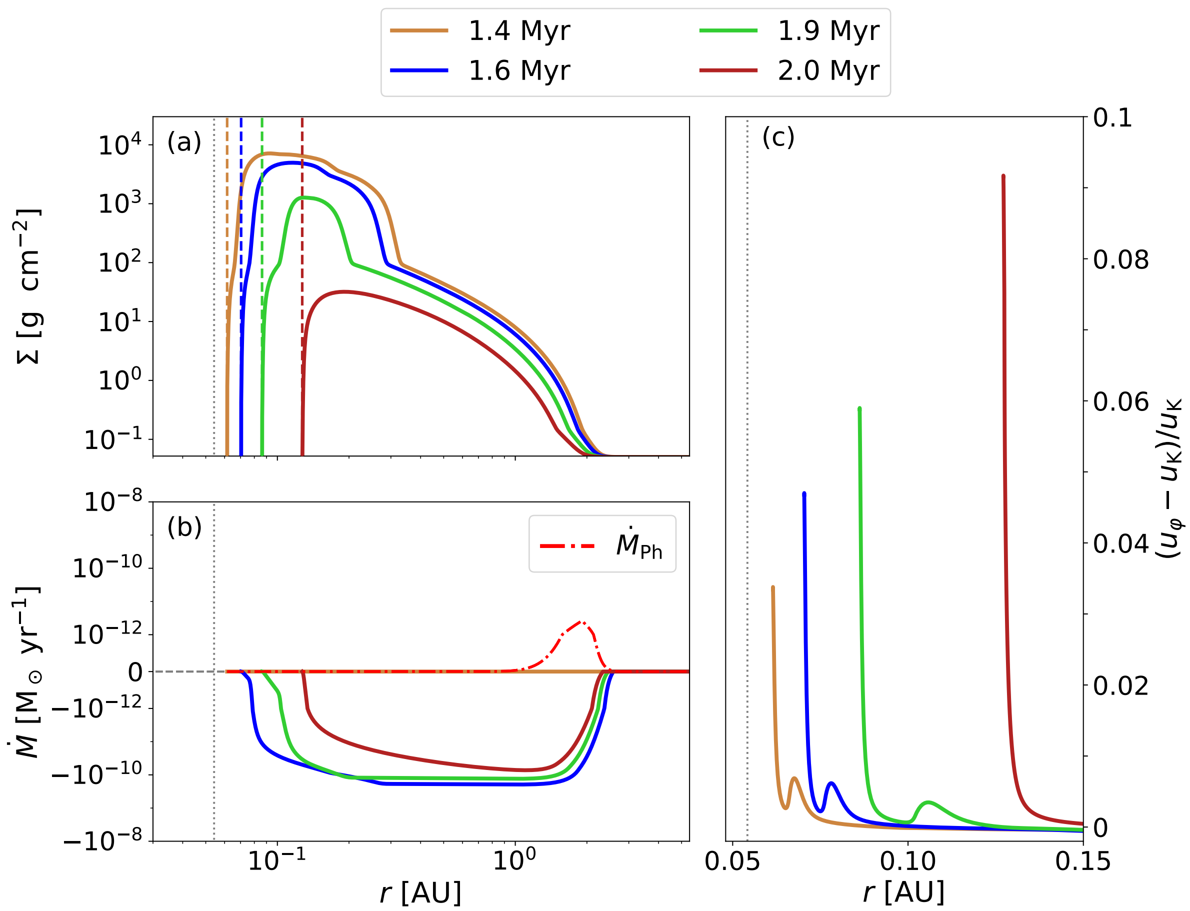

Figure 4.7: Same as Fig. 4.6 for times after the inner boundary of the disk crossed the corotation radius. The photoevaporative mass loss rate (red dash-dotted line in *panel b*) corresponds to the model at 1.4 Myr.

The further the inner boundary moves beyond the corotation radius, the stronger the acceleration becomes, as can be seen in panel c of Fig. 4.7. The two plots on the left hand side show the further evolution of the surface density and the mass flux through the disk after the inner boundary has crossed the corotation radius. The azimuthal ac-

celeration at the inner boundary is also visible in the mass flux evolution, where the gradients of the depicted functions at the inner edge steepen as time evolves and the boundary moves outwards. Between 1.9 Myr and 2 Myr, the dead zone dissolves, increasing the viscosity in that area which facilitates the angular momentum transport and the outward mass flux. The consecutive drop in gas pressure at the inner boundary accelerates its outward movement, which is why its movement velocity is larger between 1.9 Myr and 2 Myr than it was before.
While the inner boundary moves away from the star, the outer rim of the disk travels inwards only slowly due to the outward flux of material from the whole disk on the one hand and the decrease of the photoevaporative mass loss rate at such small radii (red dash-dotted line in Figs. 4.3 - 4.7) on the other hand. During the latest stage of the evolution (Fig. 4.7), the outer boundary of the disk is located at the point where the outward mass flux has been evaporated away entirely. With time, the inverted accretion flux carries the mass of the whole remaining disk outwards into the region where photoevaporation is effective, which eventually leads to the complete dispersal of the disk.

4.2 Variation of stellar luminosity

The next step in analyzing the influence of photoevaporation on the evolution of a protoplanetary disk is the variation of the stellar luminosity. The parameters used for the simulation runs concerning this aspect are listed in Tab. 4.3. The stellar magnetic field strength $B_\star$, and the viscosity parameters α_{MRI} and α_{base} are kept at their fiducial values (see Tab. 4.2). As already explained in the context of the fiducial model, the stellar luminosity has been chosen in a way that it results in X-ray luminosities L_{X} of 10^{29} erg/s (`LX29`), 10^{30} erg/s (`fid`) and 10^{31} erg/s (`LX31`) according to Eq. 3.2.13) for the different models. For the three X-ray luminosities, the corresponding photoevaporative mass loss profile (Fig. 3.2) was implemented with the respective soft X-ray luminosity $L_{\mathrm{X,soft}}$ entering Eq. 3.1.6.
Fig. 4.8 shows the evolution of the surface density of the disk for all six simulations. The panels for the photoevaporating and non-photoevaporating fiducial model (b and e) are the same as in Fig. 4.1. It is clear immediately that the timescale of the evolution decreases with increasing luminosity, which can also be seen in Fig. 4.9, where the time evolution of the inner disk boundary, the disk mass, the accretion rate and the photoevaporative mass loss rate are shown. This is true for both photoevaporating and non-photoevaporating models, respectively.

Model	$L_\star$ $[L_\odot]$	L_X $[\mathrm{erg\ s^{-1}}]$	$L_\mathrm{X,soft}$ $[\mathrm{erg\ s^{-1}}]$	$\dot{M}_\mathrm{init}$ $[M_\odot\ \mathrm{yr^{-1}}]$	Ph
fid	1.4	10^{30}	$0.47 \cdot 10^{30}$	$1.90 \cdot 10^{-9}$	x
fid_nPh	1.4	10^{30}	$0.47 \cdot 10^{30}$	$1.90 \cdot 10^{-9}$	
LX29	0.14	10^{29}	$0.53 \cdot 10^{29}$	$1.25 \cdot 10^{-9}$	x
LX29_nPh	0.14	10^{29}	$0.53 \cdot 10^{29}$	$1.25 \cdot 10^{-9}$	
LX31	14.0	10^{31}	$0.42 \cdot 10^{31}$	$3.20 \cdot 10^{-9}$	x
LX31_nPh	14.0	10^{31}	$0.42 \cdot 10^{31}$	$3.20 \cdot 10^{-9}$	

Table 4.3: Run parameters for simulations with different stellar (X-ray) luminosities.

4.2.1 Initial models

Differences between the simulation runs are already evident in the initial models. The dashed, black-rimmed lines in Fig. 4.10 show the initial conditions for the surface density (panel a) and the mass flux through the disk (panel b). The photoevaporating and non-photoevaporating models for a certain stellar luminosity share the same initial configuration. Between the three models with different luminosities, there is as good as no difference in surface density of the disk outwards of 9 AU. Going to smaller radii from there, the profiles start to spread apart from each other, leading to differences in the radii where surface density reaches Σ_0, α starts to drop and the dead zone establishes itself. This spreading of the density profiles can be explained by analyzing the behaviour of the kinematic viscosity through the disk in the initial models. Fig. 4.11 shows the midplane gas temperature, the kinematic viscosity and the vertically integrated viscosity for the initial models with dashed, black-rimmed lines. Note that the gas temperature in the inner disk almost reaches the MRI activation temperature in the LX31 and LX31_nPh models, which would possibly lead to thermal instabilities and the commencement of episodic accretion events. Due to stronger irradiation by stars with higher luminosities, the temperature in the disk rises as the stellar luminosity increases. This also leads to a higher kinematic viscosity since it scales linearly with the isothermal sound speed and the pressure scale height (Eq. 3.2.4), which both increase with higher temperature. Outside of 9 AU, the gas temperature and kinematic viscosity profiles stay parallel to each other. The larger initial mass fluxes for models with higher luminosities (see Tab. 4.3 and panel b of Fig. 4.10) are responsible for establishing the same surface density for all models in this region. But between 9 AU and the outer rim of the dead zones, the temperature profiles rise towards smaller radii and are no longer parallel, but spread apart as the temperature of the LX31 model starts rising further outward already. This spreading directly transfers to the kinematic viscosity profiles. Since the mass flux in the initial model is constant throughout the disk, the increase of the ratio between the kinematic viscosities of the models with different luminosities relative

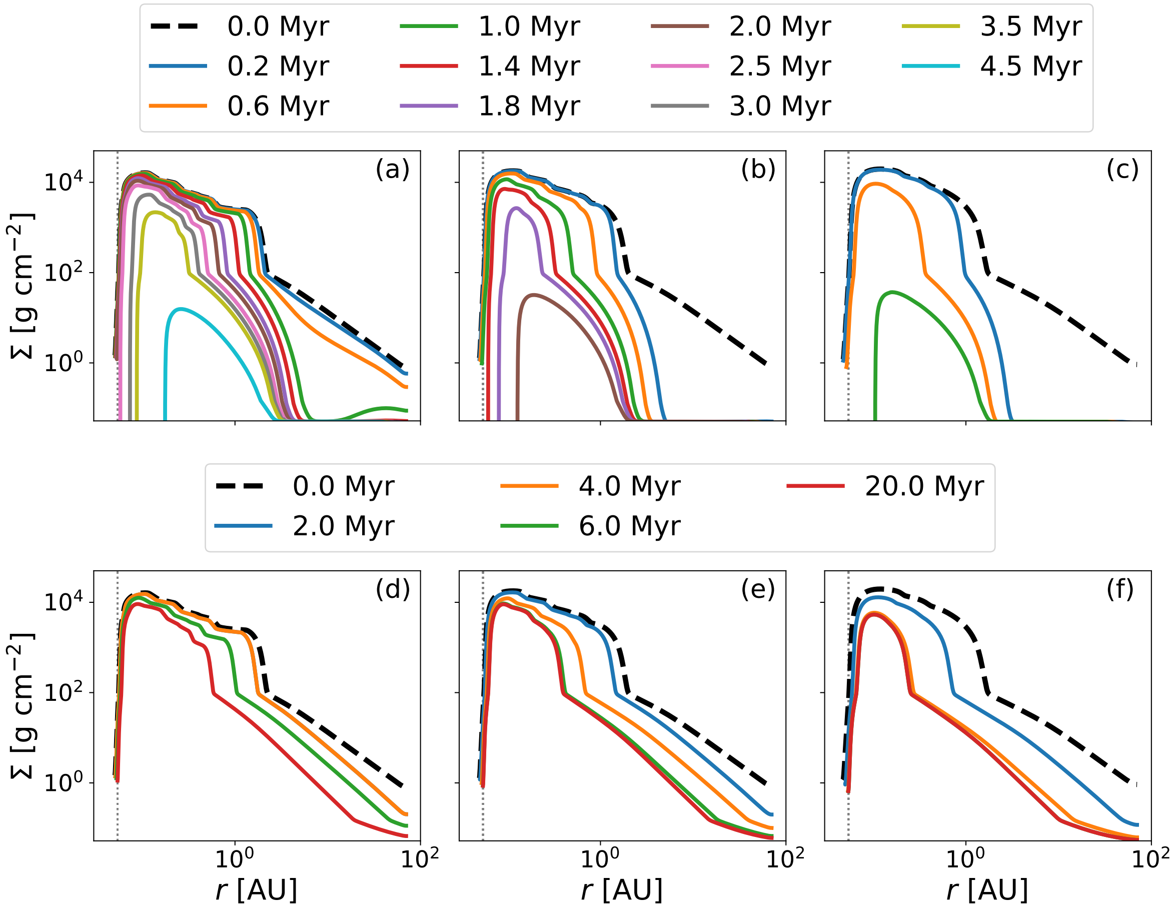

Figure 4.8: Evolution of the disk surface density for the 6 models parametrized in Tab. 4.3. *Panels a-c* show the photoevaporating models `LX29`, `fid` and `LX31` (from left to right) and *panels d-f* depict the non-photoevaporating models `LX29_nPh`, `fid_nPh` and `LX31_nPh` (from left to right). The initial configuration is shown as black dashed lines. The vertical dotted grey line marks the position of the corotation radius. This figure illustrates the different timescales at which the models evolve towards dispersal or a final disk structure, respectively.

to the disk outward of 9 AU shows itself in differences between the surface density profiles as observed in panel a of Fig. 4.10. Inside the dead zone, the temperature profiles converge again and the kinematic viscosity drops to low values for all models due to the decrease of the α parameter when deep layers are present (Configuration 2 in Tab. 3.2). Since the kinematic viscosities take similar values for all three models inside the dead zone, the higher (constant) mass flux for the higher luminosity models results in larger surface densities inside the dead zone. The trends present in the gas temperature profiles can not be seen in the initial integrated viscosity profiles (Fig. 4.11, panel c), which scales directly with the surface density (Eq. 3.2.6). A small spike can be observed at the outer edge of the dead zone where there is a rapid increase in the surface density (going from outside-in).

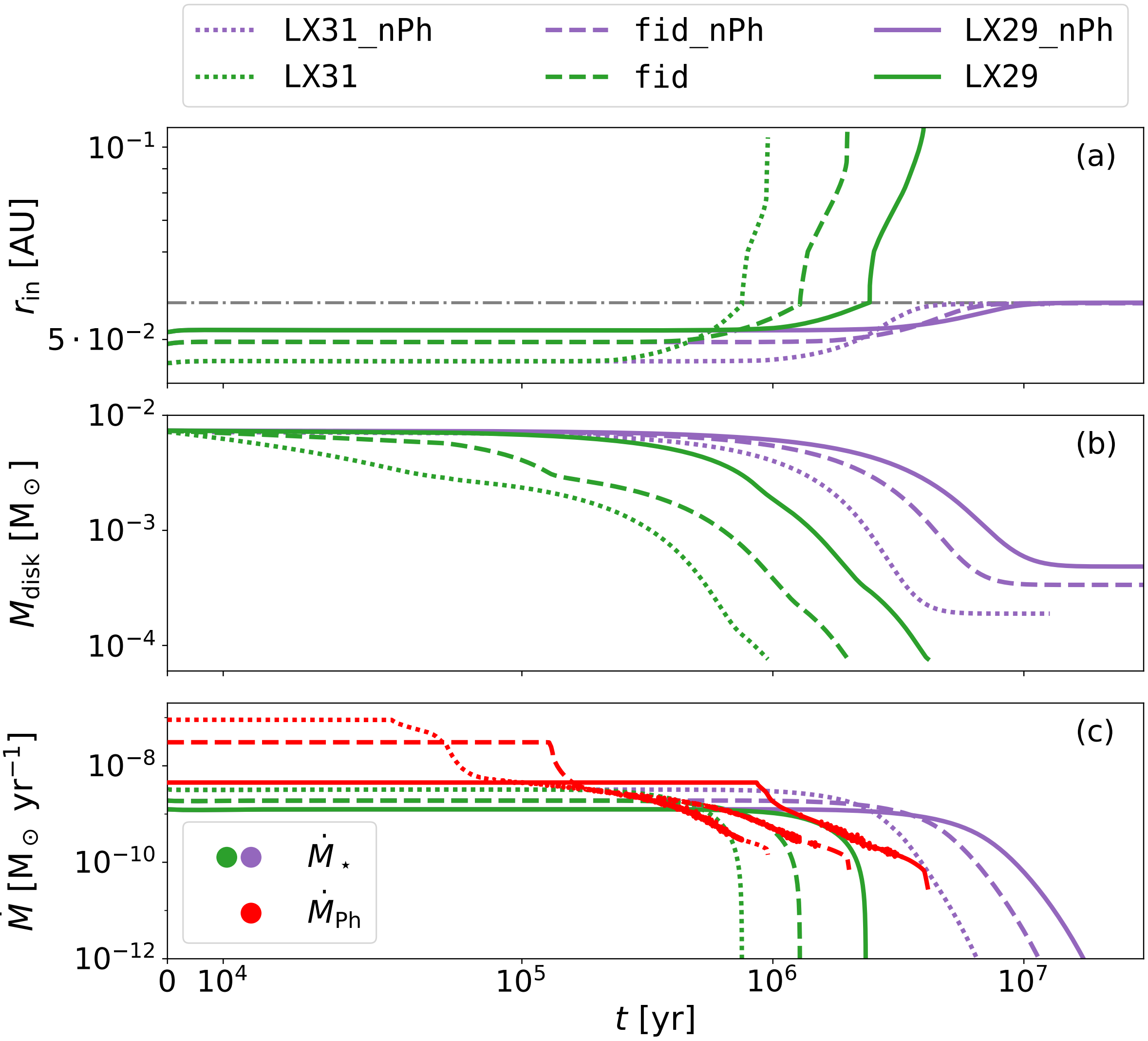

Figure 4.9: Analogous to Fig. 4.2, the time evolution of the position of *(a)* the inner boundary, *(b)* the disk mass and *(c)* the accretion rate onto the star for the models with varying stellar luminosities are shown. In *panel c*, the photoevaporative mass loss rates for the respective models are depicted in red.

4.2.2 Evolution without photoevaporation

The panels d-f of Fig. 4.8 show that the overall evolution process is the same for all three non-photoevaporating models and is explained in detail in Sec. 4.1.1. The timescale on which the disk evolves towards the stationary state decreases as the stellar luminosity increases due to both the larger initial mass flux and the higher viscosity (panels b and c of Fig. 4.11), leading to a shorter viscous timescale ($t_\nu = r^2/\nu$). Tab. 4.4 shows the time when the simulations reach the stationary state, defined as the time when the accretion rate onto the star stops (which is approximately when the inner boundary of the disk reaches the corotation radius). The `LX29_nPh` model takes almost three times as long as the `LX31_nPh` model to become stationary. Panel b of 4.9 indicates that the remaining disk mass in the stationary state is higher for the low luminosity models. The absolute values are noted in Tab. 4.4. The reason for that lies once again in the differences in gas temperatures and viscosities. Panel c of Fig. 4.11 shows that the vertically integrated viscosity is the same for all three models at every radius in the stationary state (green dotted line). As explained in Sec. 4.1.1, the simulation becomes stationary when an equilibrium is established between the angular momentum transported outwards from the inner boundary (which is determined by the connection between the stellar magnetosphere and the disk at the corotation radius) and the viscous friction. The magnetic torque at the inner boundary of the disk is the same for all three models when the inner rim reaches the corotation radius, therefore the structure of the vertically integrated viscosity also has to be equal in order to counter the resulting angular momentum transport and reach the final, stationary state. In order to achieve these integrated viscosities, the differences between the temperatures and therefore the kinematic viscosities in the final stationary states of the three models (Panels a and b in Fig. 4.11) have to be compensated by differences in surface density (See Eq. 3.2.6): A model with a higher kinematic viscosity (i.e. higher stellar luminosity) requires a lower surface density to reach the same vertically integrated viscosity as the lower luminosity model. Since the kinematic viscosity in the final, stationary state of a higher luminosity model is equal or greater than the one of the lower luminosity model at every radius, the remaining total disk mass is smaller if the stellar luminosity is larger.

Model	$t_{\rm gap}$ [ky]	$r_{\rm gap}$ [AU]	$M_{\rm disk}^{(t=t_{\rm gap})}$ $[M_\odot]$	$M_{\rm disk,outer}^{(t=t_{\rm gap})}$ $[M_\odot]$	$t_{\dot{M}_\star=0}$ [Myr]	$M_{\rm disk,stat}$ $[M_\odot]$
`fid`	130.5	16.8	$3.08 \cdot 10^{-3}$ $(0.44 \cdot M_{\rm disk,init})$	$1.8 \cdot 10^{-4}$ $(0.03 \cdot M_{\rm disk,init})$	1.28	
`fid_nPh`					18.4	$3.3 \cdot 10^{-4}$ $(0.05 \cdot M_{\rm disk,init})$
`LX29`	900.0	8.5	$2.2 \cdot 10^{-3}$ $(0.31 \cdot M_{\rm disk,init})$	$2.8 \cdot 10^{-4}$ $(0.04 \cdot M_{\rm disk,init})$	2.35	
`LX29_nPh`					28.5	$4.8 \cdot 10^{-4}$ $(0.07 \cdot M_{\rm disk,init})$
`LX31`	40.3	9.1	$3.4 \cdot 10^{-3}$ $(0.48 \cdot M_{\rm disk,init})$	$5.6 \cdot 10^{-4}$ $(0.08 \cdot M_{\rm disk,init})$	0.75	
`LX31_nPh`					10.1	$1.9 \cdot 10^{-4}$ $(0.03 \cdot M_{\rm disk,init})$

Table 4.4: Results for simulations with different stellar (X-ray) luminosities. For the photoevaporating models, the time and location of gap creation, the total disk mass, the mass of the outer disk (outside the gap) at gap creation and the time when the accretion onto the central star stops (which approximately coincides with the time the inner boundary crosses the corotation radius) are noted. For the non-photoevaporating models, the table includes the time when the evolution becomes stationary (i.e. the accretion onto the star stops) and the remaining disk mass in the stationary state.

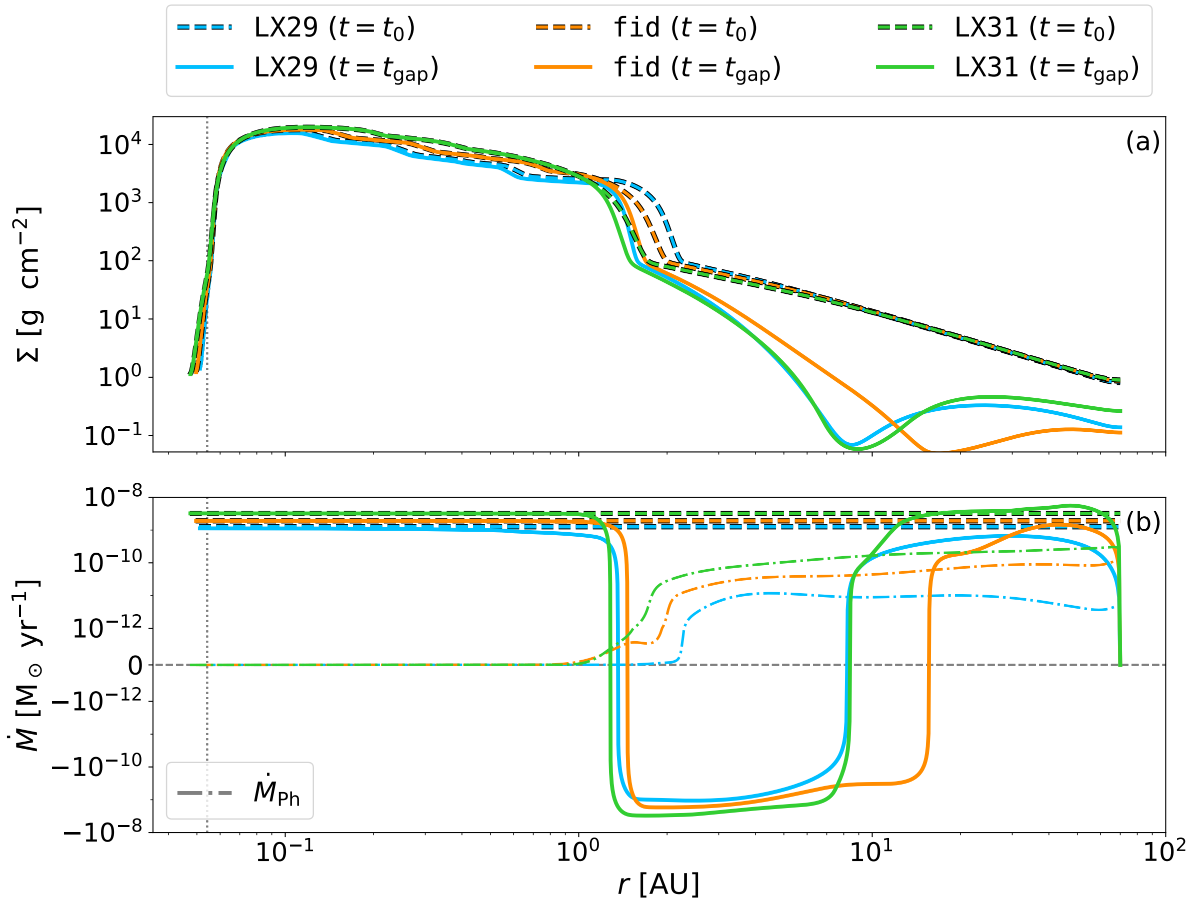

Figure 4.10: *(a)* Surface density structure and *(b)* mass flux throughout the whole disk for the three photoevaporating models with different stellar luminosities at the time a gap is created (i.e. the surface density reaches $\Sigma_{\min}$). The conditions of the respective initial model are shown as dashed, black-rimmed lines. The dash-dotted lines in *panel b* represent the initial photoevaporative mass loss rate for the corresponding model of the same color. The vertical grey dotted line and the horizontal grey dashed line mark the corotation radius and $\dot{M} = 0$, respectively.

4.2.3 Evolution with photoevaporation

As for the non-photoevaporating models, the simulations with higher stellar luminosities evolve faster than the ones with fainter stars. In addition to the stronger initial mass flux through the disk and the higher viscosity, the high luminosity models also include a much higher photoevaporative mass loss, which accelerates the evolution more than it is the case for the low luminosity simulations. The panels a-c of Fig. 4.8 show the surface density profiles at certain times for the `LX29`, `fid` and `LX31` models and in Tab. 4.4, the time and location of gap opening, the remaining disk mass and the mass of the disk outside the gap at t_{gap} are noted. While the dead zone of the `LX31` simulation has already dispersed at a time of 1 Myr, the `LX29` model has only just created a gap (after 900 kyr) and it takes an additional 3.5 Myr to lose its dead zone. The process of

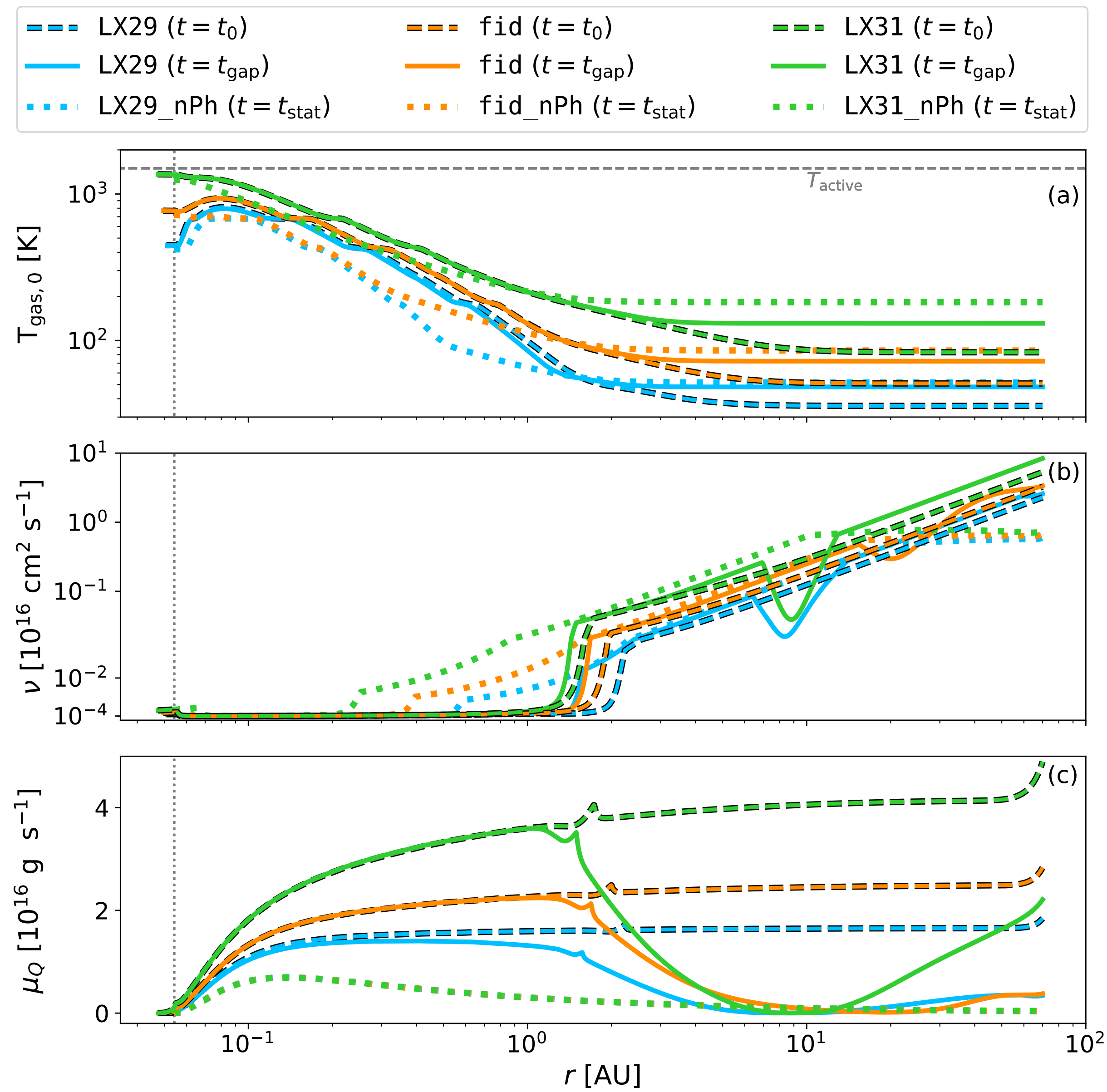

Figure 4.11: *(a)* Midplane gas temperature, *(b)* kinematic and *(c)* vertically integrated viscosity profiles for the initial model and the time of gap creation for the photoevaporating models and the stationary state for the non-photoevaporating ones. The horizontal grey dashed line in *panel a* marks the MRI activation temperature, while the vertical dotted lines signalise the position of the corotation radius. In *panel c*, the vertically integrated viscosity is the same for all three stationary states in the non-photoevaporating models and is represented by the green dotted line.

gap creation does not change in the overall picture compared to the explanation given above for the fiducial model: A mass flux inversion is first created at the outer edge of the dead zone, after which the ZRVP$_2$ starts moving outwards until it arrives at a point where enough material can be evaporated to reach $\Sigma_{\rm min}$ and create a gap fast enough before the ZRVP$_2$ is driven further outwards by the interplay between existing mass flux, the pressure gradients and the photoevaporation rate. After gap creation, the ZRVP$_2$ retreats back inwards alongside the outer edge of the inner disk. The structure of the surface density and the mass flux at the time of gap creation are depicted in Fig. 4.10. Interestingly, the gaps for the `LX29` and `LX31` models are located at very similar radii while the gap for the fiducial model lies almost twice as far away from the star ($r_{\rm gap}$ in Tab. 4.4). The reason for that can be inferred from the conditions under which gap creation is possible (see Sec. 4.1.3). Panel b of Fig. 4.10 shows the mass flux through the disk in the initial model and at the time of gap creation and the initial photoevaporation rate for all three models. Starting with comparing the `LX29` and the `fid` model, the radial profiles of the photoevaporation rates spread apart as the radius increases. While the profile of the `LX29` model reaches a maximum at around 4 AU and then declines outwards, the one for the fiducial model continues to increase on average all the way towards the outer boundary, so the ratio between the two mass loss values increases with increasing radius. This means that the flux inversion and the outward movement of the ZRVP$_2$ starts much later in the `LX29` model, not only because the absolute values of the photoevaporation rate are smaller, but also because the flux in the outer disk can be maintained for much longer due to the outwards decreasing mass loss rate. As an additional effect, the ZRVP$_2$ moves outwards at a slow rate because the inward mass flux in the outer disk can be kept up longer. Resulting from this long time the ZRVP$_2$ needs to travel away from the dead zone, the viscous mass flux and photoevaporation have already diminished the surface density in the outer disk significantly, so the point where photoevaporation at the ZRVP$_2$ can reduce the surface density to Σ_{min} and create the gap lies further inwards. So even though the initial mass flux and the viscosity (due to lower temperature, see Fig. 4.11) are lower in the `LX29` case, it is not enough to drive the ZRVP$_2$ further outwards. The reason for that is the small and radially continuously decreasing photoevaporative mass loss rate in the outer disk. In the `LX31` model, the photoevaporative mass loss rate profile behaves very similar to the one of the fiducial model but with larger absolute values. Due to the higher gas temperature and the therefore resulting higher viscosity (Fig. 4.11) compared to the other two models, the initial mass flux has to be higher (by a factor of 1.7 compared to the fiducial model) in order to achieve the same initial disk mass. The creation of the gap happens quickly (about three times as fast as in the fiducial model) while the disk mass has dropped to approximately half of its initial value (Tab. 4.4). Due to the higher (and outwards further increasing) photoevaporative mass loss rate, disk mass is removed more efficiently at the location of the ZRVP$_2$ and the refueling of material by the gas pressure gradients and viscous mass fluxes can be countered more easily, so the creation of the gap can already take place at locations where the surface density is higher compared to the models with weaker photoevaporation. The combination of the high photoevaporative mass loss and the large inward mass flux in the outer disk leads to a deeper, more pronounced gap closer to the dead zone compared to the fiducial model, as can be seen in panel a of Fig. 4.10. This also results in a more massive outer

disk (see Tab. 4.4): The outer disk of the LX31 model has twice the mass of the one of the L29 model, although the gap is at almost the same location.
The radial profiles of the kinematic viscosity, illustrated in panel b of Fig. 4.11, also show a distinct dip at the location of the gap, which follows from the decrease of α by the parameter $v(\Sigma)$ when the surface density approaches $\Sigma_{\min}$. These specific imprints do not translate directly to the profiles of the vertically integrated viscosity in panel c, since they have already been significantly decreased by the photoevaporative diminishment of the surface density.
The time of gap creation can also be seen in panel c of Fig. 4.9, where the photoevaporative mass loss rate shows a sharp bend towards smaller values. It drops steeply while the gap broadens and flattens when the outer disk is dispersed. It continues to decrease as the outer border of the inner disk is continuously driven inwards. The evolution after gap creation and outer disk dispersal behaves analogous to the fiducial model: As the mass flux in the dead zone decreases and the inner boundary approaches the corotation radius, the ZRVP_1 crosses the dead zone until the mass flux in the entire remaining disk is directed away from the star. At this point in time, the inner boundary crosses the corotation radius, the accretion rate onto the star ceases (4.9) and the remaining disk mass flows outwards, facilitated by the propeller effect, towards the region of effective photoevaporation.
This analysis of the effects of different stellar luminosity regimes shows that the qualitative overall evolution of the disk stays largely the same, but happens on different timescales (as can be inferred from Fig. 4.8 and Fig. 4.9). The comparison of the gap creation process between the three investigated photoevaporative models indicates that the location of gap creation is not merely a function of the stellar X-ray luminosity. In fact, the specific shape of the photoevaporation profiles (resulting from the difference in hardness of the used stellar X-ray luminosity spectra) and the different integrated viscosity and mass flux structures make the gap creation process a non-linear, multivariable problem.

4.3 Effects of the stellar magnetic field

As thoroughly explored in Steiner et al. (2021), the connection between the central star and its surrounding protoplanetary disk via the stellar magnetic field can have a large impact on the long-term evolution of the disk. Although the direct influences of the magnetic field are confined to the innermost parts of the disk (location of the inner boundary, propeller effect, see Sec. 3.2.5) where photoevaporation is not active, the interplay between these two effects likely has significant consequences for the whole disk, especially in the late stages of evolution (as already apparent in the analysis of the fiducial model). To investigate this matter, simulation runs with varying stellar magnetic field strengths have been conducted (including runs with no magnetic field), the parameters of which are listed in Tab. 4.5. For these runs, the stellar luminosity parameters $L_\star$, L_X, $L_\mathrm{X,soft}$ and the viscosity parameters α_MRI and α_base are kept at their fiducial values (see Tab. 4.2).

Model	$B_\star$ [kG]	$\dot{M}_\mathrm{init}$ $[M_\odot\ \mathrm{yr}^{-1}]$	Ph
`fid`	2.0	$1.90 \cdot 10^{-9}$	x
`fid_nPh`	2.0	$1.90 \cdot 10^{-9}$	
`B0`	0.0	$4.00 \cdot 10^{-9}$	x
`B0_nPh`	0.0	$4.00 \cdot 10^{-9}$	
`B1kG`	1.0	$2.02 \cdot 10^{-9}$	x
`B1kG_nPh`	1.0	$2.02 \cdot 10^{-9}$	
`B3kG`	3.0	$1.60 \cdot 10^{-9}$	x
`B3kG_nPh`	3.0	$1.60 \cdot 10^{-9}$	

Table 4.5: Run parameters for simulations with different stellar magnetic field strenghts.

4.3.1 Evolution without a stellar magnetic field

Fig. 4.12 shows the evolution of the surface density and the mass flux through the disk for the photoevaporating (panels a and b) and non-photoevaporating model (panels c and d) with no stellar magnetic field. The dashed, black-rimmed lines in Fig. 4.13 depict the time evolution of the position of the inner disk boundary, the disk mass and the accretion rate onto the central star of the same models. Since the inner disk boundary is normally set at the magnetic truncation radius (Sec. 3.2.5), it has to be set manually when no stellar magnetic field is present. For these simulations, the location of the inner disk boundary is fixed at 0.06 AU.

Regarding the non-photoevaporating model, the accretion rate onto the star does not cease (panel c in Fig. 4.13) as the disk material cannot be azimuthally accelerated at the inner boundary by the propelling effect of the stellar magnetic field. In contrast to the other non-photoevaporating models discussed in the previous sections, the simulation without a magnetic field does not reach a stationary state in which the mass flux drops to zero throughout the whole disk, but continues to accrete until the disk is completely dispersed, as can be inferred from panels c and d in Fig. 4.12. After 12.7 Myr, the maximum surface density Σ_max has dropped to 10^{-1} g cm^{-2} (which is when the disk is considered to be completely empty), while a small percentage of the initial disk mass is still present over 5 Myr later in the non-photoevaporating fiducial model (See Tab. 4.6). The comparison with the `fid_nPh` model (Sec. 4.1.1) indicates that without photoevaporation, the stellar magnetic field can indeed be responsible for retaining a

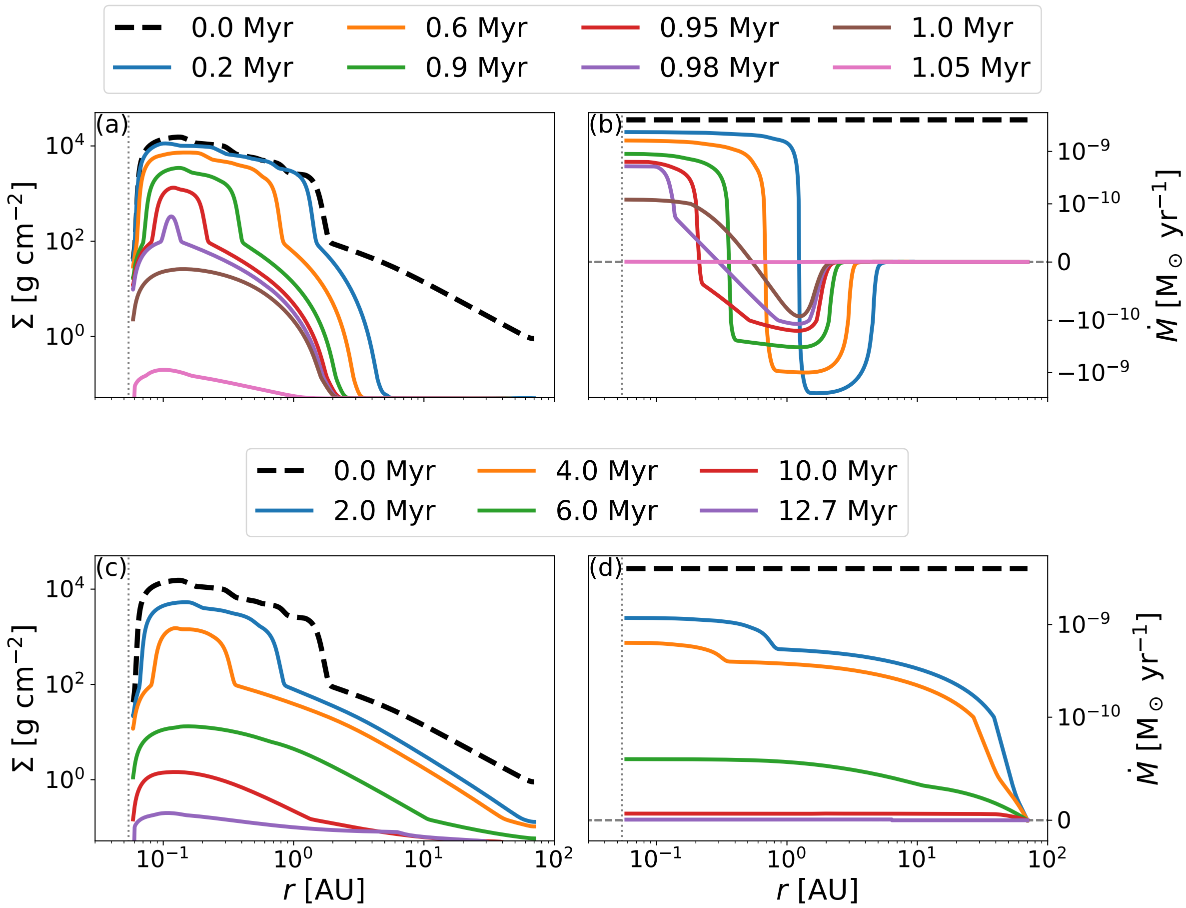

Figure 4.12: *Panels a* and *b*: Snapshots of the surface density and mass flux profiles during the evolution of the `B0` model with the black dashed line representing the initial conditions and the grey dotted line marking the corotation radius. After 1.05 Myr, the disk is completely dispersed. *Panels c* and *d*: Surface density and mass flux evolution for the non-photoevaporating model `B0_nPh`. The disk has completely vanished after 12.7 Myr.

low mass disk including a dead zone around the star (with the viscosity configuration used in these models). The photoevaporating model shows a very similar evolution to the fiducial model. Panels a and b of Fig. 4.12 show that after 0.2 Myr, the outer disk has already disappeared and the dead zone starts to shrink. The initial accretion rate for the `B0` model is more than twice as large as for the `fid` model (See Tab. 4.5), since the accretion is not hindered by the magnetic propeller effect. Therefore, the evolution of the inner disk happens on a shorter timescale: While the dead zone in the `B0` model has already disappeared after 1 Myr, the `fid` model loses its dead zone only after approximately 2 Myr. On the other hand, the differences between the two models are minimal concerning the outer disk evolution: The photoevaporative gap is created at the same location (See. Fig. 4.15) and at almost the same time with a very similar outer disk mass (Tab. 4.6). The small discrepancy in the time of gap formation can be explained by the initially larger mass flux in the `B0` model. As long as a dead zone is present, the subsequent evolution after gap creation is again very similar to the fiducial

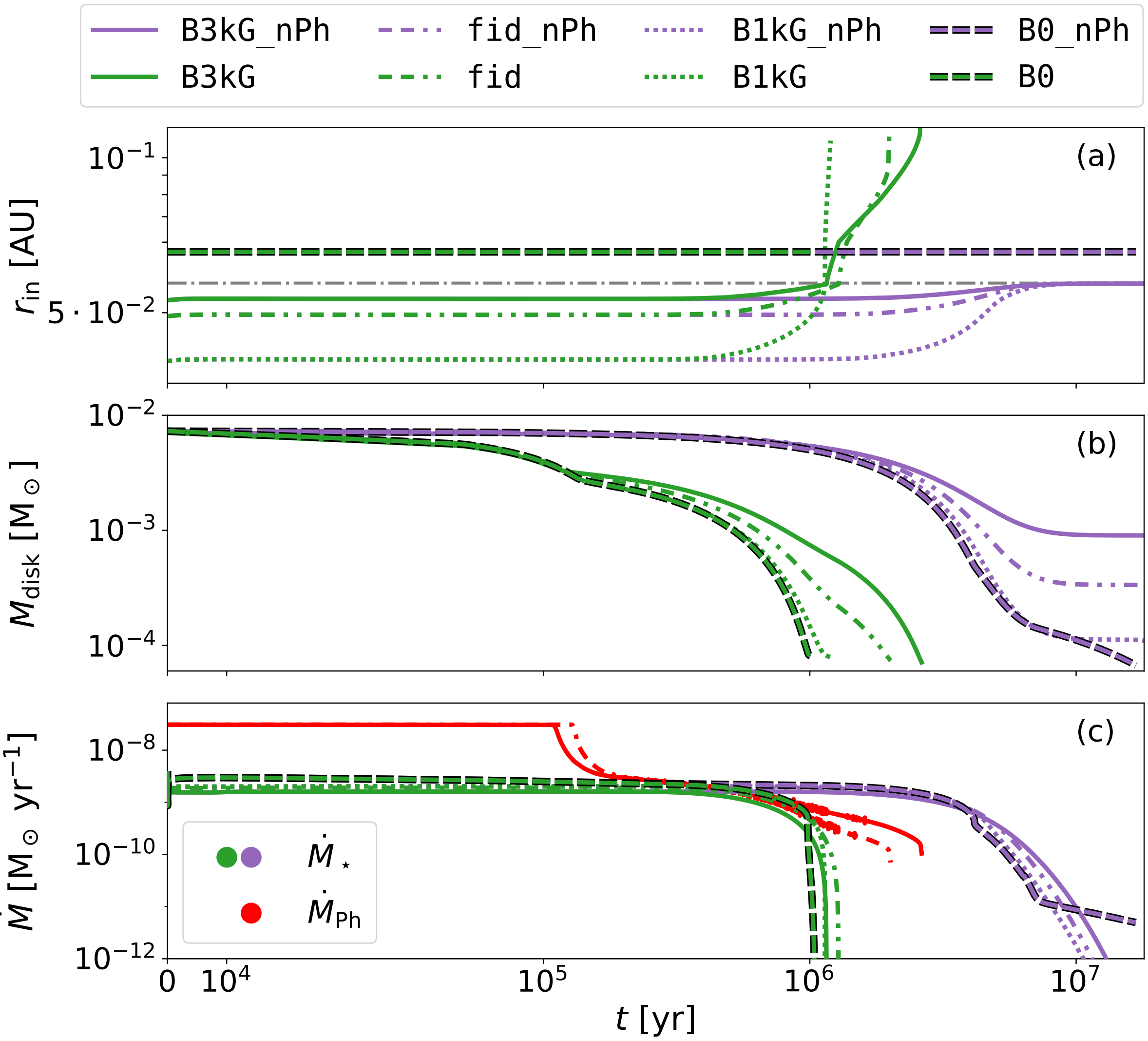

Figure 4.13: Time evolution of *(a)* the position of the inner boundary *(b)* the disk mass and *(c)* the accretion rate onto the star for the models with varying stellar magnetic field strengths. The grey dash-dotted line in *panel a* marks the position of the corotation radius. The red lines in *panel c* represent the total photoevaporative mass loss rate for the `B3kG` and the `fid` model.

model. The outer disk is photoevaporated quickly, while the ZRVP$_1$ moves inwards with the outer edge of the dead zone, which can be observed in panel b of Fig. 4.12. In the fiducial model, the stellar magnetic field provides a 'resupply' of angular momentum closely outwards of the corotation radius, which is then transported outwards by viscous friction. This allowed the ZRVP$_1$ to eventually cross the dead zone and arrive at the inner boundary. In the `B0` model, this surplus of angular momentum is missing. This means that the only mechanisms which drive the ZRVP$_1$ further inwards, is the large amount of angular momentum of the dead zone transported outwards and the large gas pressure gradient at the outer edge of the dead zone, whose location travels inwards as well as the dead zone shrinks. If the dead zone has been diminished to a significantly small size (0.98 Myr model in panels a and b of Fig. 4.12), the angular momentum arriving at the annulus at the location of the $ZRVP_1$, combined with the now small gas pressure gradient, is insufficient to overcome the viscous friction with the outer annulus. This means that the mass at the $ZRVP_1$ cannot be accelerated outwards in order for the $ZRVP_1$ to move closer to the star. The viscous friction with the outer annulus leads to an outwards angular momentum transport efficient enough to let the material flow towards the star again. Therefore, the $ZRVP_1$ is pushed outwards again and the remaining mass in the disk can accrete onto the star, unhindered by a propelling effect of a stellar magnetic field. As noted in Tab. 4.6, the disk of the `B0` model is completely dispersed after 1.04 Myr, which is considerably sooner than the fiducial model (whose accretion rate stops only after 1.28 Myr).

Model	t_{gap} [ky]	r_{gap} [AU]	$M_{\text{disk}}^{(t=t_{\text{gap}})}$ $[M_\odot]$	$M_{\text{disk,outer}}^{(t=t_{\text{gap}})}$ $[M_\odot]$	$t_{\dot{M}_\star=0}$ [Myr]	$M_{\text{disk,stat}}$ $[M_\odot]$
`fid`	130.5	16.8	$3.08 \cdot 10^{-3}$ $(0.44 \cdot M_{\text{disk,init}})$	$1.8 \cdot 10^{-4}$ $(0.03 \cdot M_{\text{disk,init}})$	1.28	
`fid_nPh`					18.4	$3.3 \cdot 10^{-4}$ $(0.05 \cdot M_{\text{disk,init}})$
`B0`	133.0	17.0	$2.86 \cdot 10^{-3}$ $(0.41 \cdot M_{\text{disk,init}})$	$2.0 \cdot 10^{-4}$ $(0.03 \cdot M_{\text{disk,init}})$	1.04	
`B0_nPh`					12.7	
`B1kG`	137.2	16.6	$2.77 \cdot 10^{-3}$ $(0.39 \cdot M_{\text{disk,init}})$	$1.8 \cdot 10^{-4}$ $(0.03 \cdot M_{\text{disk,init}})$	1.14	
`B1kG_nPh`					14.3	$1.0 \cdot 10^{-4}$ $(0.01 \cdot M_{\text{disk,init}})$
`B3kG`	114.2	18.0	$3.36 \cdot 10^{-3}$ $(0.48 \cdot M_{\text{disk,init}})$	$1.6 \cdot 10^{-4}$ $(0.02 \cdot M_{\text{disk,init}})$	1.15	
`B3kG_nPh`					20.0	$9 \cdot 10^{-4}$ $(0.13 \cdot M_{\text{disk,init}})$

Table 4.6: Same as Tab. 4.4 but for simulations with different stellar magnetic field strengths. For the `B0` and the `B0_nPh` model, $t_{\dot{M}_\star=0}$ corresponds to the time the disk is completely dissolved ($\Sigma_{\max} \leq 0.1 \text{ g cm}^{-2}$).

4.3.2 Variation of stellar magnetic field strengths

In the previous section, it was established that without a stellar magnetic field, the inner disk is completely dissolved by accretion onto the central star after the outer disk was dispersed by photoevaporation. The evolution of the fiducial model showed that with the star-disk connection via the stellar magnetic field, the accretion onto the star stops and the flux in the remaining inner disk is directed outwards towards the zone of efficient photoevaporation. As a next step, the disk evolution including different values

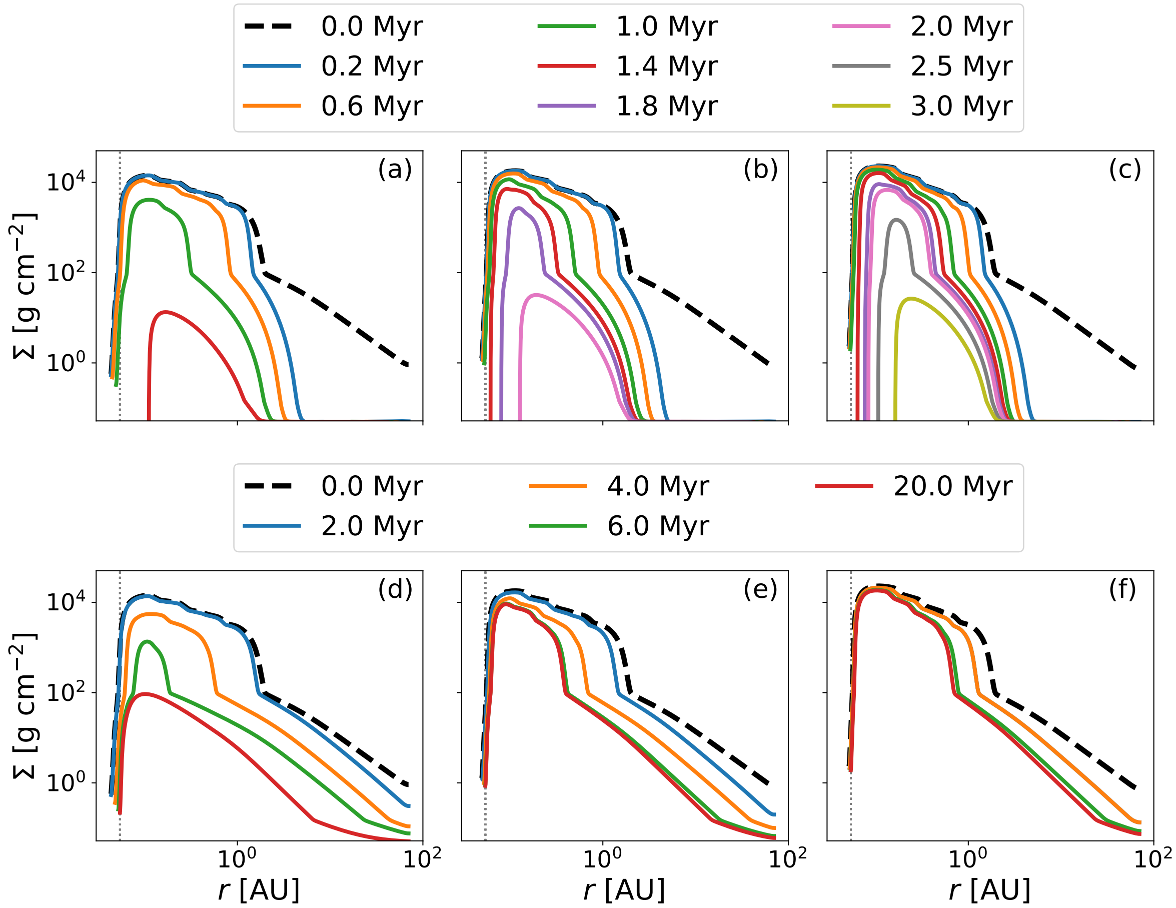

Figure 4.14: Surface density profiles of the `B1kG`, `fid` and `B3kG` models are shown in *panels a, b* and *c*, respectively, analogously the non-photoevaporative models are represented in *panels d, e* and *f* at certain times during their evolution. The black dashed lines show the corresponding initial models. The red profiles (at 20 Myr) in *panels d-f* show the stationary state of the disk. The vertical grey dotted lines mark the corotation radius.

for the strength of the stellar magnetic field is investigated. Snapshots of the surface density at certain times are depicted in Fig. 4.14 for the photoevaporating (panels a-c) and non-photoevaporating models (panels d-f) with stellar magnetic field strengths of 1 kG, 2 kG, and 3 kG. The time evolution of the location of the inner disk boundary, the disk mass and the accretion rate of these models is shown in Fig. 4.13. In the initial stationary state, the magnetic truncation radius (= inner disk boundary) is located closer to the star for smaller magnetic field strengths (panel a of Fig. 4.13) due to the weaker magnetic pressure. Due to the larger area between $r_{\rm in}$ and $r_{\rm cor}$, within which the angular velocity of the disk material is reduced by the magnetic torque, combined with a weaker propelling effect outside the corotation radius, the initial accretion rate is higher for models with weaker stellar magnetic field strengths, as noted in Tab. 4.5.

Starting with the non-photoevaporating models, panels d-f of Fig. 4.14 show that a stationary state is reached for all three models, when the inner boundary reaches the corotation radius and the accretion onto the star stops due to the propeller effect. The movement of the inner boundary is depicted in panel a of Fig. 4.13 and the times when the accretion ceases are noted in Tab. 4.6. After around 2 Myr, the accretion rate starts to drop significantly for all three models, but the decrease is stronger for models with weaker magnetic fields, because more mass has already been lost due to the initially higher accretion rate. This leads to a faster movement of the inner disk boundary towards the corotation radius and the accretion stops sooner. Although the `B3kG_nPh` model starts with its inner rim closest to the corotation radius, its accretion ceases only after 20 Myr, while the models with weaker fields reach this point in time earlier (see Tab. 4.6). Since the higher magnetic pressure of the stronger magnetic field models can withstand the ram pressure of the accreting material much easier, the inner boundary reaches the corotation radius (and the accretion ceases) when the disk mass is still high. This leads to the result that the stationary state of the disk of the `B3kG_nPh` model retains approximately 13% of the initial disk mass, while <1% remain in the `B1kG_nPh` model, in which the ram pressure stays strong enough for accretion until the dead zone has vanished (panel d in Fig. 4.14).

The timescales for the evolution of the photoevaporating models can be gauged from panels a-c of Fig. 4.13 and Fig. 4.14. After 0.2 Myr, the outer disk has already dispersed in all three models. As already noticed in the the `B0` model, the strength of the stellar magnetic field does not have a significant influence on the evolution of the outer disk. Fig. 4.15 shows the surface density and the mass flux at the time of gap creation and offers a direct comparison of the initial, stationary models. The location of the gap is almost equal for all models (within a small margin) with very similar outer disk masses as noted in Tab. 4.6. The gap opens sooner for models with higher magnetic field strengths due to the lower initial accretion rate throughout the whole disk[6] (which is why the disk mass is higher at the time of gap creation). Following this reasoning, one would expect, that the gap in the `B0` model is opened at a later point in time than in the models including a magnetic field due to the initially higher mass flux. But judging from panel c of Fig. 4.13, the accretion rate in the `B0` model starts to decrease immediately at the beginning, while it stays constant for the magnetic field models (noticeable by the gradual approach of the black-rimmed green line towards the other green lines over the course of the first Myr in panel c of Fig. 4.13). This is a consequence of the fact that without a magnetic field, the accretion onto the star is determined by the viscous angular momentum transport and the gas pressure gradient alone, while the magnetic torque 'regulates' the accretion by braking and accelerating the disk material inside and outside the corotation radius, respectively. As a result, the `B0` model reaches a mass flux profile with low enough values for gap creation sooner than would be expected for such a high accretion rate in the initial, stationary model. The time of gap creation is also visible in panel c of Fig. 4.13 where the photoevaporation rate shows a sharp

[6]The lower the initial mass flux in the outer disk is, the sooner photoevaporation can reduce it to 0 and create the flux inversion, after which the $ZRVP_2$ moves outwards and the gap is created.

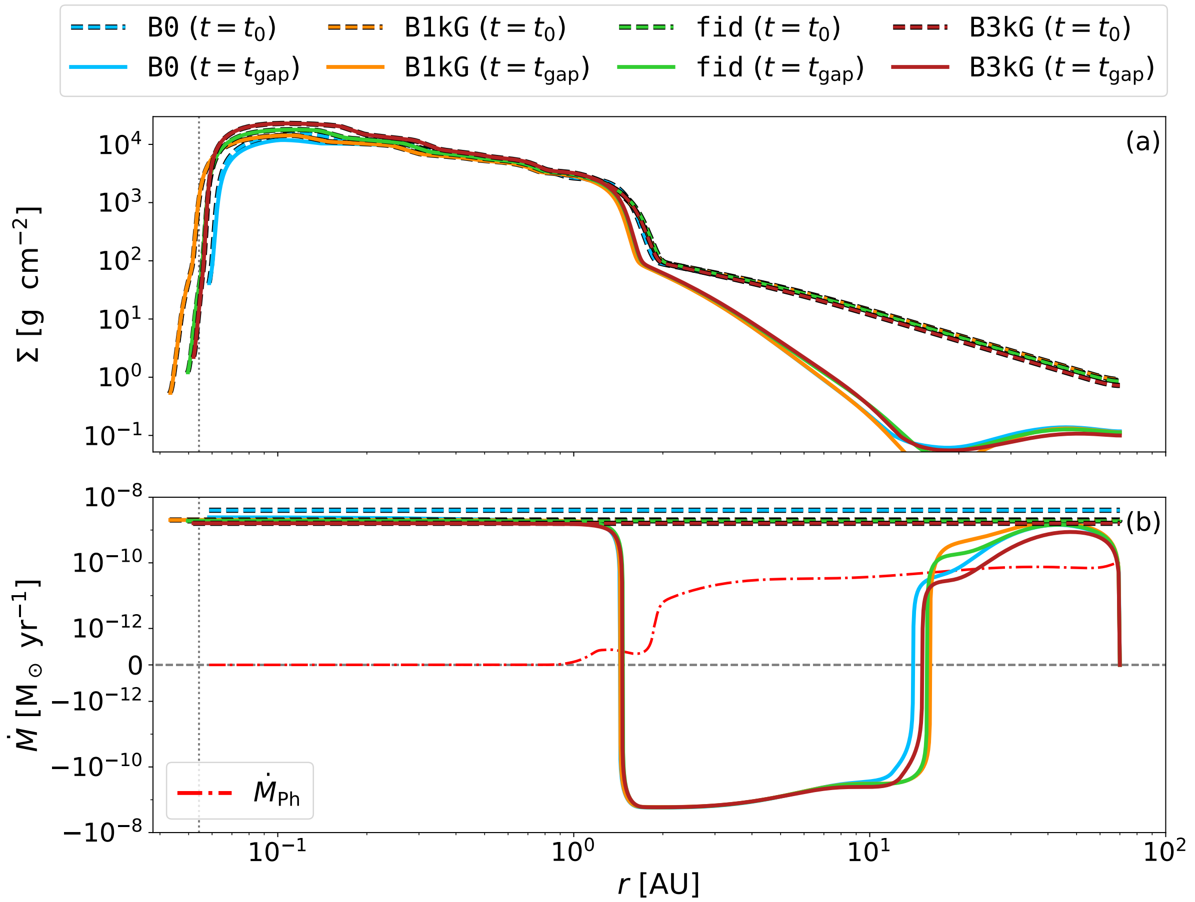

Figure 4.15: *(a)* Surface density and *(b)* mass flux profiles of the photoevaporating models with varying stellar magnetic field strengths at the initial configurations (black-rimmed dashed lines) and at the time of gap creation. The red dash-dotted line in *panel b* shows the photoevaporation rate, which is equivalent for all four models. The horizontal grey dashed line marks $\dot{M} = 0$ and the vertical dotted line indicates the corotation radius.

bend after which it approaches the values of the accretion rates. In order to preserve clarity, only the photoevaporation rates of the `B3kG` and `fid` model are shown. After the gap is created and the outer disk is evaporated, the evolutionary tracks of the disk masses start to diverge (panel b of Fig. 4.13) due to the accretion becoming dominant as the photoevaporation rate drops. The disk mass for models with higher magnetic field strengths stays larger due to the less efficient accretion. Meanwhile, the inner disk boundary starts to approach the corotation radius in a similar manner as in the non-photoevaporating models. The velocity of the movement of the inner boundary is smaller for models with higher magnetic field strengths, because the ram pressure of the accreting material decreases only slowly due to the larger density (and larger dead zone) in the inner disk and the smaller accretion rate at the time the magnetic pressure starts pushing the inner boundary outwards. The corotation radius is reached at very similar times in all three models, as is evident in panel a of Fig. 4.13. After the inner boundary has moved beyond the corotation radius and the accretion rate onto the star has stopped, the subsequent movement is determined by the gas pressure, which decreases slower for models with stronger magnetic fields due to the more massive remaining inner disk. Fig. 4.16 shows the surface density (panel a), the mass flux (panel b) and the discrepancy between the azimuthal velocity and the Keplerian velocity (panel c) at the time when the inner boundary is located at the corotation radius and at a time when the inner boundary moved a certain distance beyond the corotation radius. As mentioned above, panel a illustrates that the inner disk is more massive and still retains a significant dead zone for models with stronger magnetic fields. The inset in panel a shows, that the density in the innermost region is approximately 6 times larger in the `fid` model than in the `B1kG` model, while it is twice as large for the `B3kG` model compared to `fid`. These ratios are the same for both depicted points in time whereas the absolute values decrease.

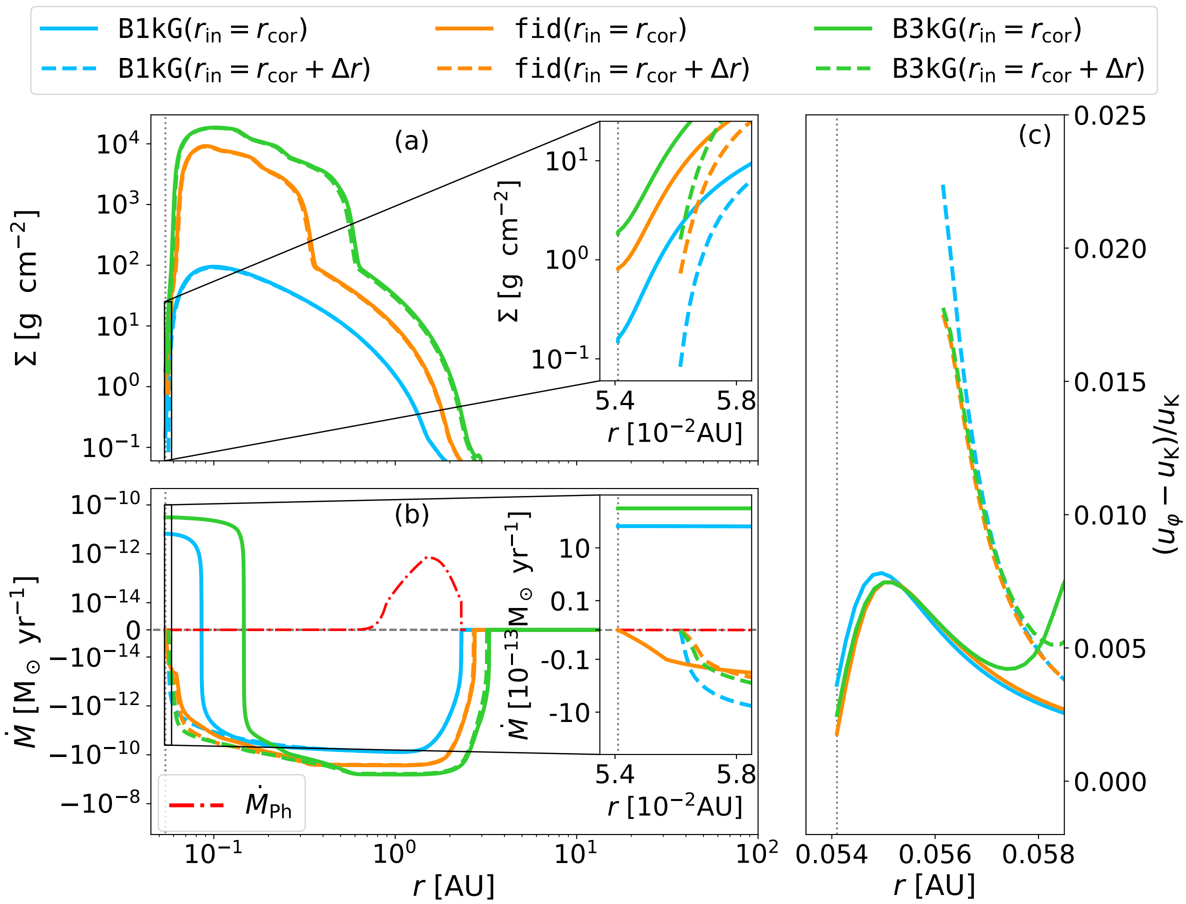

Figure 4.16: *(a)* Surface density, *(b)* mass flux and *(c)* deviation from Keplerian angular velocity at the inner boundary for the three models with different stellar magnetic field strengths. The respective radial profiles are shown at times when the inner boundary is located at the corotation radius ($r_{\rm in} = r_{\rm cor}$), which is marked with the vertical grey dotted line, and when it just crossed the corotation radius ($r_{\rm in} = r_{\rm cor} + \Delta r$). The insets in *panels a* and *b* show the surface density and the mass flux, respectively, at the inner boundary. The red dash-dotted line in *panel b* shows the photoevaporation rate for the `B1kG` model at the time when $r_{\rm in} = r_{\rm cor}$.

Panel b shows that the moment the inner boundary reaches the corotation radius is not necessarily exactly contemporaneous with the moment the accretion onto the star stops. As already explained in the context of the fiducial model, the ZRVP_1 moves inwards alongside the outer edge of the dead zone until the angular momentum induced by the magnetic torque in the inner disk is enough to overcome the large vertically integrated viscosity in the dead zone and let the ZRVP_1 cross the dead zone towards the inner boundary. In the `B3kG` model, the integrated viscosity is still large enough to counteract the strong stellar magnetic torque at the inner boundary in order to maintain an accretion flow onto the star. The same principle applies to the `B1kG` model, but in this case, the magnetic field is weak enough to allow an accretion flow although the dead zone has already vanished and the integrated viscosity is correspondingly low. In the `fid` model, the disk configuration interacts with the magnetic field in a way that the magnetic torque at the inner boundary (at the corotation radius) is large enough to counteract the viscous accretion and let the ZRVP_1 arrive at the inner boundary. Panel c shows that the differences in angular velocity in the vicinity of the corotation radius at the time of $r_{\mathrm{in}} = r_{\mathrm{cor}}$ are minimal. That being said, the difference between the point in time when the inner boundary reaches the corotation radius and the time the accretion onto the star stops (as noted in Tab. 4.6) is small (< 2 kyr). After the inner boundary crossed the corotation radius, the mass flux is directed outwards for all three models. When observing the azimuthal velocity, the propelling effect of the magnetic field is clearly visible at this point in time (see Sec. 4.1.4). The values for the `fid` and `B3kG` model are congruent at the inner rim, while the `B1kG` model shows a larger velocity. The small difference in density and therefore integrated viscosity between the `fid` and `B3kG` models can be compensated by the difference in the strength of the magnetic torque. But since the integrated viscosity is around six times smaller in the `B1kG` model compared to `fid`, the (by a factor of 2) weaker magnetic field is strong enough to accelerate the disk material at the inner boundary to larger values. This difference in angular velocity can also be inferred from the inset in panel b, where the outward flux is larger in the `B1kG` model than in the other two models. The mass of the remaining disks subsequently flows outwards, fueled by the propeller effect, towards the photoevaporation regime, illustrated as the red, dash-dotted line in panel b. As a result this process, the `B3kG` model loses its dead zone only after 3 Myr, as can be inferred from Fig. 4.14.

4.4 Influence of different viscosity parameters

In Sec. 4.1.3 and subsequent sections, it was stated that the gap creation process depends on the interplay between the photoevaporative mass loss rate and the mass flux through the disk. Since the mass flux in protoplanetary disks is predominantly determined by the viscosity (especially in the outer parts of the disk where the gap is created), the variation of the parameters describing the viscosity in the simulations is investigated. Sec. 3.2.2 shows that the viscosity is compounded by the parameters α_{base} and α_{MRI}, which describe the base viscosity anywhere in the disk and the viscosity of the MRI active regions, respectively. Depending on the surface density and the gas temperature, three different configurations at a certain radius point are possible, which are listed in Tab. 3.2 together with the corresponding conditions.

4.4.1 Viscosity of the MRI-active regions

Model	α_{MRI}	$\dot{M}_{\mathrm{init}}$ $[M_\odot\ \mathrm{yr}^{-1}]$	Ph
`fid`	$5 \cdot 10^{-3}$	$1.90 \cdot 10^{-9}$	x
`fid_nPh`	$5 \cdot 10^{-3}$	$1.90 \cdot 10^{-9}$	
`alM3em2`	$3 \cdot 10^{-2}$	$1.20 \cdot 10^{-8}$	x
`alM3em2_nPh`	$3 \cdot 10^{-2}$	$1.20 \cdot 10^{-8}$	
`alM1em3`	$1 \cdot 10^{-3}$	$0.40 \cdot 10^{-9}$	x
`alM1em3_nPh`	$1 \cdot 10^{-3}$	$0.40 \cdot 10^{-9}$	

Table 4.7: Run parameters for simulations with different values of α_{MRI}.

Tab. 4.7 shows the parameters chosen for the simulations illustrating the effects of different values of α_{MRI}. The stellar parameters $L_\star$, L_{X}, $L_{\mathrm{X,soft}}$, $B_\star$ and the base viscosity α_{base} are kept at their fiducial values (see Tab. 4.2). Once again, every simulation run was conducted with and without the influence of photoevaporation. In order to reach an initial, stationary state which results in the same disk mass of 0.07 $M_\odot$ for all these models, the initial mass flux through the disk (and therefore the accretion rate onto the star) has to be adapted. A larger MRI-viscosity hereby requires a larger flux due to the enhanced angular momentum transport. In this case, the `alM3em2` and `alM3em2_nPh` models with $\alpha_{\mathrm{MRI}} = 3 \cdot 10^{-2}$ inherit a constant initial mass flux which is over six times larger than the one in the initial stationary state of the `fid` model. The time evolution of the location of the inner boundary, the disk mass and the accretion rate together with the photoevaporation rate is shown in Fig. 4.17 for all models listed in Tab. 4.7. The `alM3em2` and `alM3em2_nPh` models develop accretion outbursts, which means the gas temperature in the inner parts of the disk rises above the MRI activation temperature T_{active}. At the radial points where this is the case, the viscosity is described by configuration 2 in Tab. 3.2, regardless of the value of the surface density. The burst mechanism and structure, described by Bell & Lin (1994), was thoroughly explored in the context of TAPIR-simulations by Steiner et al. (2021) and will not be investigated again in detail in this thesis. In Fig. 4.18, snapshots of the surface density during time integration for all six models noted in Tab. 4.7 are shown, where simulations with comparable evolutionary timescales share the same row.

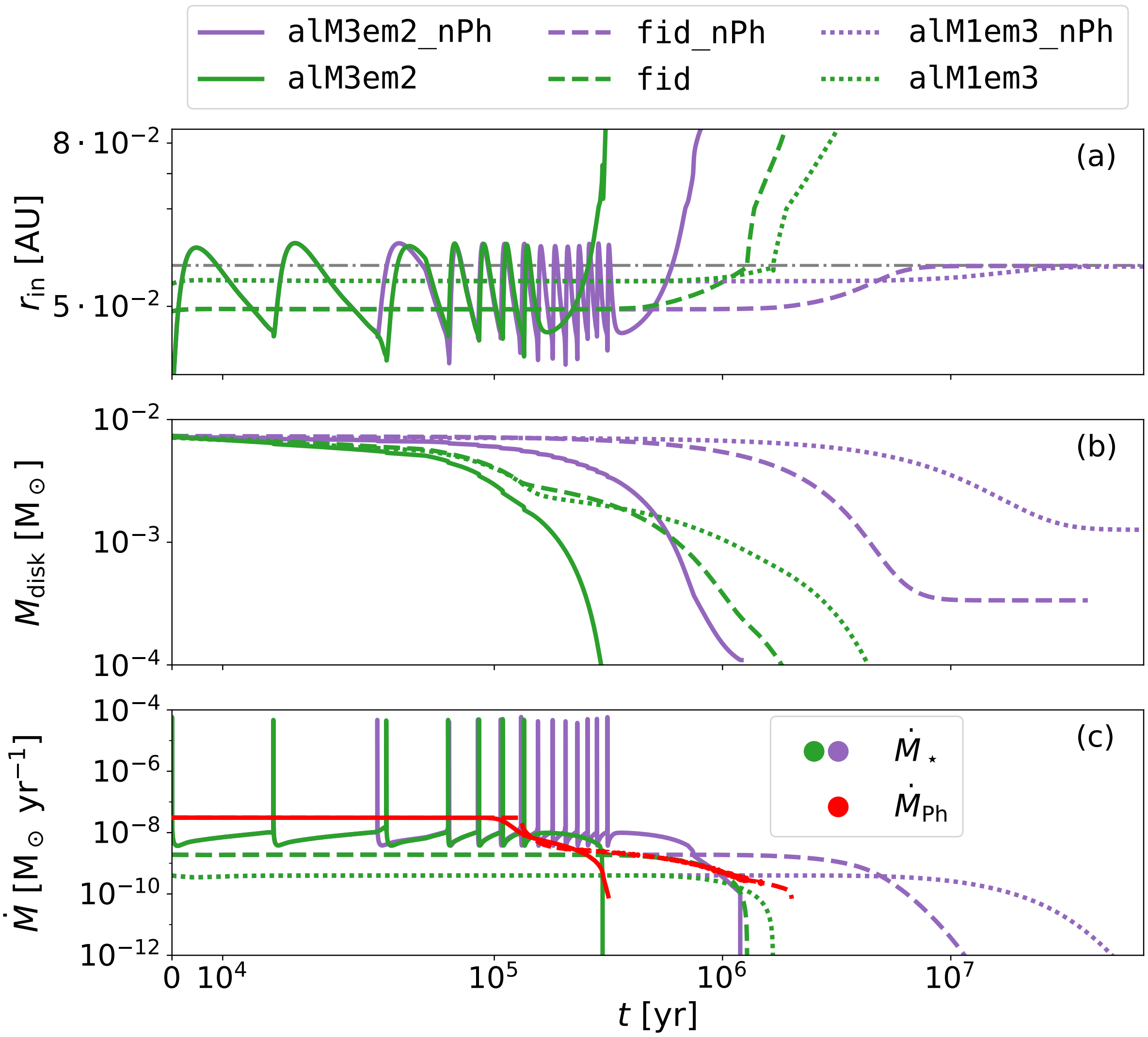

Figure 4.17: Time evolution of *(a)* the location of the inner disk boundary, *(b)* the disk mass and *(c)* the accretion rate onto the star for the three models with different values of the $\alpha_{\rm MRI}$ parameter. The models with $\alpha_{\rm MRI} = 3 \cdot 10^{-2}$ show an outburst behaviour. The horizontal grey dash-dotted line in *panel a* marks the position of the corotation radius. The red lines in *panel c* indicate the total photoevaporative mass loss rate for the `alM3em2` and the `fid` model.

Low viscosity case: $\alpha_{\rm MRI} = 0.001$

Compared to the fiducial model, a lower viscosity results in a slower evolution due to the small mass flux through the disk. Panel f of Fig. 4.18 indicates that the stationary state of the non-photoevaporating model is reached only after 50 Myr with a remaining mass of 18% of the initial mass, as noted in Tab. 4.8. From panel a of Fig. 4.17, it can be inferred that the inner boundary in the low-viscosity models is already located close to the corotation radius owing to the small ram pressure of the accreting material. The

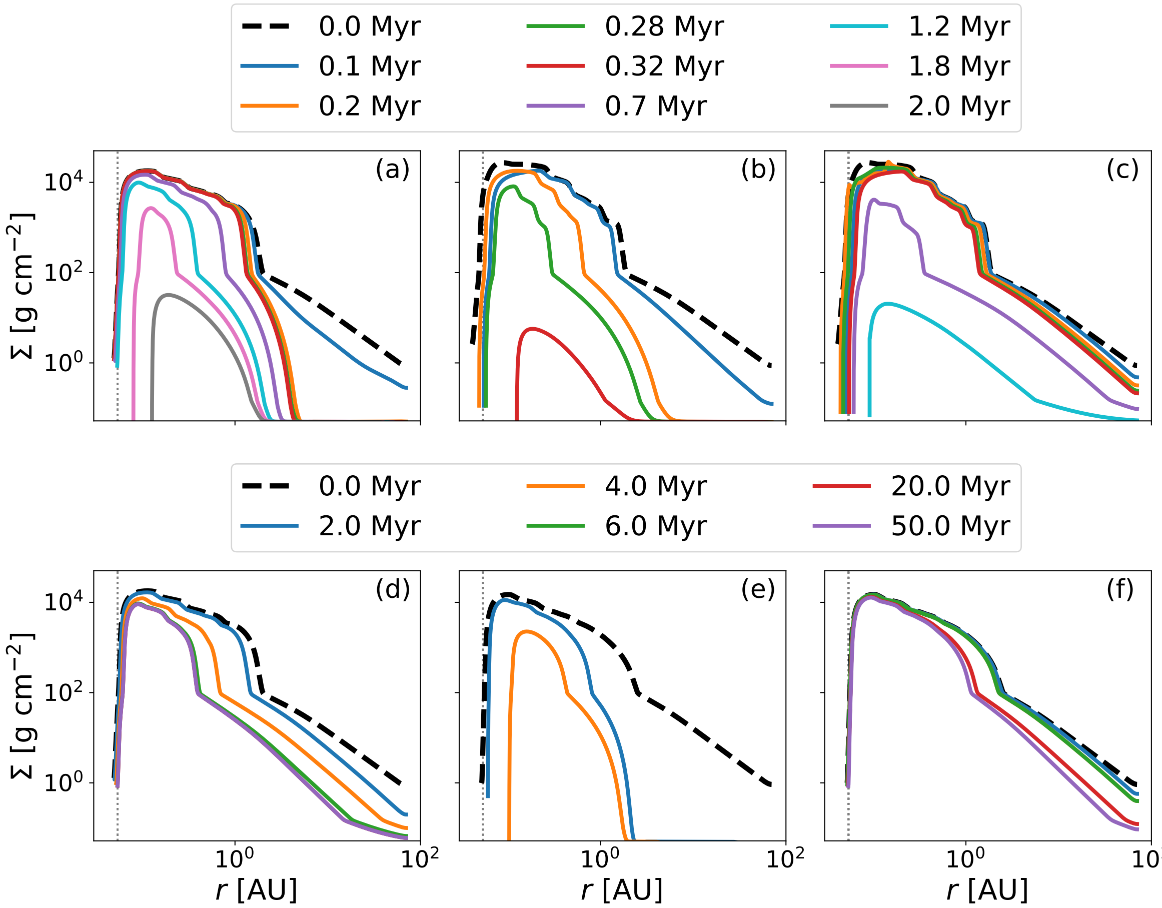

Figure 4.18: Evolution of the surface density profiles of the photoevaporating and non-photoevaporating models with varying values of α_{MRI}. Since the `alM3em2_nPh` model evolves on similar timescales as the photoevaporating simulations (see Fig. 4.17), the panels show the following models: *(a)* `fid`, *(b)* `alM3em2`, *(c)* `alM3em2_nPh`, *(d)* `fid_nPh`, *(e)* `alM1em3`, *(f)* `alM1em3_nPh`. The black dashed lines depict the initial, stationary configuration and the vertical grey dotted line marks the corotation radius.

small vertically integrated viscosity enables the magnetic pressure to push the inner rim further outwards while the disk mass is still high. When the corotation radius is reached, the propelling effect of the stellar magnetic field is strong enough to prevent this substantial amount of mass from accreting onto the star.

Panel e of Fig. 4.18 illustrates that the photoevaporating model has still not lost its dead zone after 4 Myr, but the time of gap creation is not much different compared to the fiducial model (see Tab. 4.8). Fig. 4.19 shows the evolution of the surface density and the mass flux of the `alM1em3` model in the time frame within which a gap is carved in the outer disk and expanded towards the dead zone. Similar to the fiducial model, panel b illustrates that a flux inversion is created at the outer edge of the dead zone as soon as the mass flux from the outer disk has decreased enough to be completely evaporated before reaching the dead zone. This point in time occurs sooner than in

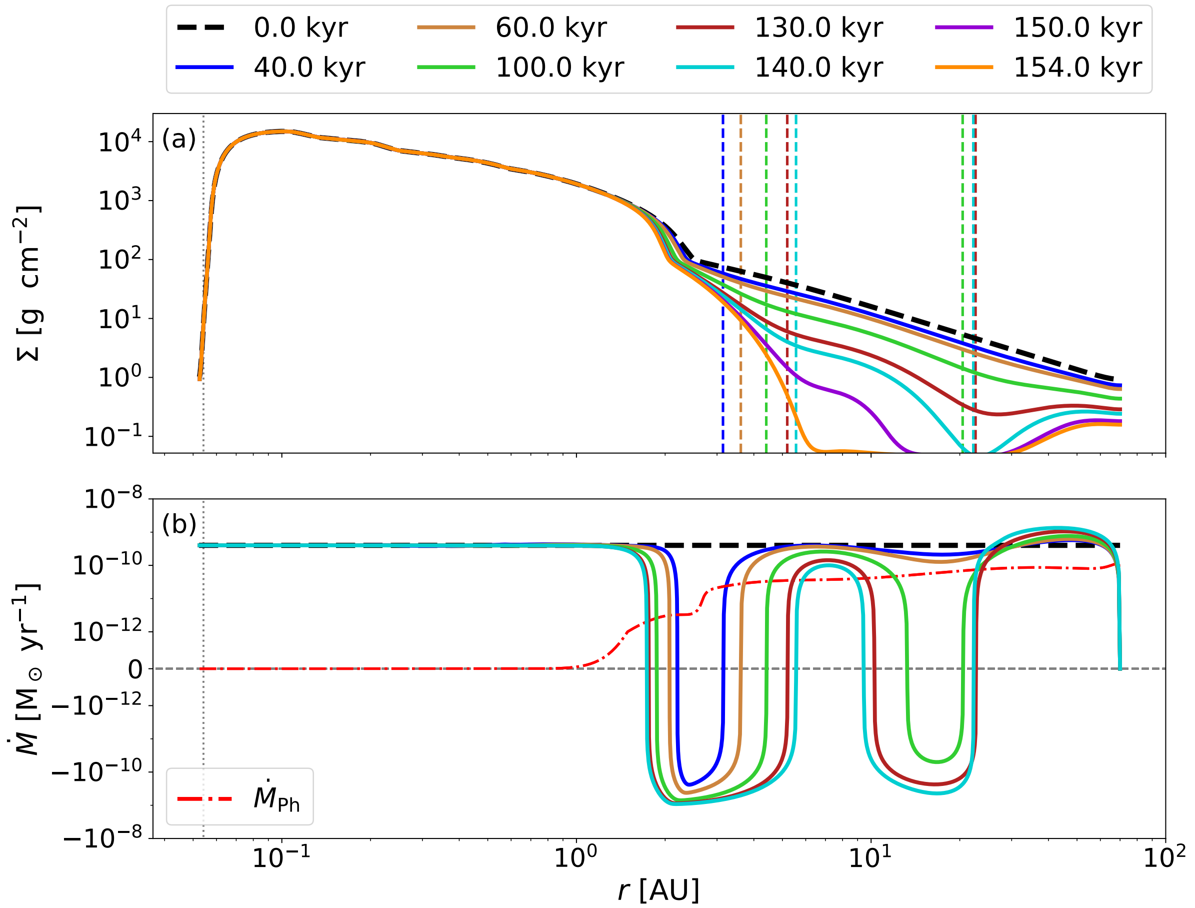

Figure 4.19: Evolution of *(a)* the surface density and *(b)* the mass flux during gap creation in the `alM1em3` model. The vertical dashed lines in *panel a* indicate the positions of the $ZRVP_2$s, where the mass flux changes from an outwards to an inwards flow. The red dash-dotted line in *panel b* shows the initial photoevaporation rate and the vertical grey dotted line marks the corotation radius. The mass flux profiles of the simulation at 150 kyr and 154 kyr have been omitted for clarity.

the fiducial model due to the lower initial mass flux. At a time of 60 kyr, the model shows that the $ZRVP_2$ (which is also indicated in panel a by the vertical dashed lines) travels outwards, but at the same time, a dip in the mass flux profile can be observed at around 17 AU. The same phenomenon can also be seen in the evolution of the fiducial model at a later time (Fig. 4.3, mass flux profile at 115 kyr). The presence of this dip is owed to the angular momentum transported outwards from the inflowing material outside the $ZRVP_2$. Due to the low viscosity, the angular momentum cannot be passed on fast enough, before photoevaporation can take away a significant amount of material from the slower flow. The flux at this location drops further until it becomes smaller than the photoevaporation rate and a second flux inversion is created with a respective $ZRVP_1$ and $ZRVP_2$. The locations of the now two $ZRVP_2$s is marked in panel a by the vertical dashed lines of the same color as the corresponding surface density profile. The still present inwards mass flux between the two regions of inverted flux is continuously diminished by photoevaporation, which causes the inner ZRVP_2 to move further outwards. Meanwhile, the outer ZRVP_2 stays approximately at the location of its initial creation due to the high mass flux in the outer disk and enables photoevaporation to efficiently remove mass in its vicinity. This results in a deeper gap compared to the fiducial model since the surface density in the outer disk is still high at this point in time. During the creation of the second flux inversion, the inward mass flux in the outer disk continuously increases because less angular momentum is transported outwards from the area where the mass flux profile starts to dip down. The same process happens outside the first ZRVP_2, which is why at 8 AU the flux does not decrease significantly from the initial value until the second flux inversion is created. The surface density profiles after 130 kyr and 140 kyr in panel a of Fig. 4.19 show that at the location of the inner ZRVP_2 mass is efficiently removed as well, discernible by the reduction of the absolute radial surface density gradient, indicating the creation of a second gap. But the disk mass is already removed from outside-in by the already present gap before a identifiable second gap can be created. In panel b, the mass flux profiles of the 150 kyr and 154 kyr models have been omitted for clarity, because the density of $\Sigma_{\min}$ in the gap and the consequent reduction of viscosity and photoevaporation rate in this region cause disturbances in the mass flux that would obscure the relevant processes depicted in Fig. 4.19.

Model	t_{gap} [ky]	r_{gap} [AU]	$M_{\text{disk}}^{(t=t_{\text{gap}})}$ $[M_\odot]$	$M_{\text{disk,outer}}^{(t=t_{\text{gap}})}$ $[M_\odot]$	$t_{\dot{M}_\star=0}$ [Myr]	$M_{\text{disk,stat}}$ $[M_\odot]$
`fid`	130.5	16.8	$3.08 \cdot 10^{-3}$ $(0.44 \cdot M_{\text{disk,init}})$	$1.8 \cdot 10^{-4}$ $(0.03 \cdot M_{\text{disk,init}})$	1.28	
`fid_nPh`					18.4	$3.3 \cdot 10^{-4}$ $(0.05 \cdot M_{\text{disk,init}})$
`alM1em3`	139.1	23.5	$2.79 \cdot 10^{-3}$ $(0.40 \cdot M_{\text{disk,init}})$	$3.4 \cdot 10^{-4}$ $(0.05 \cdot M_{\text{disk,init}})$	1.67	
`alM1em3_nPh`					50	$1.3 \cdot 10^{-3}$ $(0.18 \cdot M_{\text{disk,init}})$

Table 4.8: Results for the simulations `alM1em3` and `alM1em3_nPh` with a small value for the viscosity of the MRI-active regions α_{MRI} of 10^{-3} compared to the fiducial model. The noted quantities are the same as in Tab. 4.4.

The question occurs why a gap is not created at the location of the ZRVP_1 as well. Fig. 4.19 shows that the reduction of mass in the area around the outer ZRVP_1 is less efficient than at the ZRVP_2, even though the photoevaporative mass loss rate is almost the same. This difference can be understood in the following way: The ZRVP_2 is a location in the disk towards which the mass flux is directed from both inside and outside. But the flux is diminished from both sides by photoevaporation before reaching this point. This is not the case for the ZRVP_1 because at this point, the mass flux vanishes due to angular momentum being transported outwards from the regions inside the ZRVP_1. This occurs because no mass flux, to which the angular momentum can be transferred to, is flowing towards this point from the outside, which results from the quenching by photoevaporation. This means that the mass which reached this point just before the mass flux is cut off by photoevaporation is stopped and the radial velocity of the material in the inner neighbouring annuli is reduced. If photoevaporation now reduces the density at the ZRVP_1, the material at this point is accelerated outwards by the angular momentum coming from the inner parts of the disk, leading to a continuous inward movement of the ZRVP_1. This prevents the photoevaporation from efficiently locally reducing the surface density at the ZRVP_1.

After the disk is separated into two parts by the gap, the outer disk (which holds 5% of the initial disk mass, see Tab. 4.8) continues to keep up an inward mass flux while being evaporated. After 1.67 Myr, the inner disk boundary reaches the corotation radius and the accretion onto the star ceases. As in the fiducial model, this is followed by an outward mass flux throughout the whole disk while the inner boundary continues to be pushed away from the star. Panel e of Fig. 4.18 shows the surface density profile at 4 Myr after which the simulation had to be terminated due to numerical problems (See Sec. 5).

High viscosity case: $\alpha_{\mathrm{MRI}} = 0.03$

The likelihood of the occurrence of thermal instability-triggered episodic accretion events ultimately depends on the mechanisms which can be responsible for raising the temperature in the dead zone above the MRI-activation temperature. An important factor in this regard is the viscous heating inside the dead zone, which is primarily determined by the chosen description of α. The ratio between the parameters α_{MRI} and α_{base} is responsible for the amount of piled up material in the dead zone, where a large ratio leads to an increased surface density. This is because a higher ratio results in a larger relative difference between α in the dead zone (described by configuration 1 in Tab. 3.2) and in the outer disk (configuration 2), which consequently leads to a larger difference in surface density between these two regions in the initial stationary state. This can be observed in Fig. 4.22 (and even better in Fig. 4.26 in Sec. 4.4.2) when comparing the initial, stationary models. The higher surface density results in a larger vertically integrated viscosity, enhancing viscous heating. Another important factor is the initial disk mass: A massive disk can easily aggregate enough mass in the inner disk to trigger the thermal instability, whereas a low-mass disk can fail to do so, even if the viscosity and the ratio between α_{MRI} and α_{base} is high. Since the simulations in this thesis are conducted with a low-mass disk, the $\alpha_{\mathrm{MRI}}/\alpha_{\mathrm{base}}$ ratio of 50 and the value of α itself was too small to cause episodic accretion in the models explored so far. In the `alM3em2` and `al3em2_nPh` models, not only was the ratio between α_{MRI} and α_{base} increased compared to the fiducial model (from 50 to 300), but this increase was achieved by raising α_{MRI} to a higher value, which also facilitates viscous heating. This suffices to trigger thermal instability-induced accretion outbursts despite the rather low disk mass.

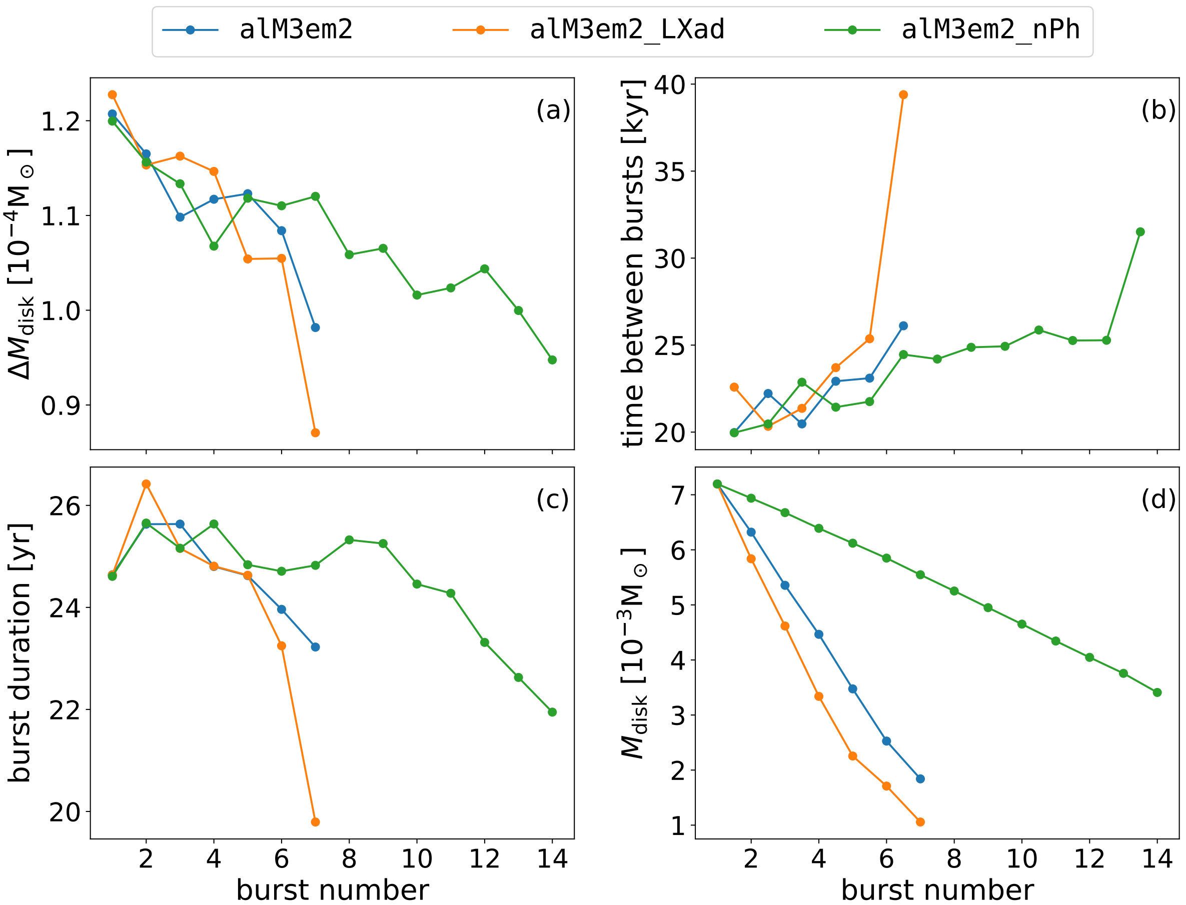

Figure 4.20: Analysis of the episodic accretion events occurring in the photoevaporating and non-photoevaporating model with $\alpha_{\mathrm{MRI}} = 3 \cdot 10^{-2}$. *Panel a*: lost disk mass during a burst (which includes the photoevaporative mass loss in the `alM3em2` model). *Panel b*: duration of the quiescent state between bursts. *Panel c*: duration of a burst. *Panel d*: disk mass at the end of a burst.

The outburst behaviour combined with the high viscosity leads to a much faster evolution for the `alM3em2_nPh` model compared to other simulations without photoevaporation. A total of 14 episodic accretion events occur during the time between the start of the simulation and the beginning of the quiescent state after 313 kyr, as noted in Tab. 4.9. Up to this point, the disk has already lost 50% of its initial mass. During a burst, amounts of mass of the order of 10^{-4} M$_\odot$ are accreted onto the star over a time period

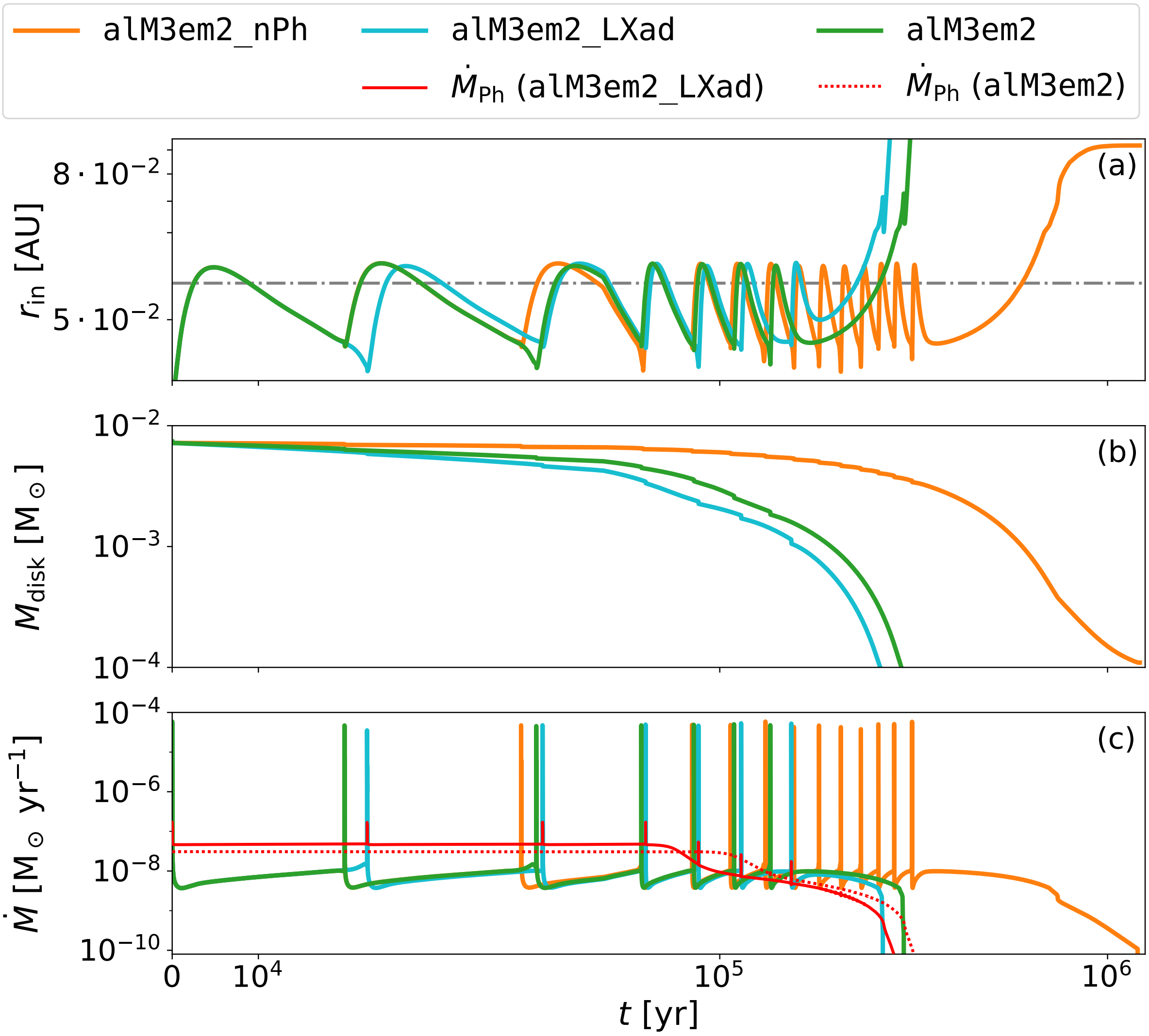

Figure 4.21: Same as Fig. 4.17, but just for the bursting models `alM3em2`, `alM3em2_nPh` and with the model considering the accretion luminosity for the evaluation of the photoevaporative mass loss `alM3em2_LXad`.

of less than 30 yr, as depicted in panels a and c in Fig. 4.20. The corresponding spikes in the accretion rate can be observed in panel c of Fig. 4.17. As explored in Steiner et al. (2021), the inner boundary of the disk responds to these events by adapting to the ram pressure of the inflowing material. Panel a of Fig. 4.17 shows the movement of the inner boundary, which may not be accurate according to the descriptions given in Steiner et al. (2021) due to extreme peak accretion rate during a burst (see Sec. 5).

After 1.20 Myr, the accretion rate onto the star stops in the non-photoevaporating model. It can be inferred from Fig. 4.17 and panel c of Fig. 4.18 that at this point in time the inner disk boundary has moved well beyond the corotation radius. This is because the magnetic torque is not strong enough to stop the accretion sooner, which results from high viscosity. Only when the disk mass has dropped to values low enough and the radius of the inner boundary is at a location where the propelling effect of the stellar

Model	# bursts	t_{quies} [kyr]	$M_{\text{disk}}^{(t=t_{\text{quies}})}$ $[M_\odot]$	$t_{\dot{M}_\star=0}$ [Myr]
alM3em2	7	135.0	$1.8 \cdot 10^{-3}$ $(0.26 \cdot M_{\text{disk,init}})$	0.30
alM3em2_LXad	7	152.8	$1.05 \cdot 10^{-3}$ $(0.15 \cdot M_{\text{disk,init}})$	0.26
alM3em2_nPh	14	313.3	$3.4 \cdot 10^{-3}$ $(0.49 \cdot M_{\text{disk,init}})$	1.20

Table 4.9: Results for simulations where episodic accretion events occurred (with $\alpha_{\text{MRI}} = 0.03$). The noted quantities are the number of bursts, the time at which the disk enters its quiescent state (i.e. after the last burst), the disk mass at that time and the time when the accretion onto the central star stops. The two depicted photoevaporative models do not develop a gap.

magnetic field is strong enough, the accretion onto the star can be halted.

Concerning the photoevaporative model with a high MRI viscosity `alM3em2`, it can be observed that the number of bursts reduces to 7 and the quiescent phase already starts after 135 kyr. The reason for that is that photoevaporation takes a substantial fraction of mass out of the outer disk, which is then not available to resupply the inner disk with material after a burst any longer. As for all models discussed so far, the stellar X-ray luminosity for this model was chosen to be held constant (see Tab. 4.7). But as mentioned in Sec. 3.2.4, the effective stellar X-ray luminosity can also be calculated at every timestep as a function of the accretion luminosity according to Eq. 3.2.14. Since the accretion luminosity strongly increases during an episodic accretion event as described by Eq. 3.2.15, the photoevaporative mass loss rate increases accordingly. Therefore, an additional simulation run was conducted for the photoevaporative model with $\alpha_{\text{MRI}} = 0.03$ with the denotation `alM3em2_LXad`. It shares the same parameters with `alM3em2`, but the stellar X-ray luminosity was continuously adapted to the accretion luminosity. The time evolution of the inner boundary of the disk, the disk mass, the accretion rate and the photoevaporation rate for all three models showing accretion outbursts is illustrated in Fig. 4.21. The photoevaporative mass loss rate is of course inherently larger in the `alM3em2_LXad` due to the addition of the accretion generated X-ray luminosity. During a burst, an increase in the photoevaporation rate by a maximum factor of 3.3 can be observed. This increase is limited by the saturation of the mass loss rate at high stellar X-ray luminosities (see Sec. 2.2.2). The corresponding enhanced mass loss leads to a slightly steeper drop of the disk mass function and the point in time when accretion onto the star stops is reached sooner by 40 kyr compared to the `alM3em2` model. Fig. 4.20 shows an analysis of the accretion outbursts occurring in all three models. Despite the increased mass loss due to the adaptive photoevapo-

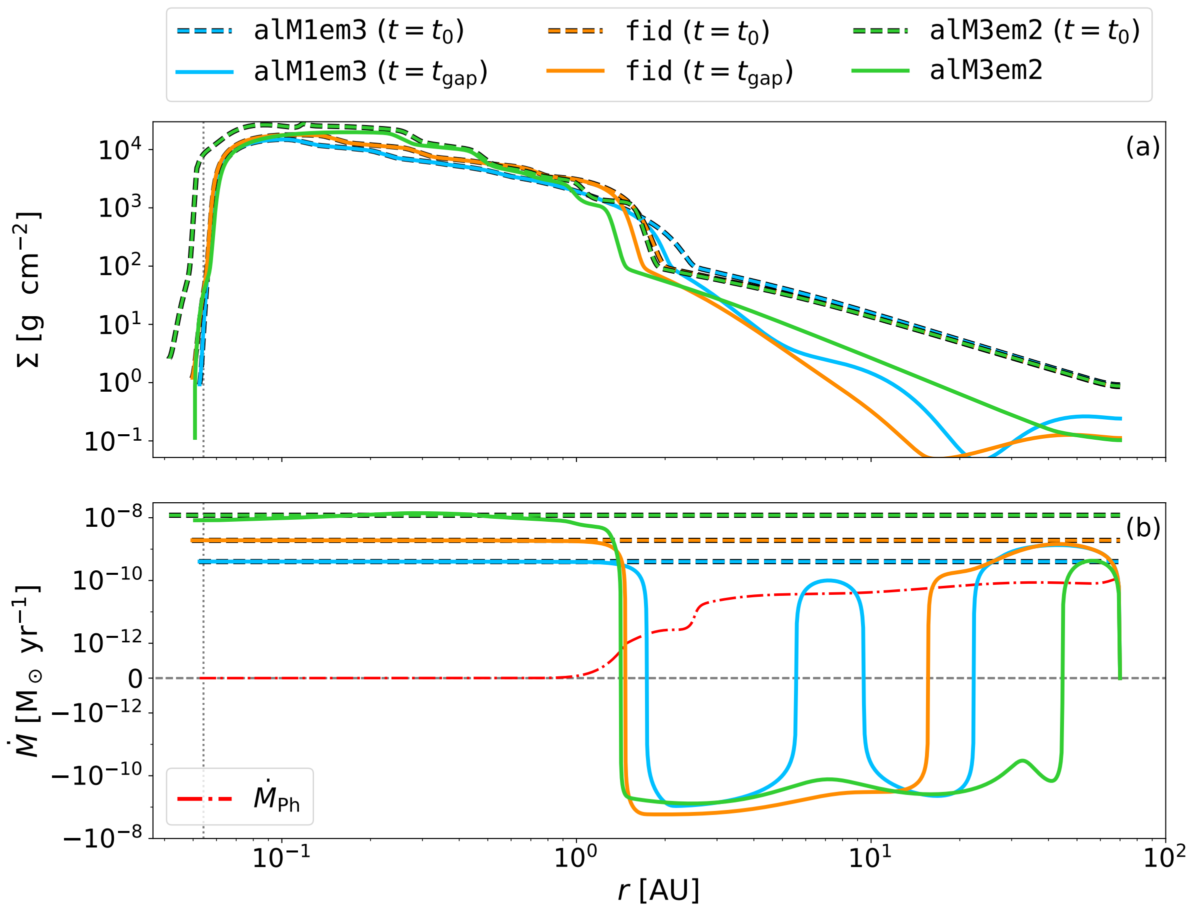

Figure 4.22: *(a)* Surface density and *(b)* mass flux profiles at the time of gap creation for the `fid` and `alM1em3` models and at the time the ZRVP$_2$ stops its outward movement for the `alM3em2` model, where no gap is created. The black-rimmed dashed lines show the initial conditions. The vertical grey dotted line marks the corotation radius and the red dash-dotted line in *panel b* represents the initial photoevaporation rate, which is the same for all three models.

ration rate, the models `alM3em2` and `alM3em2_LXad` show the same number of bursts. The incorporation of photoevaporation in general does not seem to have a significant effect on the bursts at the beginning of the evolution, as can be inferred from the similar location of the datapoints for the first 4 bursts in panels a, b and c. The differences become more apparent when investigating the latest bursts. These differences all arise from the fact that photoevaporation rids the outer disk of significant amounts of mass. Fig. 4.23 shows that the flux inversion caused by photoevaporation is already created during the outburst phase (which lasts until $t_{\rm quies}$, see Tab. 4.9). The datapoints of the photoevaporative models in panels a-c of Fig. 4.20 start to diverge significantly from the ones of the non-photoevaporative models as soon as the flux from the outer disk is significantly diminished by photoevaporation and the flux inversion is created. At this point in time, the dead zone is completely cut off from any mass flux coming from the outer disk. The bursts are then fueled only by material coming from the dead zone it-

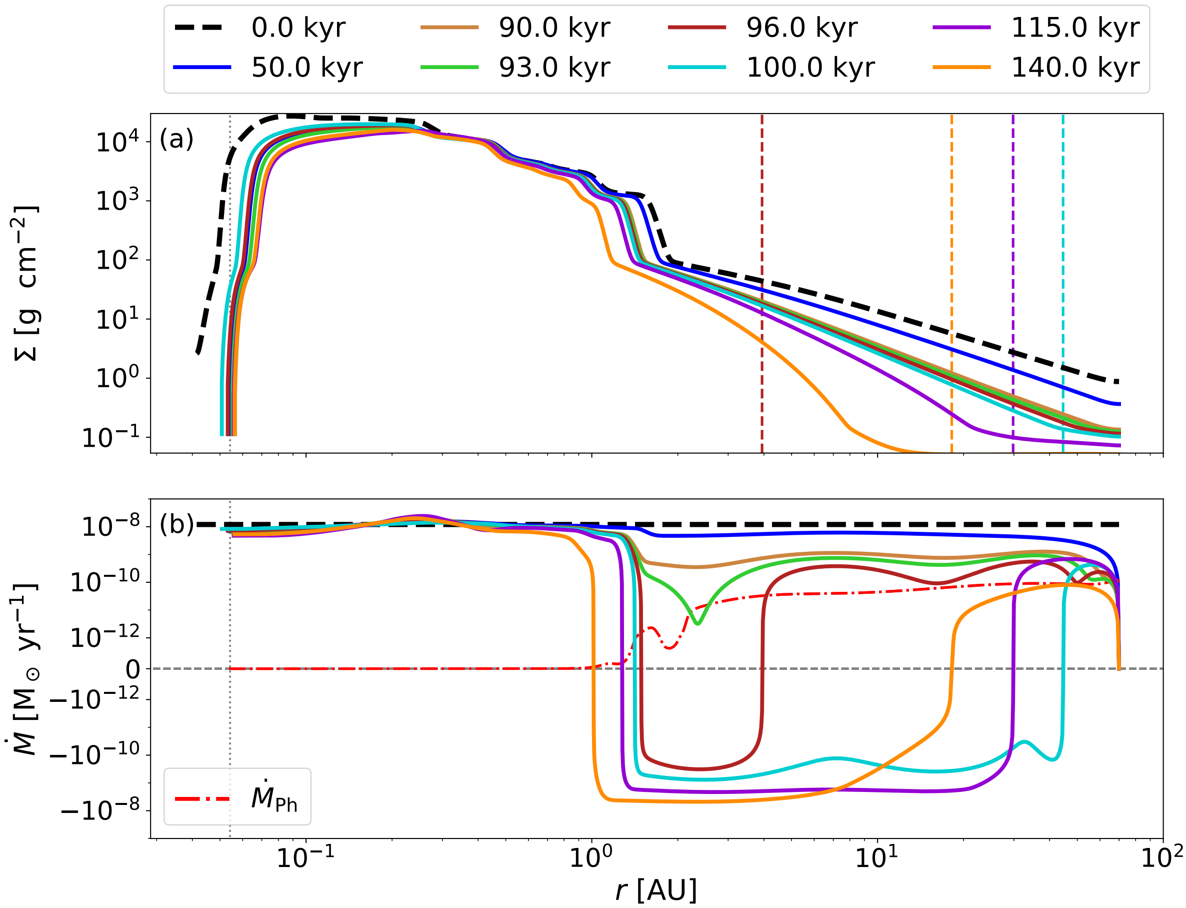

Figure 4.23: Same as Fig. 4.19 but during flux inversion and the movement of the $ZRVP_2$ of the `alM3em2` model. The mass in the outer disk is lost before a gap can be created.

self, which therefore shrinks at a faster rate compared to the `alM3em2_nPh` model. This leads to both a longer time between the bursts to refill the material lost and to less mass overall available for bursting, which consequently shortens the duration of the bursts. A larger photoevaporative mass loss rate as in the `alM3em2_LXad` model causes the flux inversion to happen at an earlier time and the aforementioned effects aggravate. This is especially observable at the last burst of the `alM3em2_LXad` model, which occurs almost 40 kyr after the previous one and lasts for a smaller amount of time, carrying much less mass towards the star compared to bursts at earlier times. This long duration between the last two bursts causes the disk to enter the quiescent state later than the `alM3em2` model with significantly less mass left in the remaining disk, as noted in Tab. 4.9.
Fig. 4.23 shows snapshots of the surface density and the mass flux during the development and expansion of the flux inversion in the `alM3em2` model. In this case, no photoevaporative gap is created[7]. As was established in the analysis of the previous photoevaporative models, the creation of a gap depends on the density and mass flux in the outer disk and the photoevaporation rate itself. In this case, the inward mass flux

[7]The same applies for the `alM3em2_LXad` model.

is large due to the high viscosity in the fully MRI-active outer disk. Therefore, photoevaporation requires a longer time to diminish the mass flux and create the flux inversion at the outer edge of the dead zone. In this case, this point in time is reached after 93 kyr (see Fig. 4.23) whereas in the fiducial model, the flux inversion already occurs at 50 kyr. After 93 kyr, the density in the outer disk has already been significantly decreased by the collaboration of photoevaporation and the large mass flux, periodically influenced by the episodic accretion events. As a result, the surface density in the outermost parts of the disk has already reached values low enough to decrease the α parameter (see Eq. 3.2.5). This leads to a second flux inversion in these very outer parts, similar to the case described above for the low viscosity case, but in this case, the flux diminishment is not caused by outward angular momentum transport, but by a sudden decrease in kinematic viscosity. After this, the remaining inward flux between the flux inversions vanishes quickly and the $ZRVP_2$ effectively jumps to a position in the outermost disk, visible in the flux profile after 100 kyr in panel b and the corresponding vertical dashed line in panel a of Fig. 4.23. The same surface density and mass flux profile is depicted in Fig. 4.22 together with the states of the disks of the `alM1em3` and `fid` model at the time of gap creation. Compared to the models which develop a gap, the $ZRVP_2$ of the `alM3em2` simulation is located much further away from the star. Since the density at this location is already so low when the $ZRVP_2$ arrives and still decreases outwards, photoevaporation is not efficient enough to locally diminish the density so that a gap can be created before the material in the outer disk has vanished as well. The further evolution shows that the outer disk is dispersed from outside-in by photoevaporation, as can be observed in Fig. 4.23.

4.4.2 Dead zone viscosity

For the final part of the parameter study, different values of $\alpha_{\rm base}$, which are listed in Tab. 4.10, are implemented. For these runs, the stellar parameters $L_\star$, $L_{\rm X}$, $L_{\rm X,soft}$, $B_\star$ and the viscosity of the MRI active regions $\alpha_{\rm MRI}$ are kept at their fiducial values (see Tab. 4.2). As was the case for the variation of $\alpha_{\rm MRI}$, the mass flux in the initial stationary model has to be adapted in order to achieve the same initial disk mass. The `alB5em4` and `alB5em4_nPh` models inherit an initial accretion rate of only 1.4 times the value of the `fid` model with the value of $\alpha_{\rm base}$ being higher by a factor of 5.

Model	$\alpha_{\rm base}$	$\dot{M}_{\rm init}$ $[M_\odot\ {\rm yr}^{-1}]$	Ph
`fid`	$1 \cdot 10^{-4}$	$1.90 \cdot 10^{-9}$	x
`fid_nPh`	$1 \cdot 10^{-4}$	$1.90 \cdot 10^{-9}$	
`alB5em4`	$5 \cdot 10^{-4}$	$2.65 \cdot 10^{-9}$	x
`alB5em4_nPh`	$5 \cdot 10^{-4}$	$2.65 \cdot 10^{-9}$	
`alB2em5`	$2 \cdot 10^{-5}$	$1.29 \cdot 10^{-9}$	x
`alB2em5_nPh`	$2 \cdot 10^{-5}$	$1.29 \cdot 10^{-9}$	

Table 4.10: Run parameters for simulations with different values of $\alpha_{\rm base}$.

Fig. 4.24 shows the time evolution of the position of the inner disk boundary, the disk mass and the accretion rate for all models noted in Tab. 4.10. Snapshots of the surface density during their evolution are depicted in Fig. 4.25. In both figures, the evolutionary timescales can be compared. As expected, a larger viscosity leads to a faster evolution. All three non-photoevaporating models reach a stationary state after the inner boundary has moved towards the corotation radius and the accretion onto the star stopped. The times when this occurs and the masses of the remaining disks are noted in Tab. 4.11. Not only does it take the longest for the `alB2em5_nPh` model to reach this state, but it also retains the most mass due to the inability of the low viscosity to keep up an accretion flow against the azimuthal acceleration by magnetic torque at the inner boundary any longer.

Fig. 4.26 offers a direct comparison of the initial surface density and mass flux profiles for the three models with different base viscosities. As mentioned in Sec. 4.4.1 in the context of the onset of accretion outbursts, the amount of piled up material inside the dead zone depends on the ratio $\alpha_{\rm MRI}/\alpha_{\rm base}$. This ratio has a value of 10, 50 and 250 for the `alB5em4`, `fid` and `alB2em5` model, respectively, which explains the difference in surface density in the dead zone between these three models. A surplus of mass in the dead zone has to be compensated by a lack of mass in the outer disk in

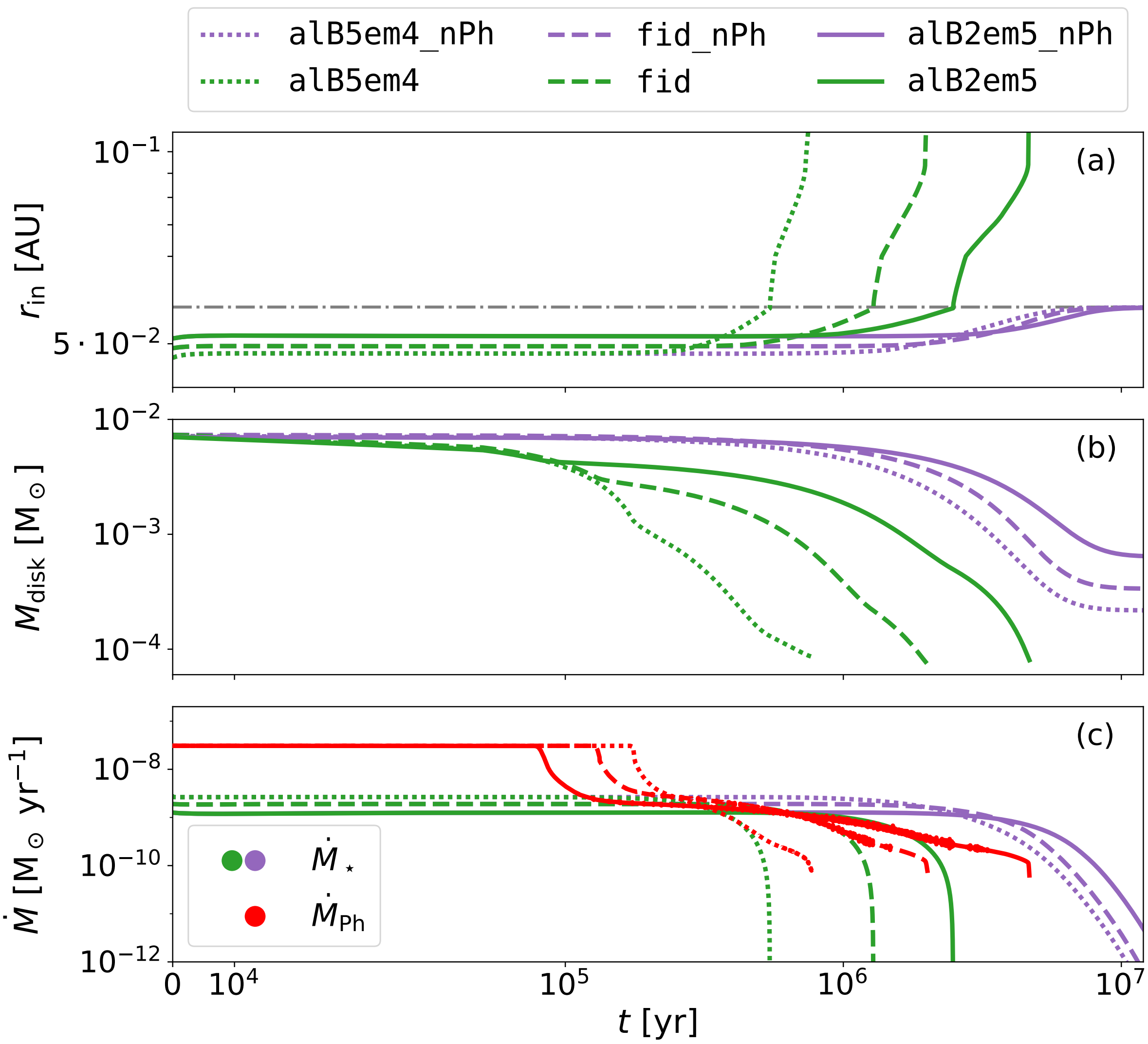

Figure 4.24: Time evolution of *(a)* the location of the inner disk boundary, *(b)* the disk mass and *(c)* the accretion rate onto the star for the models with different values of the $\alpha_{\rm base}$ parameter. The horizontal grey dash-dotted line in *panel a* marks the position of the corotation radius. The red lines in *panel c* indicate the total photoevaporative mass loss rate.

order to end up with the same total disk mass, which is why the surface density outside the dead zone is lowest for the `alB2em5` model. Despite the large $\alpha_{\rm MRI}$ to $\alpha_{\rm base}$ ratio in the `alB2em5` model, no episodic accretion events are triggered. This is because this large ratio was achieved by decreasing $\alpha_{\rm base}$ (as opposed to increasing $\alpha_{\rm MRI}$ as was the case in Sec. 4.4.1), which leads to an overall decrease of α. In order to keep the vertically integrated viscosity high, the large pile-up of material in the dead zone partially compensates the smaller kinematic viscosity. But due to the low disk mass, not enough mass can be accumulated in the dead zone to account for the decrease in α and cause sufficient viscous heating for pushing the temperature above $T_{\rm active}$. If the value of α was increased while keeping the same ratio of $\alpha_{\rm MRI}$ to $\alpha_{\rm base}$, the resulting increased viscous heating may be enough to trigger accretion outbursts even with disk

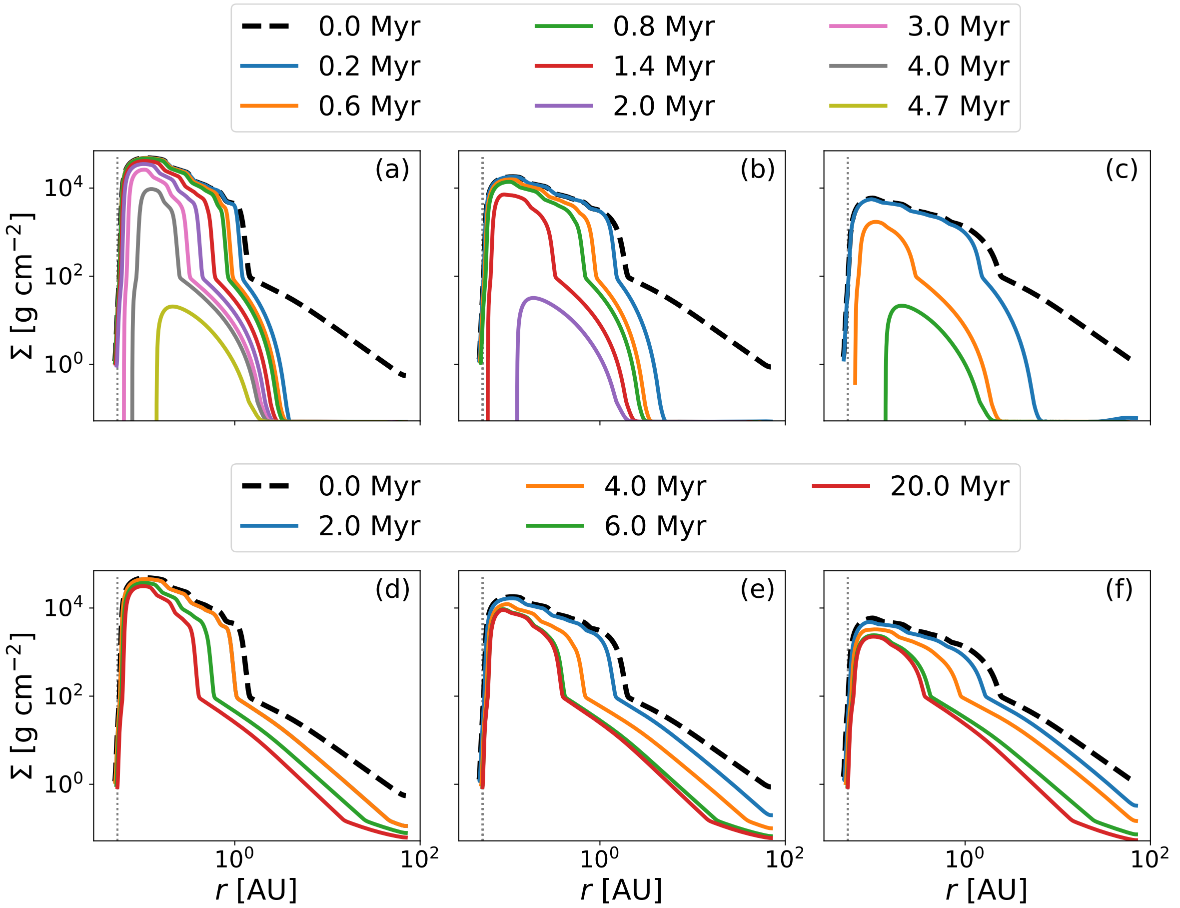

Figure 4.25: Evolution of the surface density of the models with different α_{base} values. *Panels a-c* show the photoevaporating models `alB2em5`, `fid` and `alB5em4` whereas the non-photoevaporating models are depicted in *Panels d-f*. The black dashed lines represent the initial, stationary conditions and the grey dotted line marks the corotation radius.

masses as low as in this case.

Fig. 4.26 also shows the surface density and the mass flux for the three models at the respective time of gap creation. This point in time, as well as the location of the gap and the total and outer disk masses are listed in Tab. 4.11. Due to the low initial mass flux in the `alB2em5` model, the flux inversion can be created quickly and the gap opens faster than in the other two models at a time of only 83.2 kyr. At this point, most of the disks remaining mass, which is 63% of its initial mass, is stored in the dead zone. On the other hand, the gap opens only after 175.9 kyr in the `alB5em4` model due to the larger mass flux, which leads to only a small remaining total mass 19% of the initial mass. The time of gap creation can once again also be seen in panel c of Fig. 4.24, where it coincides with the point in time at which the photoevaporation rate shows a sharp bend. Although the model with the largest viscosity evolves the fastest, the gap is opened at a later time than in models with smaller viscosities.

Despite the very different times of gap opening and the different remaining disk mass, the gap is opened at almost the same location for all three models with the same

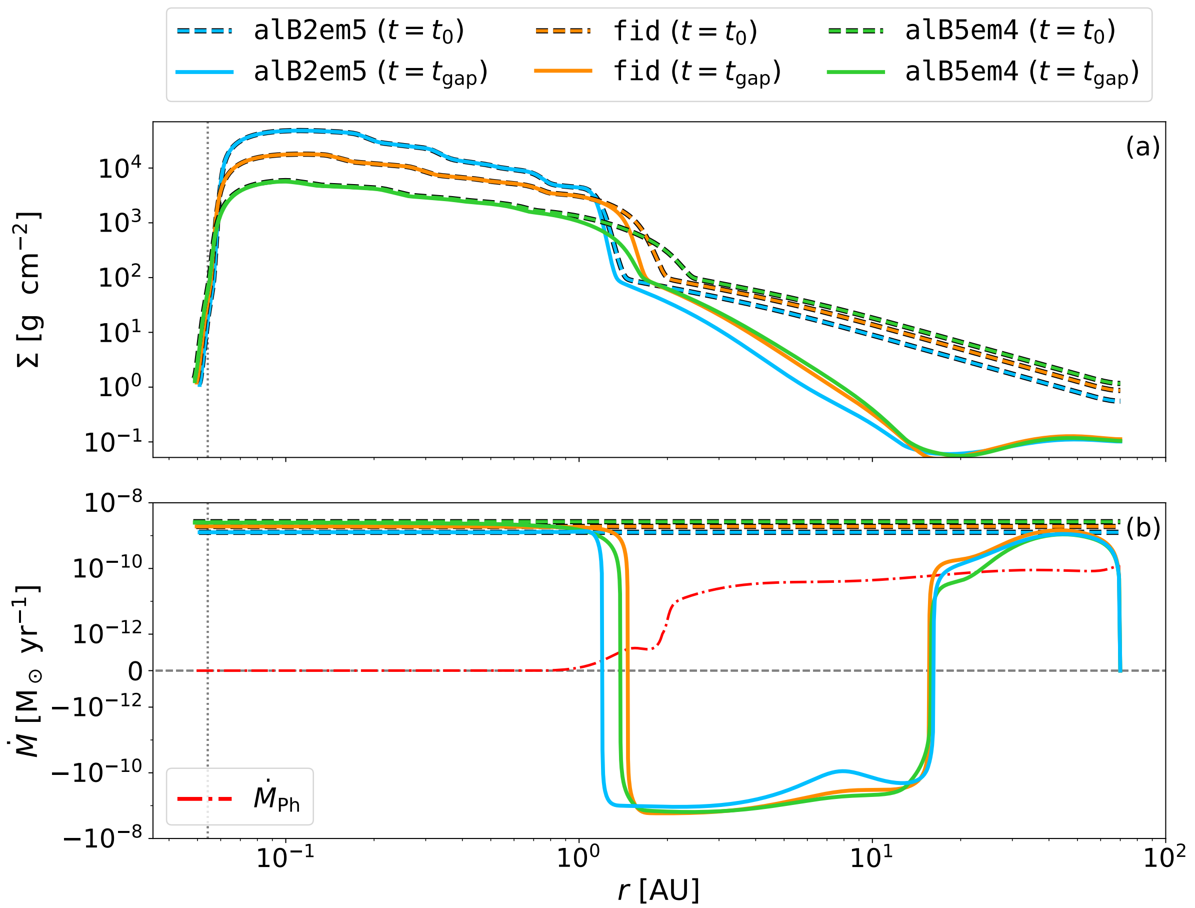

Figure 4.26: *(a)* Surface density and *(b)* mass flux through the disk for the three models with varying $\alpha_{\rm base}$ at the initial, stationary state (black-rimmed dashed lines) and at the time of gap creation. The red dash dotted line in *Panel b* shows the initial photoevaporation rate, which is equal for all three models.

amount of mass remaining in the outer disk, as observable in Fig. 4.26 and noted in Tab. 4.11. The reason for that could be that α takes the form of configuration 2 (Tab. 3.2) and is dominated by $\alpha_{\rm MRI}$ outside of the dead zone. When the flux inversion is created, the integrated mass flux from the outer rim of the dead zone to the outer disk boundary is approximately the same for the three models, while the surface density is already low (<5 g cm^{-2}) at the location where the gaps will be created. Since the viscous flux in the outer disk at this point in time is dominated by $\alpha_{\rm MRI}$ and is not affected by the difference between the initial conditions of the models anymore, the value of $\alpha_{\rm base}$ does not have a significant influence on the outward movement of the ZRVP$_2$. Therefore, its outermost position and consequently the location of the gap coincide for all three models.

Model	t_{gap} [ky]	r_{gap} [AU]	$M_{\mathrm{disk}}^{(t=t_{\mathrm{gap}})}$ $[M_{\odot}]$	$M_{\mathrm{disk,outer}}^{(t=t_{\mathrm{gap}})}$ $[M_{\odot}]$	$t_{\dot{M}_{\star}=0}$ [Myr]	$M_{\mathrm{disk,stat}}$ $[M_{\odot}]$
fid	130.5	16.8	$3.08 \cdot 10^{-3}$ $(0.44 \cdot M_{\mathrm{disk,init}})$	$1.8 \cdot 10^{-4}$ $(0.03 \cdot M_{\mathrm{disk,init}})$	1.28	
fid_nPh					18.4	$3.3 \cdot 10^{-4}$ $(0.05 \cdot M_{\mathrm{disk,init}})$
alB5em4	175.9	16.9	$1.3 \cdot 10^{-3}$ $(0.19 \cdot M_{\mathrm{disk,init}})$	$1.7 \cdot 10^{-4}$ $(0.02 \cdot M_{\mathrm{disk,init}})$	0.54	
alB5em4_nPh					16.1	$2.2 \cdot 10^{-4}$ $(0.03 \cdot M_{\mathrm{disk,init}})$
alB2em5	83.2	16.3	$4.4 \cdot 10^{-3}$ $(0.63 \cdot M_{\mathrm{disk,init}})$	$1.6 \cdot 10^{-4}$ $(0.02 \cdot M_{\mathrm{disk,init}})$	2.48	
alB2em5_nPh					24.5	$6.5 \cdot 10^{-4}$ $(0.09 \cdot M_{\mathrm{disk,init}})$

Table 4.11: Results for simulations with different values of α_{base}. The noted quantities are the same as in Tab. 4.4.

5 Discussion

In this thesis, the effects of X-ray photoevaporation on the long-term evolution of a protoplanetary disk, including layered viscosity and stellar magnetic torque, were investigated in the context of various stellar- and disk parameters. This section is dedicated to comparing the results to previous studies and to discuss the shortcomings and limitations of the model presented in this thesis.

5.1 Comparison to previous work and observations

Clarke et al. (2001) were the first to argue that the combination of photoevaporative mass loss and viscous evolution leads to the creation of a gap in the disk, after which the inner part quickly accretes onto the star. The outer part continues to slowly evaporate until the density of the inner disk becomes low enough so that the stellar radiation can reach the inner rim of the outer disk directly. This consequently leads to a faster dispersal of the outer disk (Alexander et al. 2006). This general process also resulted from several following studies (e.g. Owen et al. 2012; Ercolano et al. 2021; Kunitomo et al. 2021). Morishima (2012) recognised that this picture may not be accurate when layered accretion is considered. Using the X-ray photoevaporation model of Owen et al. (2011), they concluded that gaps can be opened beyond the dead zone and the outer disk can be evaporated before the inner disk disappears since at small radii, the disk evolves on a longer viscous timescale due to the suppressed MRI-activity in the dead zone. This phenomenon is also present in every simulation run conducted in this thesis. The models of Morishima (2012) also indicated that the value of the base viscosity $\alpha_{\rm base}$ does not have a significant influence on the gap location, unless it becomes high enough that the dead zone vanishes before a gap can be created. In these cases, the gap opens at very small radii (closer than 3 AU). Fig. 4.26 and Tab. 4.11 show that the gap location is indeed independent of the value of $\alpha_{\rm base}$, although it is never the case, that the whole disk becomes fully MRI active before the gap can be created.

A very similar approach was made by Gárate et al. (2021), who used the photoevaporation profiles of Picogna et al. (2019) to conduct a population synthesis study. They constructed populations out of different values of $\alpha_{\rm base}$ (while fixing the value of $\alpha_{\rm MRI}$ to 0.001) and various radial extents of the dead zone, which were fixed for their individual simulations. For each population, the range of stellar X-ray luminosity between 10^{29} erg s^{-1} and 10^{31} erg s^{-1} and a range of characteristic disk radii (from which the initial surface density profile followed) was sampled. Although the photoevaporation model they used was configured for a star-disk system with a stellar mass of 0.7 $M_\odot$, they implemented a solar mass star as the central object and an initial disk mass of 0.1 $M_\odot$. For time evolution of the surface density, they used the typical diffusion equation (Lynden-Bell & Pringle 1974), starting from the self-similar solution by Lynden-Bell & Pringle (1974) as an initial configuration. Additionally, the inner boundary of the simulation domain was fixed at 1 AU. In the original study, they assumed steady-state accretion in the disk following $\dot{M} = 2\pi r \Sigma v$, where v is a velocity depending on viscosity. But as an appendix, they added the same population synthesis starting from a stationary initial model with a constant mass flux throughout the disk. Despite the described significant differences in the disk model, the similarity of the photoevaporation model and the stationary initial configuration (in the appendix of Gárate et al. 2021) allows for a comparison of their population synthesis study with the results obtained in this thesis.

Fig. 5.1 shows the probability distribution regarding the relationship between the inner boundary of the outer disk after gap creation and the accretion rate onto the star, resulting from the population synthesis model of Gárate et al. (2021), as a grey shaded map. The population used for the creation of this map consisted of disks with $\alpha_{\rm MRI} = 10^{-3}$, $\alpha_{\rm base} = 10^{-4}$ and an extent of the dead zone of 10 AU. The grey dots represent observational data and the colored crosses with corresponding evolutionary tracks show the models described in Sec. 4. For the majority of their lifetime after gap creation, all models lie within the area where the occurrence of such disks also resulted from the population synthesis study. The dead zones of the simulations of this thesis do not extend as far as 10 AU, which is why they tend to produce gaps closer to the star than the shown shaded map would suggest. In addition to that, the different photoevaporation profiles, especially for the `LX29` and `LX31` models, lead to a further shift to smaller outer disk radii. The evolutionary tracks do not extend further towards larger gaps due to the small disk masses (0.007 $M_\odot$) and the outer disk boundary being set at 70 AU. In

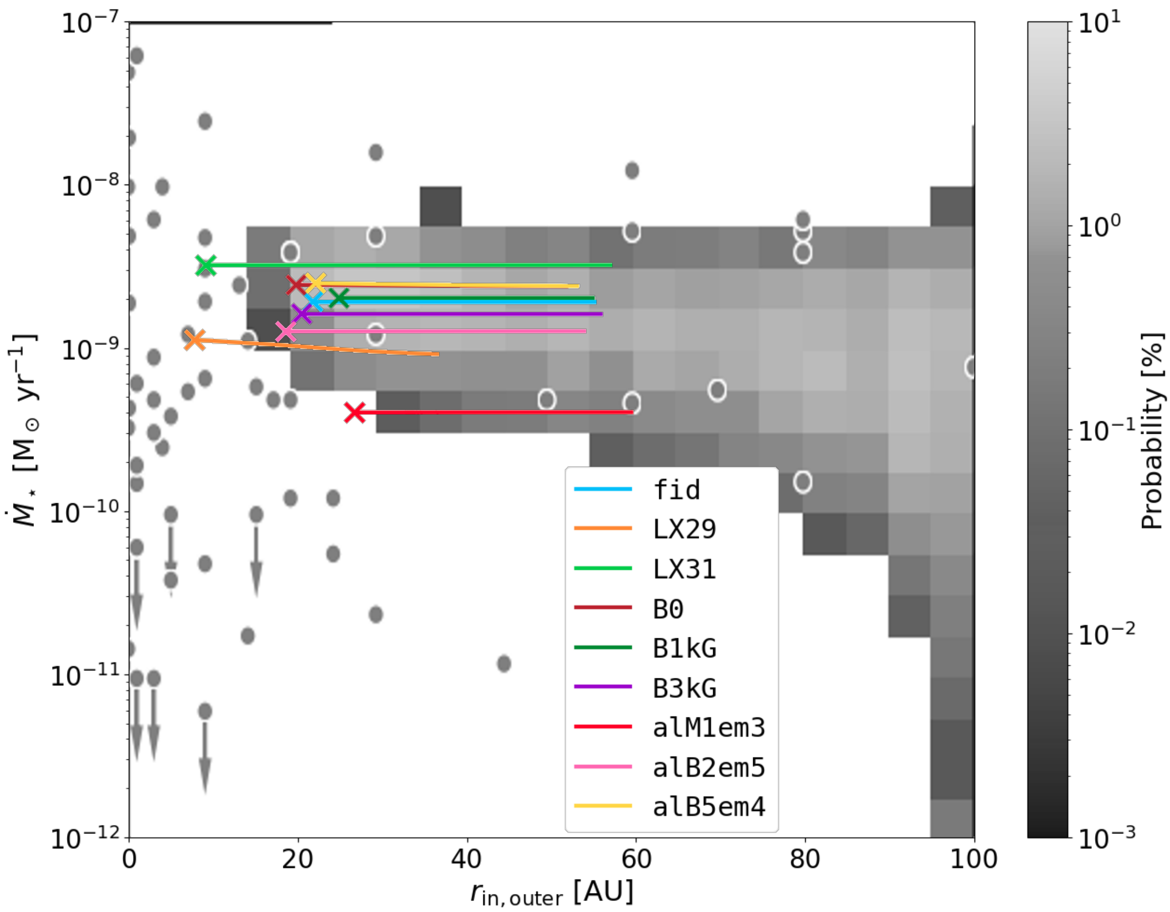

Figure 5.1: Location of the inner edge of the outer disk after gap creation vs. corresponding accretion rate onto the central star. The colored crosses mark the relation at the time the gap is created (i.e. $\Sigma = \Sigma_{\min}$ for the first time) while the colored lines indicate the subsequent evolution. The evolutionary tracks end when the outer disk has disappeared completely. The grey dots show observational data from transition disks (where points with arrows have to be understood as upper limits for the accretion rate), summarized in Ercolano & Pascucci (2017) and the grey shading represents the probability distribution calculated from a population synthesis model by Gárate et al. (2021).

agreement with the presented results, Bae et al. (2013a) also predict that disks which inherit a dead zone and develop a photoevaporative gap move horizontally towards larger gap radii, since the gap expands outwards quickly while the accretion process from the dead zone onto the star stays unfazed. The results of this thesis therefore agree with the findings of Morishima (2012) and Gárate et al. (2021), who argue that it is indeed possible to create transition disks with extended gaps while retaining a significant accretion when layered viscosity is considered.

Gárate et al. (2021) also offered a 'proof of concept', where they showed the evolution of the surface density and the mass flux for models with and without a dead zone. As a comparison, Fig. 5.2 depicts the evolution of such a model without a dead zone,

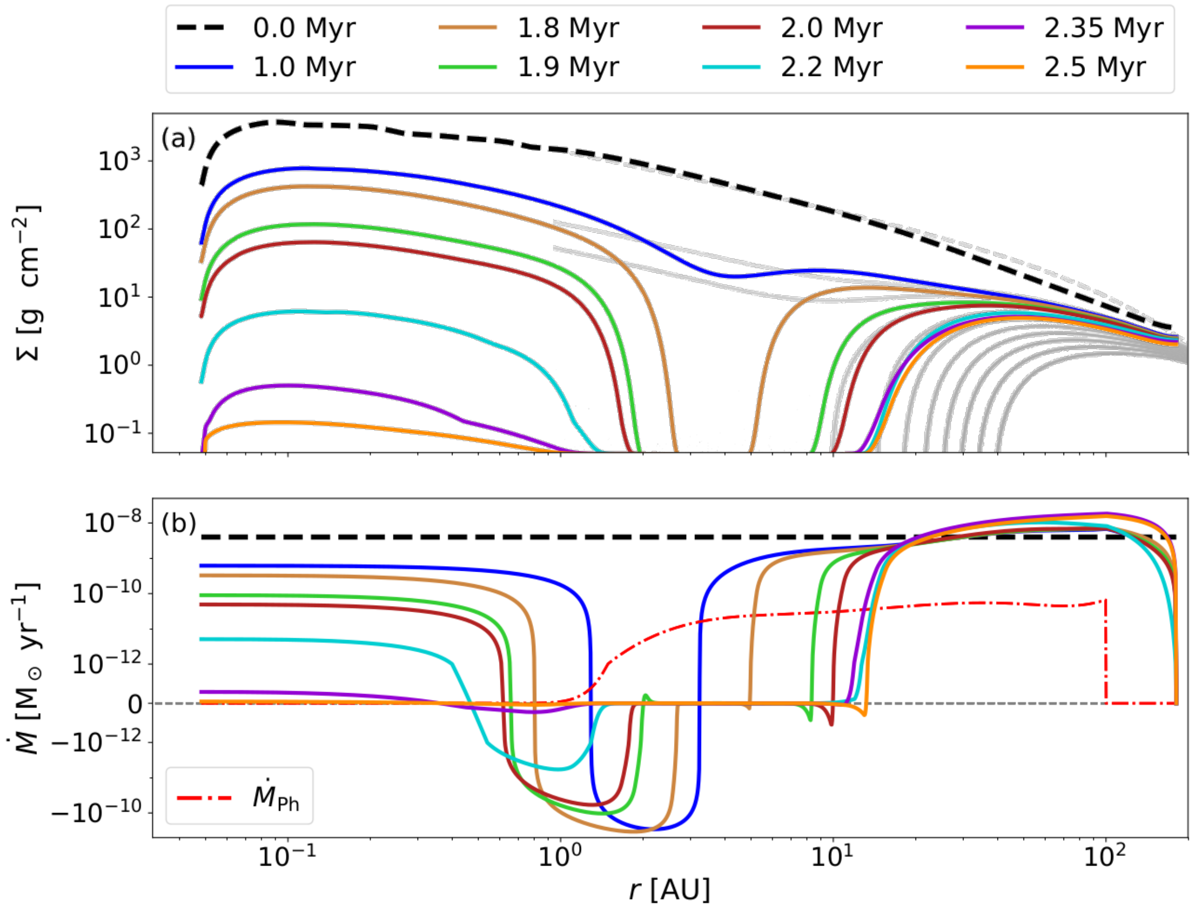

Figure 5.2: Snapshots of the surface density and the mass flux during the evolution of a 0.1 $M_\odot$ without the influence of a stellar magnetic field and without a dead zone ($\alpha(r) = \mathrm{const.} = 10^{-3}$) for comparison with the 'proof of concept' in Gárate et al. (2021). The evolution of the surface density of the model by Gárate et al. (2021) is shown as grey profiles, where the initial model is indicated as a dashed line. Starting at 2.5 Myr, the solid grey lines illustrate the surface density profile every 0.2 Myr. The inner boundary of their simulation was fixed at 1 AU.

calculated with the TAPIR-Code. For better comparison, the star-disk connection via a stellar magnetic field has been omitted and the disk parameters have been chosen to match the model of Gárate et al. (2021) as closely as possible ($M_{\rm disk} = 0.1\mathrm{M}_\odot$, $\alpha(r) = \mathrm{const.} = 10^{-3}$). The most significant difference between the two approaches is the initial model, where Gárate et al. (2021) used $\dot{M} = 2\pi\Sigma v$ (as mentioned above) and the simulation conducted with the TAPIR-Code and shown in Fig. 5.2 starts from a stationary state with constant mass flux. Since the disk mass is much higher than in the previously presented models, potential gravitational instabilities are neglected, which may severely reduce the physical accuracy of such simulations. Fig. 5.2 shows the expected 'standard' evolution of a disk undergoing photoevaporative dispersal, as established and studied since Clarke et al. (2001): a gap opens at small radii (in this case at 3 AU) after which the inner disk is dispersed over the course of a few 10^5 yr.

Note that the inner disk does not drain completely onto the star, but the flux inversion leads to an outwards flux of a part of the inner disk mass towards the photoevaporation regime. Relative to the disk lifetime, the inner disk disappears at a slower rate than in Gárate et al. (2021), which may be a consequence of the different initial mass flux configurations. Otherwise, the outcomes of these two simulations agree reasonably well, which shows that the TAPIR-Code is indeed capable of reproducing previous, well established results.

After the inner disk has vanished, the outer disk is exposed to the direct irradiation from the star, which leads to an enhanced photoevaporation rate (Alexander et al. 2006). The corresponding mass loss profile is also implemented in the TAPIR-Code, following Picogna et al. (2019), but has not been active in the results of this thesis shown so far, since the outer disk vanishes before the density in the inner disk becomes low enough. The simulation shown in Fig. 5.2 is the only model where direct irradiation of the outer disk would be relevant.

Due to the missing dead zone, the surface density is distributed more evenly over the disk, which is why the outer boundary can be moved to significantly larger radii without the density dropping to too small values. In Fig. 5.2, the outer boundary was set at 180 AU. Following Ercolano et al. (2021), the photoevaporation profile shown in panel b drops sharply to zero at 105 AU, which results from shadowing of the outer disk from the stellar X-ray radiation by dense, photoevaporative winds in the inner disk regions. Typically, this drop is not as sharp as depicted, but for the purpose of showing the overall, long-term evolution of the disk, this is of minor importance. Interestingly, panel b also shows that the flux inversion occurs at a very similar location compared to e.g. the `fid` model with a dead zone. But due to the high mass flux in the outer disk and the lack of outwards transported angular momentum without a dead zone, the movement of the ZRVP_2 is slow, allowing for the creation of a deep gap at small radii.

Fig. 5.3 depicts the surface density and mass flux evolution of the same model as in Fig. 5.2, but with a disk mass of 0.007 $M_\odot$ and $\alpha(r) = \mathrm{const.} = 5 \cdot 10^{-3}$, as also used for the `fid` model. In this case, the surface density in the outer disk is already low (<1 g cm^{-2}) at the time of gap creation. As a consequence, when the inner disk disappears, the outer disk has almost (but not entirely) evaporated already. Figs. 5.2 and 5.3 indicate that without a dead zone, disks with large gaps and high accretion rates (as frequently observed, e.g. Francis & van der Marel 2020) are hardly reproducible with X-ray photoevaporation models.

Bae et al. (2013a) used a layered accretion model based on Zhu et al. (2010a,b), which is similar to the one used in this thesis, to simulate variable accretion outbursts in combination with the photoevaporation model of Owen et al. (2010, 2011, 2012). Their study also included mass infall from the protostellar cloud. For the evolution of

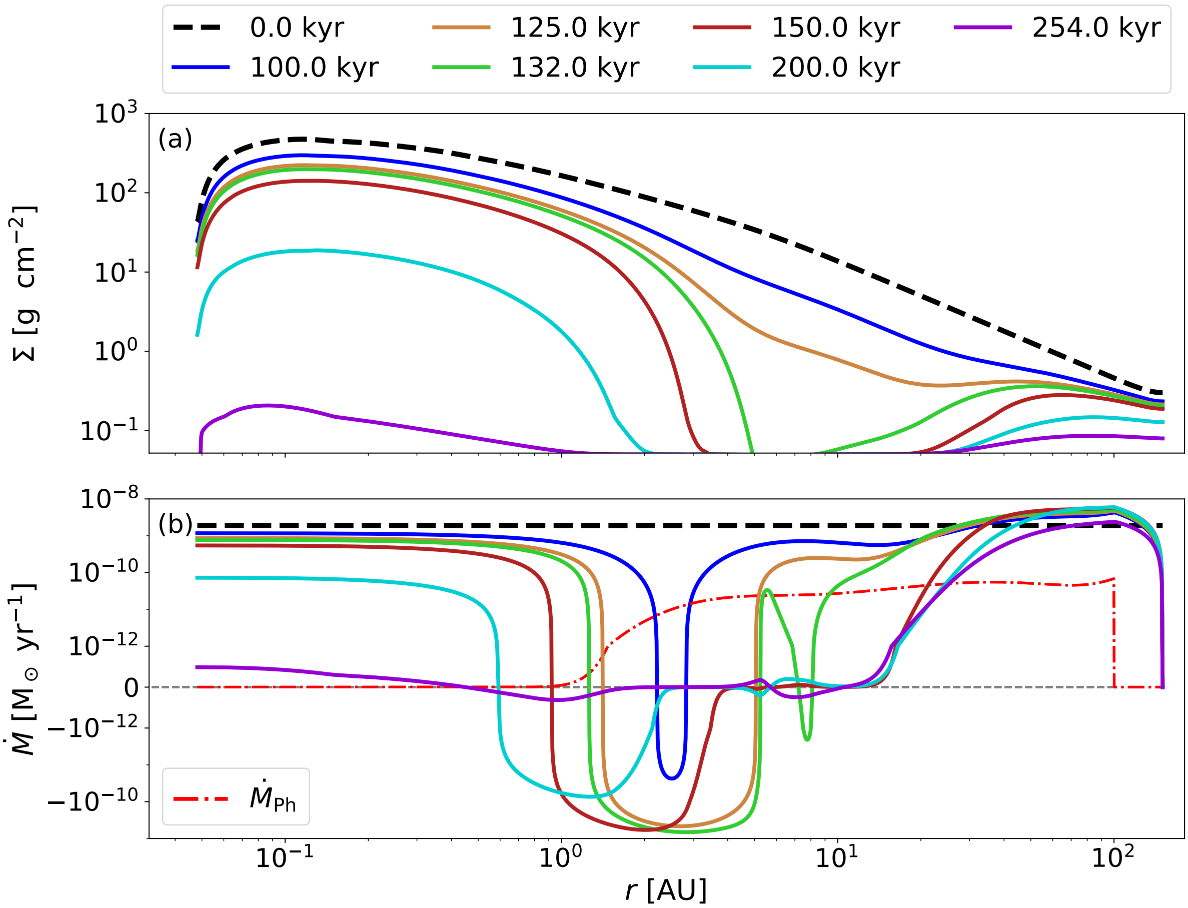

Figure 5.3: Same as Fig. 5.2, but for a disk with the same mass as in the simulations presented in Sec. 4 (0.007 M$_\odot$) and $\alpha(r) = \mathrm{const.} = 5 \cdot 10^{-3}$

the surface density, they simultaneously solved the equations for the conservation of mass (equation of continuity) and angular momentum (azimuthal equation of motion), as explained in Bae et al. (2013b). For their models with $\alpha_{\mathrm{MRI}} = 10^{-2}$ and $\alpha_{\mathrm{base}} = 10^{-4}$, they found that no photoevaporative gaps are opened in the outer disk, agreeing with the `alM3em2` model. However, they observed that once the dead zone has depleted, a gap is opened at small radii, similar to the findings of Morishima (2012). The small inner disk is then immediately drained onto the star, exposing the outer disk to direct irradiation, similar to the process for disks without dead zones, described e.g. by Alexander et al. (2006). This does not occur in the `alM3em2` model. Beside the differences in the used photoevaporation models, another reason for that could be that the propelling effect of the stellar magnetic field (which was not included in the models of Bae et al. (2013a)) turns the mass flux outwards throughout the whole disk in the late stages of evolution. That way, no ZRVP$_2$ can ever be created in the inner disk. As Bae et al. (2013a) point out, these comparisons show that the evolution of a disk influenced by photoevaporation (especially the time and location of gap opening) is very sensitive to the details of the used simulation models.

Owen (2016) report that the photoevaporative process can serve as a candidate to explain the occurrence of transition disks, which show a suppressed infrared excess in observations due to cavities or large gaps in the dust component. The 'standard' photoevaporation scenario of gap creation $\rightarrow$ inner disk drainage $\rightarrow$ direct irradiation of outer disk has been investigated for that purpose in the context of EUV-, FUV- and X-ray heating. Using this model, long-lived, non-accreting transition disks can be produced due to the rapid disappearance of the inner disk after gap creation and the comparably slow dispersal of the outer disk. According to Owen (2016), an open problem concerning this process is the reproduction of optically thick, accreting transition disks, which are observed more often than their non-accreting counterparts. As the results of this thesis indicate, when considering the suppression of MRI activity in the inner disk and the resulting small viscosity in combination with the propelling effect of the stellar magnetic field, X-ray photoevaporation can produce large gaps out to radii of several dozen AU while maintaining significantly high accretion rates (Fig. 5.1). Such disk structures have been observed by Van Der Marel et al. (2016) by using CO isotopologs with ALMA, although they argue that the central disk cavities are most likely produced by an embedded planet. They found that the gas density shows a significant drop, while the dust has been cleared out completely in the cavities, without a sign of a retained inner dust disk. They mention that a dead zone would not change the gas density in the cavity, but there has to be a significant amount of gas close to the star to explain the observed high accretion rates. The simulations in this thesis show that a dead zone can have small radial extents (approx. 1 AU, which may hardly be observable with ALMA) and still maintain high accretion rates in disks with large gaps, devoid of gas and dust.

Francis & van der Marel (2020) also investigated a large sample of transition disks observed with ALMA. They found that a large part of their sample shows inner dust disks together with large cavities. In the case of AA Tauri (e.g. Bouvier et al. 2013), which is a K7 type star with a mass of 0.66 $M_\odot$ and a bolometric luminosity of 1.1 $L_\odot$, they determine a gap in the surrounding disk, ranging from approximately 4.5 AU to 44 AU, which would be consistent with e.g. the `fid` model after 150 kyr (Fig. 4.5). However, they report a depletion of dust in the inner disk relative to the outer disk, which indicates dust trapping by an embedded planet rather than photoevaporation. But since they only observed the dust component without measuring the gas content as well, the photoevaporation scenario including a layered viscosity approach cannot be ruled out. Since in this thesis, a constant gas-to-dust ratio of 100 is assumed for the whole disk at any time, comparisons with separate gas or dust observations have to be taken with a grain of salt. But the modelling of the observed disks done by Van Der Marel et al. (2016) and Francis & van der Marel (2020) show that surface densities as low as 10^{-2} g cm^{-2} (as resulted from the simulations in this thesis) can be measured. This means that gaps created when the surface density in the outer disk has already dropped to values of the magnitude 1 g cm^{-2} (which is the case for most simulations, except for `alM1em3` where the viscosity is low and `LX29` and `LX31` where the gap is carved at smaller radii) are indeed observable.

5.2 Model limitations

The version of the TAPIR-Code used in this thesis inherits a combination of features for simulations of protoplanetary disks which have not yet been coupled with photoevaporation in previous studies. The implicit integration scheme allows for a self-consistent treatment of the inner disk including the star-disk connection by the stellar magnetic field while retaining the possibility of long-term evolution simulations. The solution of the full set of hydrodynamic equations at every timestep eliminates the shortcomings of the commonly used diffusion equation for surface density evolution. Even though episodic accretion events and photoevaporation are considered in the calculations, the TAPIR-Code can produce full simulation runs of the entire disk lifetime in a matter of minutes to a few hours due to the adaptive timestep ranging from $\sim 10^4$ s to over 10^5 yr. The implicit method allows for such calculations on ordinary workstations with no need of big computer clusters. However, there are certain limitations to the model presented in this thesis, which have to be taken into account.

Some of these limitations have already been described by Steiner et al. (2021). They mention that the 1D approach and the therefore assumed axisymmetry is suited for simulations of the the inner parts of the disk, since potentially non-axisymmetric perturbations cannot be sustained. This is in principle not the case for larger radii due to the weaker viscous shear and larger dynamic timescales. Since the radiation of the central star does not have a preferred direction, the assumption of axisymmetry of the resulting photoevaporative effect is reasonable for the whole disk. In order to avoid non-axisymmetric effects resulting from gravitational instabilities, the disk masses of all simulations in this thesis have been chosen to bee small, so that the fulfillment of the Toomre criterion can be avoided (see Sec. 3.2.2). Since there are also no other massive bodies like planets or stellar companions included, which could e.g. lead to the formation of spiral structures (e.g. Fung & Dong 2015), the risk of formation of non-axisymmetric perturbations has been minimized.
Steiner et al. (2021) also argue that photoevaporation in the inner disk should have an effect on the interaction between the disk and the star through the stellar magnetic field since a significant amount of gas should be removed. Fig. 3.2 indicates that photoevaporative mass loss rate is typically very small at small radii (inward of 1 AU) since on the one hand, the gravitational potential is too large in these regions to launch a thermal flow and on the other hand, the irradiation angle of the stellar radiation onto the disk is shallow. Therefore, photoevaporation does not have a direct influence on

the qualitative behaviour of the inner disk. But as the comparison between photoevaporating and non-photoevaporating models in Sec. 4 show, the removal of material from the outer disk has an effect on the time after which the inner disk boundary moves towards the corotation radius and the accretion onto the star stops. Furthermore, the flux inversion created by photoevaporation, which is extended throughout the whole disk by the propelling effect of the stellar magnetic field, allows the inner boundary to cross the corotation radius, after which the whole remaining disk is dispersed by an outward flow of mass towards the region of effective photoevaporation. Therefore, an indirect effect of photoevaporation on the inner disk can indeed be observed. But to investigate the precise interactions between the processes in the very inner disk and the potential local photoevaporative mass loss, more rigorous 2D or 3D simulations of photoevaporation with particular attention to the inner disk have to be conducted.

The photoevaporation profiles used for the models in this thesis are implemented without regarding the underlying disk structure. As argued by Owen et al. (2012), X-ray photoevaporation should indeed be independent of the disk thermal and density structure and only be determined by the X-ray properties of the central star. More recent studies indicate that this might not be entirely accurate (as reviewed by e.g. Gorti et al. 2016). The differences in the three photoevaporation profiles used in this thesis, which result from different disk structures in the simulations of Ercolano et al. (2021), already point towards this fact. But to completely and accurately determine the photoevaporative mass loss at every radius fitting to the current state of the disk, the photoevaporative flows have to be calculated from the disks thermal structure at every timestep, which is only possible in 2D or 3D models. An approximation in 1D simulations can in principle be made by e.g. assuming a Parker wind solution (Waters & Proga 2012), but this would require a large amount of additional computational effort and is not guaranteed to yield more accurate results than the pre-calculated mass loss profiles already available in the literature.

The photoevaporation profiles of Ercolano et al. (2021) were calculated with regard to X-ray and EUV heating using a disk model with simplified thermochemistry. This was motivated by the findings of Picogna et al. (2019) on the one hand, which indicate that X-ray heating is dominant and that the neglected cooling terms do indeed not influence the photoevaporation rate, and on the other hand again by referring to Owen et al. (2012), who argue that the disk structure does not affect the X-ray heated thermal wind. Other models including FUV heating and advanced thermochemistry (Wang & Goodman 2017; Nakatani et al. 2018) imply that FUV heating may be the dominant mechanism to drive photoevaporation, while X-rays and EUV radiation only play a minor role (contrary to the arguments made by Owen et al. 2012). But in order to properly include FUV heating in global simulations, processes like dust evolution and the tracking of PAH abundances are necessary, which are not included in the results presented in this thesis.

As mentioned in Sec. 5.1, a constant gas-to-dust ratio of 100 is assumed in the current state of the TAPIR-Code. Photoevaporation is assumed to remove mostly gas from the disk, while dust is entrained in the wind (e.g. Franz et al. 2022). But the rate at which dust is removed from the disk by entrainement is much smaller than the gas mass loss rate (Franz et al. 2022) which would in principle reduce the gas-to-dust ratio in the photoevaporation regime. A dust evolution model which also includes the radial dust drift would therefore be desirable.

Using an implicit integration scheme requires a substantial amount of effort in numerics to produce results compared to an explicit method. In addition to that, the risk of encountering mysterious numerical difficulties is much higher. The most notable measure to avoid such difficulties is the implementation of the factor $v(\Sigma)$ in the viscosity and photoevaporation description. It ensures that the density in the photoevaporative gap and during outer disk dispersal does not drop below 0.05 g cm^{-2}. It already reduces the photoevaporation rate and the viscosity in a certain threshold above this limiting value (as observable in Fig. 4.5). This could have a potential impact on the exact location of the gap since the density in the outermost disk is already low enough for $v(\Sigma)$ to be effective before the gap is created. As a possible consequence, a disturbance of the mass flux in the outer disk can be caused, influencing the movement of the ZRVP$_2$ and the dispersal of the outer disk. However, this does not have an effect on the qualitative findings of this thesis.
The necessity of $v(\Sigma)$ arises because the timestep of the simulation is reduced by several orders of magnitude as soon as the density drops below approximately $\Sigma_{\min}$. The resulting timesteps are unfit to be used for long-term simulations. A possible reason for this numerical problem could lie in the formulation of the energy equation. Steiner et al. (2021) describe the term for the net heating and cooling rate $\dot{E}_{\rm rad}$ (Eq. 3.3.5) in the optically thick limit (with the optical depth $\tau \to \infty$). Therefore, a temperature at the disk surface and at the disk midplane can be defined. When the density drops to significantly low values, this description breaks down, which is why in Fig. 4.11, the gap does not leave a signature in the $T_{\rm gas,0}$ profile. In order to solve this issue, the optically thin case ($\tau \to 0$) has to be considered as well and correspondingly implemented in the energy equation, which will be done in future work.
Another consequence of this shortcoming is that if the star-disk interaction via the stellar magnetic field is included, the simulations are unable to evolve the disk to the point of complete dispersal, contrary to the `B0` model without a stellar magnetic field (Fig. 4.12). The respective latest model for the simulations including photoevaporation shown in Figs. 4.1, 4.8, 4.14, 4.18 and 4.25 represent the state of the disk at the time when the timestep of the simulations has decreased to such low values that no further evolution can be observed. This is most notable in the `alM1em3` model, where the simulation had to be terminated before the dead zone had disappeared. When the inner

disk boundary crosses the corotation radius and the propeller effect causes the $ZRVP_1$ to reach the inner boundary, the radial velocity of the innermost grid cell is set to 0 and the the mass flows outwards throughout the whole disk. This leads to a rapid decrease in density and gas pressure in the innermost cell, pushing the inner boundary further outwards. At larger radii, the magnetic pressure and the gas pressure at the inner rim become very small, potentially making the definition of the location of the inner boundary inaccurate. Combined with the aforementioned inaccuracy of the energy equation at low densities and the large density gradient at the inner boundary, this leads to a severe reduction of the timestep. A potential solution for this lies in another definition of the inner boundary after accretion onto the star has stopped. However, this problem has no influence on the statements made about gap formation, outer disk dispersal and mass flux inversion in this thesis.

The definition of the inner boundary location also causes some imprecision in the models showing accretion bursts `alM3em2`, `alM3em2_LXad` and `alM3em2_nPh`. Fig. 4.21 showing the time evolution of the inner boundary is qualitatively different from the ones presented in Steiner et al. (2021). The reason for that is that the accretion rates during the bursts occurring in this thesis are so high that numerically, the inner boundary of the computational domain would be pushed to radii smaller than $R_\star$. This primarily results from the large $\alpha_{\rm MRI}/\alpha_{\rm base}$ ratio. To prevent this, the inner boundary stays at the last location before reaching the stellar surface until the accretion rate decreases again. This may have an impact on the detailed structure of the bursts, but does not influence the consequences of photoevaporation.

Finally, the initial models for the simulations presented in Sec. 4 are constructed so that the initial disk masses are the same for all simulation runs in order to make them comparable. This is achieved by adapting the initial constant mass transport rate through the disk $\dot{M}_{\rm init}$ (as described in Sec. 3.2.1). Another possibility of making the individual models comparable is to fix the initial mass flux through the disk for all simulations and let the initial disk mass adapt to the chosen parameters. Which of these two approaches to choose depends on what the primary focus of the conducted simulation runs is. In this thesis, the focus lies on the effects of the photoevaporative mass loss on different disk structures and the evolutionary timescales. For this, the choice was made to use the disk mass as a quantity with which the different simulation runs can be compared during different stages of evolution (e.g. time of gap formation, inner and outer disk mass, mass of the final stationary state of non-photoevaporative disks). Since the evolution of the mass flux in the outer disk is crucial for the gap formation process, using the same initial mass transport rates through the disk for all simulations could result in different gap locations and different times of gap creation. But in that case, the comparability of the models via disk mass would be lost. This indicates again that the choice of the initial models has to be well-considered, since it cannot only severely impact the evolution of the simulated disk, but also determines the factors which make all conducted simulations comparable.

6 Conclusion and further work

In this thesis, the fully implicit 1+1D hydrodynamic TAPIR-Code (Ragossnig et al. 2020) is utilized to simulate the long-term evolution of protoplanetary disks under the influence of X-ray photoevaporation. Several stellar- and disk parameters are varied in order to analyze their effect on the disk's temporal behaviour. The full set of hydrodynamic equations, which is solved at every timestep, includes the effects of the star-disk connection via a stellar magnetic dipole field and takes local pressure gradient forces into account. Dead zones in the inner disk regions are considered by the implementation of a layered viscosity model, which can also lead to thermal instabilities and episodic accretion events. To describe the mass loss through photoevaporative winds, pre-calculated mass loss profiles by Ercolano et al. (2021) are used and the corresponding terms are implemented in the hydrodynamic equations. The profiles result from 2D hydrodynamic simulations of disks heated by X-ray and EUV radiation from stars inheriting different, synthetic X-ray radiation spectra, based on observations. The resulting mass loss rates are only dependent on the luminosity of the soft part of the stellar X-ray spectrum and the radial distance from the central star.
The timestep of the implicit integration method is not limited by the CFL-condition, which allows for a self-consistent treatment of the inner disk regions while maintaining the ability to conduct long-term simulations. An adaptive timestep control scheme is implemented for the integration of the hydrodynamic equations on an adaptive, staggered-mesh numerical grid with the inner boundary being set at the magnetic truncation radius. As an initial configuration, a stationary state with a constant inward mass flux throughout the whole disk is utilized.
For every simulation, a central star with a mass of 0.7 $M_\odot$ is used and the disk mass is chosen to be small (0.007 $M_\odot$) in order to minimize the risk of non-axisymmetric perturbations resulting from gravitational instabilities. The evolution of the fiducial model shows that without photoevaporation, the disk evolution would enter a quasi-stationary state where the mass flux has been halted in the whole disk as soon as the inner boundary arrives at the corotation radius, stopping the accretion process. Hereby, the mass flux is directed towards the star during the whole evolution. When influenced by photoevaporative processes, a mass flux inversion is created at the outer edge of the dead zone as soon as the mass flux in the outer disk has been reduced to a point where it is completely evaporated when arriving at the dead zone. As the mass flux is reduced further, two points of zero radial velocity are created, the first of which ($ZRVP_1$) stays at the dead zone boundary while the second ($ZRVP_2$) moves outwards. The $ZRVP_2$ is a

location where photoevaporation removes mass while no replenishment is arriving from either smaller or larger radii. The gap is created at the point where the photoevaporation at the $ZRVP_2$ can first reduce the density to virtually zero before moving further. In the area between the $ZRVP_1$ and the $ZRVP_2$, the mass flux is turned outwards through a combination of viscous angular momentum transport from the dead zone and the gas pressure gradient. The gap then expands and the outer disk is completely evaporated while the inner disk and the accretion rate onto the star remain unchanged. Thereupon the radial extent of the dead zone starts to decrease as the inner disk is accreted with the $ZRVP_1$ initially staying at its outer edge. As the accretion rate decreases, the inner boundary moves towards the corotation radius, which eventually causes the $ZRVP_1$ to cross the dead zone and arrive at the inner boundary by the influence of the propelling effect of the stellar magnetic field outside the corotation radius. Consequently, the mass flux is turned outwards throughout the whole remaining disk, carrying mass towards the area of effective photoevaporation, leading to the final dispersal of the disk. The time after which a gap is created and the disk is dispersed strongly depends on the stellar luminosity, owed to the corresponding X-ray luminosity and photoevaporation rate as well as to the temperature-dependent viscosity. The structure of the used photoevaporation profile has a large impact on the location of gap creation. This is supported by the finding that the gap is created at almost the same location in the two simulations with an X-ray luminosity of 10^{29} erg/s and 10^{31}erg/s while it is created further outwards for the model with 10^{30} erg/s.
Without the influence of the torque created by the stellar magnetic field, the mass flux in the disk is never turned outwards throughout the whole disk since the $ZRVP_1$ cannot cross the dead zone or move further inward when the dead zone has vanished. In this case, the remaining inner disk is accreted onto the star. The strength of the magnetic field does not have a significant influence on the location of gap creation, but a strong magnetic field can stop the accretion and turn the mass flux in the inner disk outward for more massive remaining disks than a weak field is able to. This leads to a much larger dispersal timescale of the inner disk, although the differences in gap creation time are minimal between the models with different stellar magnetic field strengths. Furthermore, stronger magnetic fields lead to larger rest masses in the non-photoevaporating simulations.
When reducing the viscosity of the MRI-active regions, it can be observed that a deeper gap is created at larger radii, whereas a higher viscosity can result in the dispersal of the outer disk before a gap can be created. Furthermore, a high ratio of the viscosity parameters $\alpha_{\mathrm{MRI}}/\alpha_{\mathrm{base}}$ can lead to thermal instability-induced accretion outbursts. Photoevaporation can reduce the number of bursts by depriving the disk of resupply of mass, but the early stages of the burst phase are largely unfazed.
A smaller value of the viscosity of the MRI-inactive regions α_{base} causes a larger pile-up of mass in the dead zone, a smaller mass flux in the initial model and a smaller surface

density in the outer disk, leading to a fast creation of a gap. However, $\alpha_{\rm base}$ does not have an influence on the location of gap creation.

The results of this thesis show that the timescales of the stages of photoevaporative disk dispersal are very sensitive to the set of model parameters and the consequent structure of the initial model for the simulations. But using the described methods, it is indeed possible to create disk models which show extended gaps out to radii of several dozen AU while still retaining a significant accretion rate onto the star. Therefore, the results can point towards a solution of the long standing problem that X-ray photoevaporation is unable to produce such disks, which make up a large part of observed transition disks. In addition to that, it has also been shown that using the TAPIR-Code, well established results of the photoevaporation-induced disk dispersal can be reproduced. However, the presented model still has potential of improvement.
The initial disk masses of the simulations in this thesis are chosen to be only 1% of the stellar mass in order to avoid gravitational instabilities. Since the used photoevaporation profiles were configured for a star with a mass of 0.7 $M_\odot$, the resulting disk masses are very small. Although a description for the viscosity of gravitationally unstable regions is already in place, further research is needed to confirm its accuracy, after which larger disk masses can be chosen. This may result in different gap structures and timescales of inner and outer disk dispersal. Picogna et al. (2021) already investigated the impact of stellar mass on the photoevaporation rates based on the studies of Picogna et al. (2019) and Ercolano et al. (2021). The implementation of the corresponding mass loss profiles in the TAPIR-Code will also allow the variation of the stellar (and disk) masses in the simulations.
As already pointed out in several studies (e.g. Gorti et al. 2009; Wang & Goodman 2017; Nakatani et al. 2018), FUV radiation could play an important (or even dominant) role in the photoevaporative processes in disks. Therefore, the consideration of FUV, not only from the central star, but potentially also from the interstellar environment, would be a valuable addition to the photoevaporation model. In conjunction, a dust evolution model is desirable to investigate this process more accurately.
The combination of photoevaporation and magnetocentrifugal winds resulting from large-scale, global magnetic fields can also be an interesting next step, since the disk evolution is then not only influenced by mass loss, but also by removal of angular momentum by magnetic torques.
Finally, the investigation of massive bodies like planetesimals or planets in discs undergoing photoevaporative processes promises to yield interesting insights for the formation of planetary systems. A study of a mass sink term representing a planetary body in the equations of the TAPIR-Code is already in the works and can be combined with the current photoevaporation model.
Modelling the evolution of protoplanetary disks is a complex matter due to the many dif-

ferent physical processes taking place at the same time and interacting with each other. Using an implicit integration scheme can make such simulations even more cumbersome. But the unique opportunities offered by such a scheme paint the TAPIR-Code as a very versatile method and fruitful ground for significant progress in this field of research. The photoevaporation model presented and analyzed in this thesis represents a valuable addition to the code, further demonstrating and testing its abilities to produce scientifically accurate results.

Bibliography

Adams, F. C., Hollenbach, D., Laughlin, G., & Gorti, U. 2004, The Astrophysical Journal, 611, 360

Alexander, R. D., Clarke, C. J., & Pringle, J. E. 2006, Monthly Notices of the Royal Astronomical Society, 369, 216

Bae, J., Hartmann, L., Zhu, Z., & Gammie, C. 2013a, The Astrophysical Journal, 774, 57

Bae, J., Hartmann, L., Zhu, Z., & Gammie, C. 2013b, The Astrophysical Journal, 764

Bai, X. N. & Stone, J. M. 2011, The Astrophysical Journal, 736, 144

Balbus, S. A. & Hawley, J. F. 1997, International Astronomical Union Colloquium, 163, 90

Bell, K. R. & Lin, D. N. C. 1994, The Astrophysical Journal, 427, 987

Bendo, G. J., Joseph, R. D., Wells, M., et al. 2003, The Astronomical Journal, 125, 2361

Berger, M. J. & Oliger, J. 1984, Journal of Computational Physics, 53, 484

Bouvier, J., Grankin, K., Ellerbroek, L. E., Bouy, H., & Barrado, D. 2013, Astronomy and Astrophysics, 557, A77

Bustamante, I., Merín, B., Bouy, H., et al. 2016, Astronomy and Astrophysics, 587

Campana, S., Stella, L., Mereghetti, S., & De Martino, D. 2018, Astronomy and Astrophysics, 610, 46

Clarke, C. J., Gendrin, A., & Sotomayor, M. 2001, Monthly Notices of the Royal Astronomical Society, 328, 485

Courant, R., Friedrichs, K., & Lewy, H. 1928, Mathematische Annalen, 100, 32

Dorfi, E., Pikall, H., Stökl, A., & Gautschy, A. 2006, Computer Physics Communications, 174, 771

Dorfi, E. A. & Drury, L. O. 1987, Journal of Computational Physics, 69, 175

Ercolano, B., Barlow, M. J., Storey, P. J., & Liu, X. W. 2003, Monthly Notices of the Royal Astronomical Society, 340, 1136

Ercolano, B., Clarke, C. J., & Drake, J. J. 2009, The Astrophysical Journal, 699, 1639

Ercolano, B., Drake, J. J., Raymond, J. C., & Clarke, C. C. 2008, The Astrophysical Journal, 688, 398

Ercolano, B. & Pascucci, I. 2017, Royal Society Open Science, 4, 170114

Ercolano, B., Picogna, G., Monsch, K., Drake, J. J., & Preibisch, T. 2021, Monthly Notices of the Royal Astronomical Society, 508, 1675

Francis, L. & van der Marel, N. 2020, The Astrophysical Journal, 892, 111

Franz, R., Picogna, G., Ercolano, B., et al. 2022, Astronomy and Astrophysics, 659, A90

Fung, J. & Dong, R. 2015, Astrophysical Journal Letters, 815, L21

Gammie, C. F., Gammie, & F., C. 1996, The Astrophysical Journal, 457, 355

Gárate, M., Delage, T. N., Stadler, J., et al. 2021, Astronomy and Astrophysics, 655, A18

Gorti, U., Dullemond, C. P., & Hollenbach, D. 2009, The Astrophysical Journal, 705, 1237

Gorti, U. & Hollenbach, D. 2008, The Astrophysical Journal, 690, 1539

Gorti, U., Liseau, R., Sándor, Z., & Clarke, C. 2016, Space Science Reviews, 205, 125

Gressel, O., Nelson, R. P., & Turner, N. J. 2012, Monthly Notices of the Royal Astronomical Society, 422, 1140

Güdel, M., Briggs, K. R., Arzner, K., et al. 2007, Astronomy and Astrophysics, 468, 353

Haisch, Jr., K. E., Lada, E. A., & Lada, C. J. 2001, The Astrophysical Journal, 553, L153

Hartmann, L., Herczeg, G., & Calvet, N. 2016, Annual Review of Astronomy and Astrophysics, 54, 135

Hollenbach, D., Johnstone, D., Lizano, S., & Shu, F. 1994, The Astrophysical Journal, 428, 654

Illarionov, A. F. & Sunyaev, R. A. 1975, Astronomy and Astrophysics, 39, 185

Johns-Krull, C. M. 2007, The Astrophysical Journal, 664, 975

Kastner, J. H., Huenemoerder, D. P., Schulz, N. S., Canizares, C. R., & Weintraub, D. A. 2002, The Astrophysical Journal, 567, 434

Kastner, J. H., Richmond, M., Grosso, N., et al. 2004, Nature, 430, 429

Kimura, S. S., Kunitomo, M., & Takahashi, S. Z. 2016, Monthly Notices of the Royal Astronomical Society, 461, 2257

Kluzniak, W. & Rappaport, S. 2007, The Astrophysical Journal, 671, 1990

Kóspál, Ábrahám, P., Acosta-Pulido, J. A., et al. 2016, Astronomy and Astrophysics, 596, A52

Kratter, K. & Lodato, G. 2016, Annual Review of Astronomy and Astrophysics, 54, 271

Kunitomo, M., Ida, S., Takeuchi, T., et al. 2021, The Astrophysical Journal, 909, 109

Kunitomo, M., Suzuki, T. K., & Inutsuka, S.-i. 2020, Monthly Notices of the Royal Astronomical Society, 492, 3849

Livio, M. & Pringle, J. E. 1992, Monthly Notices of the Royal Astronomical Society, 259, 23P

Lynden-Bell, D. & Pringle, J. E. 1974, Monthly Notices of the Royal Astronomical Society, 168, 603

Morishima, R. 2012, Monthly Notices of the Royal Astronomical Society, 420, 2851

Nakatani, R., Hosokawa, T., Yoshida, N., Nomura, H., & Kuiper, R. 2018, The Astrophysical Journal, 865, 75

Owen, J. E. 2016, Publications of the Astronomical Society of Australia, 33, e005

Owen, J. E., Clarke, C. J., & Ercolano, B. 2012, Monthly Notices of the Royal Astronomical Society, 422, 1880

Owen, J. E., Ercolano, B., & Clarke, C. J. 2011, Monthly Notices of the Royal Astronomical Society, 412, 13

Owen, J. E., Ercolano, B., Clarke, C. J., & Alexander, R. D. 2010, Monthly Notices of the Royal Astronomical Society, 401, 1415

Parker, E. N., Parker, & N., E. 1958, The Astrophysical Journal, 128, 664

Pascucci, I., Cabrit, S., Edwards, S., et al. 2022, eprint arXiv:2203.10068

Picogna, G., Ercolano, B., & Espaillat, C. C. 2021, Monthly Notices of the Royal Astronomical Society, 508, 3611

Picogna, G., Ercolano, B., Owen, J. E., & Weber, M. L. 2019, Monthly Notices of the Royal Astronomical Society, 487, 691

Preibisch, T., Kim, Y., Favata, F., et al. 2005, The Astrophysical Journal Supplement Series, 160, 401

Ragossnig, F., Dorfi, E. A., Ratschiner, B., et al. 2020, Computer Physics Communications, 256, 107437

Ribas, Á., Merín, B., Bouy, H., & Maud, L. T. 2014, Astronomy and Astrophysics, 561, 54

Rodenkirch, P. J., Klahr, H., Fendt, C., & Dullemond, C. P. 2020, Astronomy and Astrophysics, 633, A21

Romanova, M. M., Toropina, O. D., Toropin, Y. M., & Lovelace, R. V. E. 2003, The Astrophysical Journal, 588, 400

Shakura, N. I. & Sunyaev, R. A. 1973, Symposium - International Astronomical Union, 55, 155

Steiner, D., Gehrig, L., Ratschiner, B., et al. 2021, Astronomy and Astrophysics, 655

Tarter, C. B., Tucker, W. H., & Salpeter, E. E. 1969, The Astrophysical Journal, 156, 943

Telleschi, A., Güdel, M., Briggs, K. R., Audard, M., & Palla, F. 2007, Astronomy and Astrophysics, 468, 425

Toomre, A. 1964, The Astrophysical Journal, 139, 1217

Van Der Marel, N., Van Dishoeck, E. F., Bruderer, S., et al. 2016, Astronomy and Astrophysics, 585, A58

Wang, L. & Goodman, J. 2017, The Astrophysical Journal, 847, 11

Waters, T. R. & Proga, D. 2012, Monthly Notices of the Royal Astronomical Society, 426, 2239

Williams, J. P. & Cieza, L. A. 2011, Annual Review of Astronomy and Astrophysics, 49, 67

Winkler, K. H. A., Norman, M. L., & Mihalas, D. 1984, Journal of Quantitative Spectroscopy and Radiative Transfer, 31, 473

Wölfer, L., Picogna, G., Ercolano, B., & van Dishoeck, E. F. 2019, Monthly Notices of the Royal Astronomical Society, 490, 5596

Zhang, S., Zhu, Z., Huang, J., et al. 2018, The Astrophysical Journal, 869, L47

Zhu, Z., Hartmann, L., & Gammie, C. 2010a, The Astrophysical Journal, 713, 1143

Zhu, Z., Hartmann, L., Gammie, C. F., et al. 2010b, The Astrophysical Journal, 713, 1134